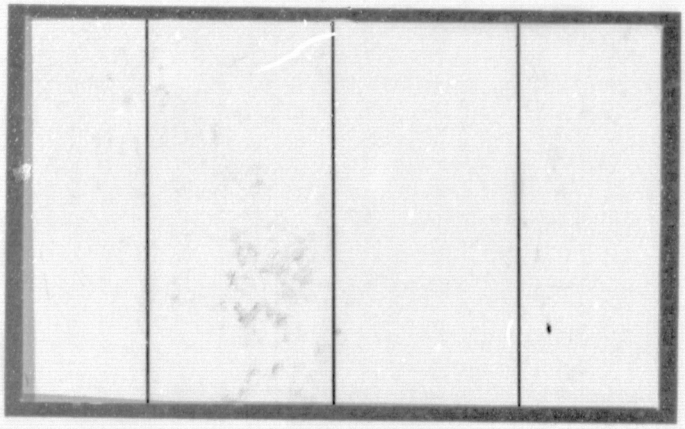

Aerospace Division

Ball Brothers Research Corporation

DEWAR TECHNOLOGY STUDY

FINAL REPORT

F75-20 October 1975

Prepared By

W. Davis
Study Manager

Approved By

Dr. R. N. Herring
Assistant Director,
Space Sciences

Aerospace Division
Ball Brothers Research Corporation
SUBSIDIARY OF BALL CORPORATION
BOULDER, COLORADO 80302

FOREWORD

This Helium Dewar Technology Study for the Stanford Relativity Experiment was performed by Ball Brothers Research Corporation (BBRC) under Contract NAS8-29848 from the NASA/Marshall Space Flight Center. The BBRC Program Manager was Dr. William B. Davis. This report covers work done on porous plugs, neck design, instrumentation and insulation of a 650 liter dewar.

Section 1

SUMMARY

1.1 POROUS PLUG STUDIES

Operation of a superfluid open cycle dewar in zero-g requires liquid/gas phase separation to prevent superfluid creep out of the dewar through the vent line. A porous plug, a device with many very small holes, is one way to provide phase separation.

An experimental apparatus was built to test the operation of a conducting material (nickel) plug and an insulating material (ceramic) plug. Operating characteristics were determined by varying the temperature of the helium in a storage chamber. Operational range is reduced with the larger (2 μ) pore size of the nickel plug compared to the range for the smaller (0.5 μ) pore size of the ceramic plug. Results indicate that material conductivity is not important, but pore size is. Results are consistent with other experimenters' results.

1.2 NECK STUDIES

A liquid helium dewar which houses an instrument requiring an external view, such as the telescope for the Stanford Relativity Experiment, must have a transition from the cold cavity to the outside. This "neck" must have mechanical stability as well as thermal properties appropriate for a long life dewar. Insulation treatment of the neck tube interface is important and the neck tube must mechanically tolerate relative motion between the inner vessel and the outer shell. This investigation involved the examination of the relationship between load carried by the neck and load carried by supports. Two methods of insulation were investigated. Results

indicate that mechanical and thermal requirements of the neck transition should not present insurmountable problems in detail design.

1.3 INSTRUMENTATION STUDIES

Temperature, pressure and mass flow instrumentation is essential for monitoring dewar performance. This task involved investigation to determine the best devices and techniques for the required instrumentation.

Results indicate that existing germanium thermometer sensors are adequate, but that suitable amplifiers are not existing. Amplifiers were designed, built and tested for absolute and for differential measurements.

The Stanford thrustors were tested for mass flow characteristics and are adequate.

A SenTran pressure sensor was selected and tested and is adequate.

The Stanford thrustors in combination with the SenTran pressure sensors to measure plenum pressure appear to be the best mass flow meter since other devices are not usable at the low flow pressures and rates contemplated.

1.4 HELIUM DEWAR INSULATION

The dewar insulation task was to install multilayer insulation blankets on a 40-inch diameter by 40-inch long pressure vessel. The vessel is supported by fixed fiberglass and retractable titanium supports. The blankets are divided into four sections separated by three vapor-cooled shields. The insulation is aluminized mylar

sheets separated by dacron net sheets. Special treatment of the ends of the vessel, penetrations through the blankets, attachments and plumbing were worked out. Special tooling for cutting the insulation was evolved. The insulation layer density was varied from the inside to the outside. The pressure vessel insulation is five layers thick, the first vapor-cooled shield insulation is 16 layers, the second shield insulation is 20 layers, and the outer shield insulation is 34 layers.

Temperature instrumentation installed consisted of four chromel/constantan thermocouples and two germanium temperature sensors.

The insulation installation was apparently successful since the dewar ambient boil-off rate is quite close to that predicted by analysis and previous model testing.

Section 2

POROUS PLUG STUDIES

2.1 INTRODUCTION

The operation of an open cycle liquid cryogenic system in zero-g requires special considerations for fluid containment and efficient heat transfer to the cryogen. For liquid helium below the lambda point, the situation is compounded by superfluid film creep. Superfluid films can transport large quantities of liquid and can conduct large amounts of heat. A method for containment of superfluid helium to prevent it from creeping into the vent system is essential.

One device for superfluid helium containment is called a porous plug. This section describes experimental studies of two such devices, one made from conducting material and one made from an insulating material.

2.2 THEORY

Superfluid helium behavior is best explained by assuming the liquid has two components, the fraction of each depending upon the temperature. One component is normal helium which has normal viscosity and entropy; the other component is superfluid which behaves as if it has zero viscosity and no entropy (for low flow velocities of interest in dewars).

In this model, then, when heat flows into the two component fluid, the superfluid flows toward the heat source and the normal fluid flows away to equalize the temperature. Now if such a heat/liquid flow regime is constrained to flow through a very small hole, the normal fluid flow rate is constrained by its viscosity, but the superfluid flow rate has no such constraint since it has no viscosity. Therefore, the superfluid is pumped through a small hole toward a heat source, a phenomenon called the fountain effect. If the

outer surface of the small hole is vented to space, that surface becomes colder and the fountain pressure keeps the normal fluid contained.

2.3 EXPERIMENTAL APPARATUS

2.3.1 Design Considerations

There were two basic goals to be achieved in designing the experimental apparatus. First, an isolated and controlled thermal environment had to be provided for the porous plug assembly. Secondly, a method for filling the liquid helium storage chamber upstream of the porous plug had to be designed. Both these goals were achieved in the design of the apparatus.

An isolated and controlled thermal environment was provided by mounting the porous plug assembly inside an evacuated can which was immersed in a liquid helium bath at 4.2°K. The assembly was suspended from a mounting flange by low thermally conductive supports. Radiative heat inputs from the 300K outside environment were minimized by proper baffling.

The filling system for the storage chamber was initially designed to allow direct filling of the chamber from a liquid helium storage dewar. This method was chosen to insure that superfluid film creep would not introduce spurious heat leaks to the inner porous plug assembly. In actual practice, the filling system was modified twice as will be detailed below.

2.3.2 Apparatus Description

Figure 2-1 shows the experimental apparatus with the evacuated can installed. The lower evacuated can was designed to fit 7-1/2 inch inside diameter of a standard laboratory liquid helium dewar. The

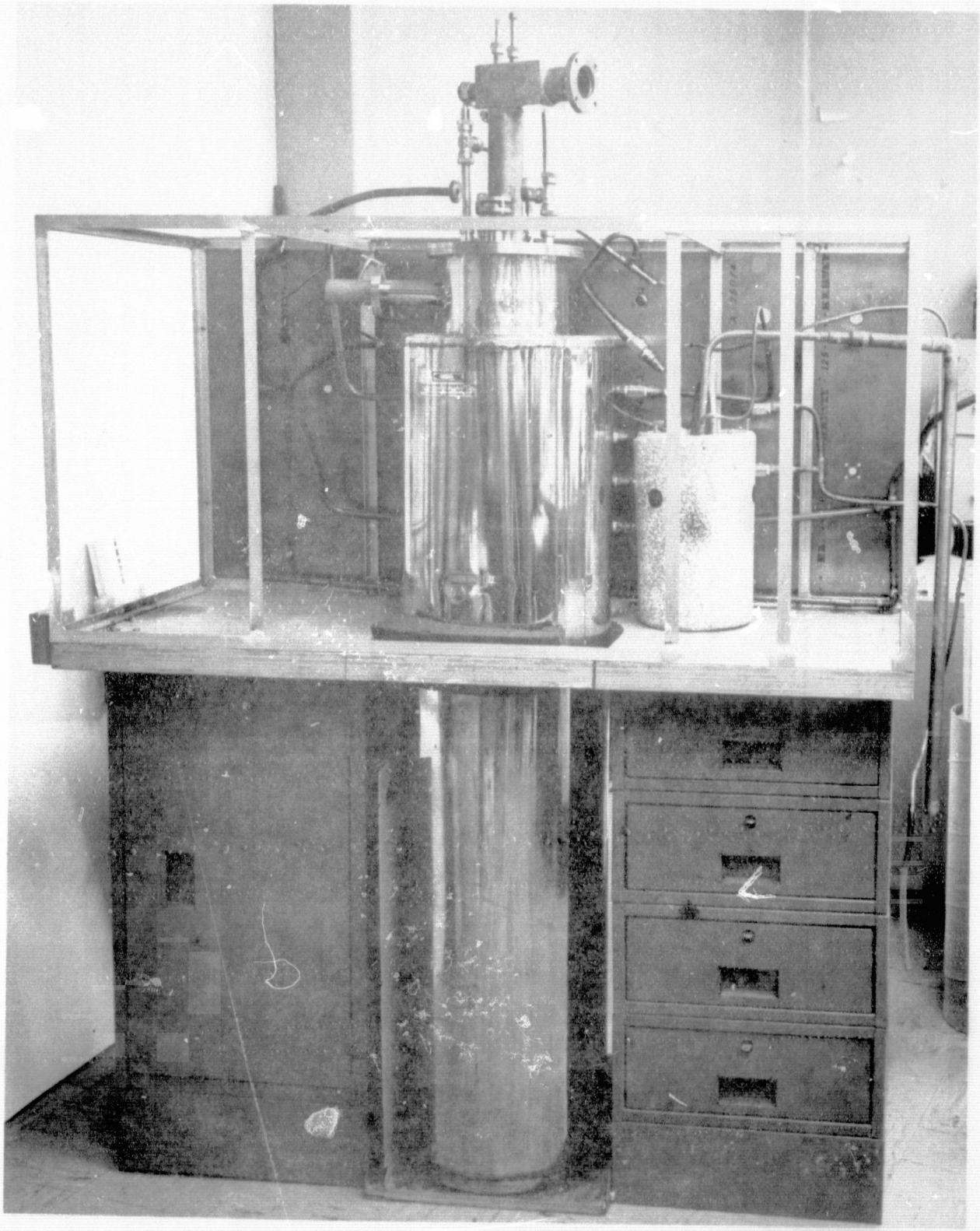

Figure 2-1 Experimental Apparatus

can was suspended from the dewar cover flange by a 2" x 0.020" wall stainless steel tubing. The tubing was made in two sections and later joined with a soft solder union. The lower piece of tubing had a radiation baffle silver brazed to the inside of the tube to prevent 300K radiation from reaching the inner assembly. The can was evacuated through the 2-inch diameter tube by means of a liquid nitrogen trapped oil diffusion pump. Pressures of 1×10^{-6} torr were achievable with the apparatus at room termperature.

Figure 2-2 is a sketch of the evacuated can and porous plug assembly. The outer can was made of rolled stainless steel 304 sheet metal 0.020 inches thich, heli-arc welded along the seam and around the top flange and the bottom cover. The top of the can was mated to a 3/4 inch thick SS304 flange, 7-1/4 inches in diameter by means of a demountable lead o-ring. The lead o-ring made from 0.020 inch diameter lead wire, provided a reliable superfluid tight joint assembly. This type of o-ring is used in all demountable joints on the apparatus and proved trouble free. Care had to be taken however, to provide close enough spacing of the attach bolts on the flanges. Even 1/2 inch SS304 flanges would distort enough to cause leaks when cooled to liquid nitrogen temperatures. Adequate spacing depends on the construction of the flange, but 3/4 inch spacing appeared to be a reasonable design criteria for most joints.

The porous plug assembly consisted of a liquid helium storage chamber, porous plug and vapor expansion chamber. The helium storage container was rolled from SS304 sheet metal, 0.020 inches thick, and welded to the top and bottom flanges. The porous plug was epoxied with Stycast epoxy into a stainless steel holder. The steel holder was soft soldered into a 3/4 inch thick SS304 flange. The epoxy was mixed with an equal part by weight of catalyst and allowed to room cure for 24 hours. This method

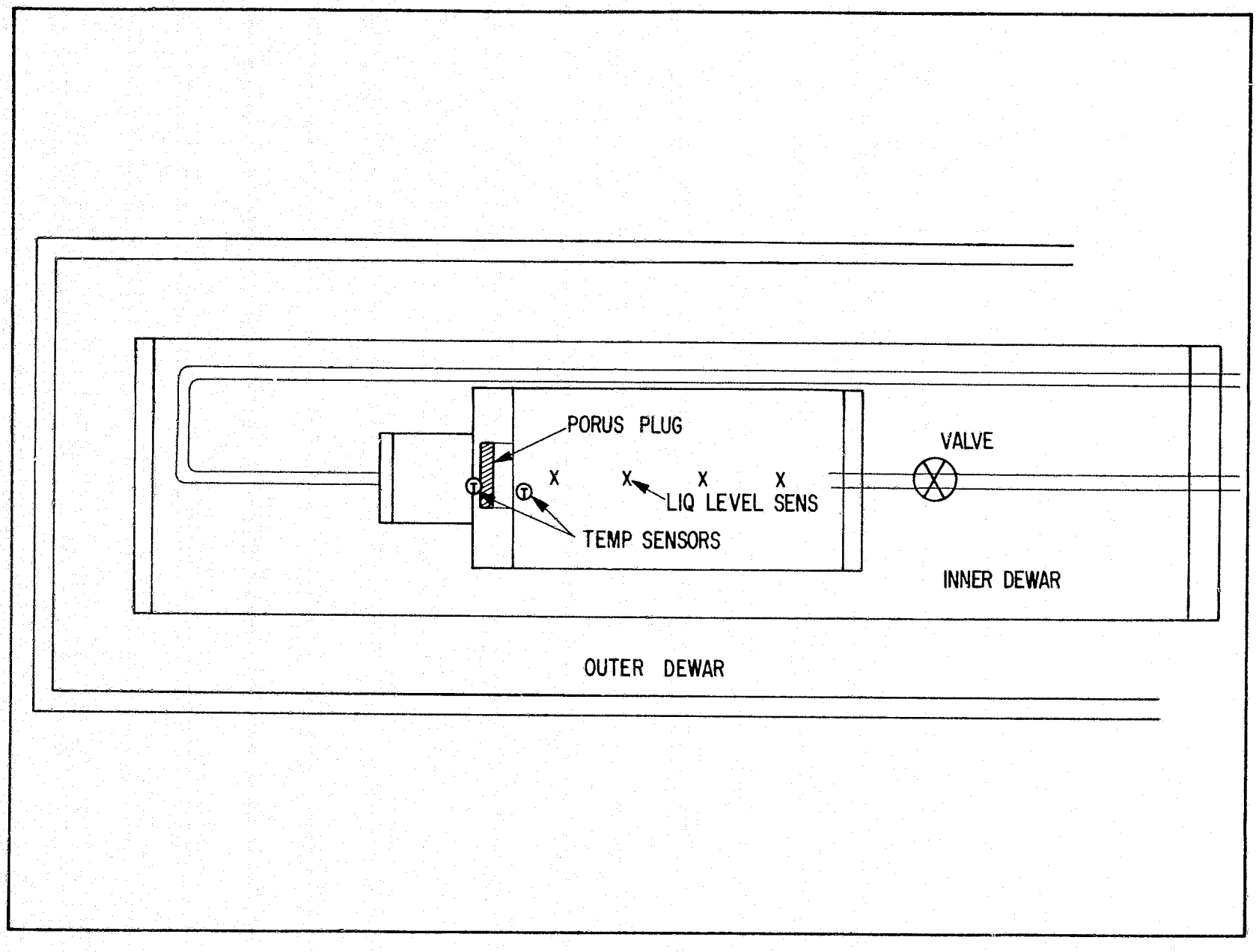

Figure 2-2 Schematic of Experimental Apparatus

F75-20

of mounting the porous plug proved reliable; however, a better method has been devised at NASA/MSFC. That method used a hydraulic press to seat the plug onto an indium o-ring seal. A cover ring was attached to prevent detachment of the plug from the indium. That method reduces the time for changing the porous plug and is probably more reliable than epoxy joints, which could crack when cooled to liquid helium temperatures.

The vapor expansion chamber was made from 2 inch OD x 0.020 inch wall SS304 tubing, welded to end flanges. The expansion chamber provided the transition from the 1/2 inch diameter pumping line to the downstream side of the porous plug. A Welch mechanical pump, liquid nitrogen trapped, pumped the downstream side of the porous plug. Pumping speed at the plug was controlled by an in-line 1/2 inch high conductance valve. Ultimate pumping speed was set by the conductance of the 1/2 inch diameter pump line.

The porous plug assembly was mounted to the top flange of the outer can. This support, which had to have a low thermal conductivity, was made from a 2 inch OD x 0.020 inch wall SS304 tubing. A piece of tubing was welded to two end flanges which mated to the top flange of the can and to the top of the helium storage container. The assembled support was then sliced into two pieces along the cylindrical axis leaving two half cylinders with approximately one inch clearance on one side and 1/4 inch clearance along the other side. The support was slit in this manner to provide access for the filling valve "B" which was mounted to the top of the helium storage container.

The liquid helium filling valve B is a 1/4 inch Hupro Bellows valve. The valve is all stainless steel with the exception of the replaceable copper stem gasket. The bellows assembly is normally mated to the valve body with a metal gasket. Since this valve must be superfluid helium tight, this gasket was replaced

with a lead o-ring gasket. The valve driver was a 1/4 inch socket fitting brazed to the end of a 1/4 inch diameter SS304 rod. The rod threaded the length of the 2 inch diameter pump and support tube and exited through a quick disconnect coupling at the top of the apparatus. The driver could be retracted from the valve once filling was completed and the valve shut.

Electrical feedthroughs were provided for temperature and level sensing devices. The feedthroughs used were of two types, standard glass Kovar feedthroughs and a lab built multi-wire feedthrough. The glass Kovar feedthroughs were single wire, commercially purchased. The lab device consisted of a short copper tube silver soldered to a 1/4 inch 304 stainless steel tube. The top of the copper piece was shaped to a knife edge. Nichrome wires were threaded through the feedthrough and epoxy applied to the top of the copper tube. The epoxy covered the knife edge of the copper tube. This type of feedthrough had been used before and worked well during this experiment.

2.3.3 Instrumentation

Instrumentation was necessary to provide information on temperature, pressure, and liquid level in the helium storage chamber. Level sensing was performed by discrete liquid sensors. The sensors were 1/8 watt 1000 Ω carbon resistors. A Cryresco liquid level sensing unit provided the input and readout signal. The unit sensed the change in resistance of the sensors when the level of the liquid helium passed through the sensor position. The change in the resistance of the sensor occurs due to the change in the thermal conductivity of the surrounding medium. Because the vapor phase has a much lower thermal conductivity than the liquid phase, the heat cannot be conducted away, and thus warms the resistor causing the resistance to change. This resistance change is sensed by the unit which indicates that a phase change from liquid to vapor has occurred at the level sensor.

To establish the operating parameters of the plug, it was important to directly measure the vapor pressure at the plug surface. This was accomplished by the use of an oil manometer connected to an 1/8 inch OD thin wall SS304 tube. This pressure monitoring tubing was placed in the 1/2 inch plug pump line such that the end of the tube was at the bend of the pump-out line on the bottom of the plug assembly, Figure 2-2. At this point, the mass velocity of the helium gas was low and thus venturi tube effects should be small.

Temperature measurements were critical to the success of the experiment. Two Cyro-Cal calibrated germanium resistance thermometers were used. One was placed 1/4 inch above the surface of the plug in the liquid helium storage container. The other one was placed on the vapor or downstream side of the plug. A gold plated copper lug was epoxied to the bottom surface of the plug. The thermometer was then mounted into the lug. Since all surfaces on the vapor side of the plug were sure to be covered with a superfluid film of helium, good thermal contact with the surface could be predicted. Eight inches of 0.005 inch diameter nichrome wire were attached to the four copper leads to the thermometer on the porous plug to prevent spurious heat loads from reaching the sensor. The nichrome wires were attached to glass kovar feedthroughs in the expansion chamber walls. A four wire potentiometric readout system was used. The thermometer resistance could be read to five place accuracy with an HP digital voltmeter. Temperature readings were then interpolated from the computer tabulated resistance versus temperature tables supplied by Cyro-Cal. The tables could be read to millidegrees kelvin.

2.3.4 Helium Storage Chamber Fill System

The filling system for the helium storage chamber evolved over several months of operating experience. Two different systems were tried before a workable system was achieved.

Initially the chamber was to be filled at 4°K from a standard laboratory helium storage cryostat. The transfer tube was inserted into a 1/4 inch tube running inside the 2 inch pump out-line. Valve "A" which was mounted on top of the storage container controlled the rate of supply to the storage chamber.

This system was found unworkable. However, it now appears that it was inoperative because of the type of porous plug which was being used at this time. The porous plug was sintered nickel with a nominal pore size of less than 2 microns. This type of plug has been shown to work, but is much more difficult to control, as will be explained below. If a ceramic porous plug had been in use at this time, this type of filling system would, in all probability, have been completely satisfactory.

The difficulty experienced with this filling system was also due to two factors in the design of the experimental apparatus. First, the pump out line was chosen to be 1/2 inch diameter to simulate the operating conditions of the BBRC liquid helium dewar. The engineering model uses 1/2 inch diameter tubing as vent lines for the porous plug. The size was chosen from calculations using expected boiloff rates of the dewar and the maximum allowable pressure drop through the vent lines. With a small mechanical pump and the 1/2 inch diameter pump line, the pumping speed at the plug would be identical for both the BBRC liquid helium dewar and the porous plug experiment. In actual operation of the experiment, however, the vapor pumping speed at the surface of the plug was not enough to maintain the necessary temperature differential across the plug. Thus, bulk liquid would flow through the plug and fill the lower chamber completely, forcing shutdown of the experiment.

Secondly, the porous plug pump line was not isolated from the cryo-stat bath. If the bath was maintained at less than 2°K while the storage container was being filled, the vapor in the pump out line

would recondense on the walls of the line and run back down the tube. This was the most serious design fault of the apparatus. The pump out line should have been completely isolated from the bath. This design ultimately limited the type of porous plug that could be studied in the apparatus to the small pore or ceramic plug.

The second type of filling system was designed to cool the helium from the storage cryostat as it was transferred to the storage chamber in the apparatus. A small holding tank was attached to the two inch pump out line. The helium from this tank flowed through a 1/16 inch diameter OFHC copper tube approximately 12 inches long formed in a helical coil. The coil was designed to cool the incoming helium below the lambda point before entering the storage chamber. This system again was not successful for the same reasons enumerated above. The sintered nickel plug required a much larger pumping capacity than was available in the apparatus in order to maintain the required temperature gradient in the plug. Thus bulk liquid would flow through the plug and fill the expansion chamber.

The third system was successful mainly because it was decided to change to the ceramic plug at the same time the fill system was modified. The third fill system used two valves, one of which was in the bath. The storage chamber was filled directly from the bath. This filling technique requires a superfluid tight valve to be successful. Once liquid is admitted to the fill line and the chamber has been filled, valve "A" and "B" are closed. The remaining liquid in the fill lines must then be pumped out by mechanical vacuum pumps. This prevents heat leaks between the storage chamber and the bath by helium films. Both valves must be superfluid helium leak tight to prevent recurrence of these films. Even with continuous pumping, a small superfluid leak in one of the valves will induce a large heat leak between the bath and the storage chamber.

This filling technique was evolved only after it had been proven that a superfluid tight valve existed. Many different designs for superfluid tight valves have been proposed and tested. However, at the start of this program, a commercially available superfluid tight valve was not available. For economic reasons, the valve described above was purchased and adapted for liquid helium work. The valve proved extremely reliable and trouble free. A second valve was then added to fill the storage chamber from the bath.

2.4 EXPERIMENTAL RESULTS

The experiment was conducted using two different porous plugs. The first plug used was made from sintered nickel 1/4 inches thick. The design specification called for an average pore size of less than 2μ. The second plug was made from a standard 6mm thick, 75mm diameter porous filter disk purchased from Coors Porcelain, Golden, Colorado. The material used was Coors P-1/2-BC. Bubble tests rated the pore size to be less than 0.5μ.

Quantitative data for the sintered nickel plug could not be obtained due to time and economic reasons. However, qualitative results will be presented to point out the similarities and differences between the behavior of the two types of plugs.

2.4.1 Ceramic Porous Plug

The ceramic porous plug was only tested with the final filling method. Once the entire apparatus had been cooled to 4°K, liquid helium was admitted to the liquid storage chamber from the 4°K bath. The vent line from the evaporation chamber was continuously pumped during filling. Both temperature sensors were monitored as were fill level sensors.

During the initial phase of filling at 4°K, the downstream side of the plug would cool to approximately 2°K. The temperature would then begin to rise slowly as the filling continued. Suddenly, the temperature would rise to the neighborhood of 3°K. At this time, filling was ceased. Mechanical pumping of the fill line was begun to lower the temperature of the liquid in the storage chamber. This action was necessary to re-establish porous plug control. Once the plug temperature of less than 2°K was reached, filling was begun anew. This cycle was repeated as often as necessary in order to fill the storage chamber to the desired level.

At the end of the fill process, the vent line was left fully open. Mechanical pumping would lower the storage chamber temperature to approximately 1.3°K. This temperature corresponds to the ultimate pumping speed of the vent line and mechanical pump. At equilibrium, the net residual heat input is balanced by the rate of evaporation at the surface of the porous plug. Figure 2-3 is a plot of rate of helium gas flow as a function of time after filling has ceased. The lowest flow rate corresponds to approximately 7.75 milliwatts residual heat load. Other data indicate that the lowest attained residual heat load was 5.8 milliwatts. In Figure 2-3 the last data point indicates that the heat leak is beginning to rise. At this time, the bath level had fallen below the top of the outer can. Thus, heat inputs to the storage chamber begin to rise as temperature gradients across the support system increased. Radiative baffling also became less effective, adding another contribution to the residual heat leak.

The operating characteristics of the porous plug can be determined by varying the temperature of the helium in the storage chamber. The temperature is varied by I^2R heating due to a wire wound resistor in the bath. Figure 2-4 shows the effect on various experiment parameters for heat inputs between 100 and 60 mwatts.

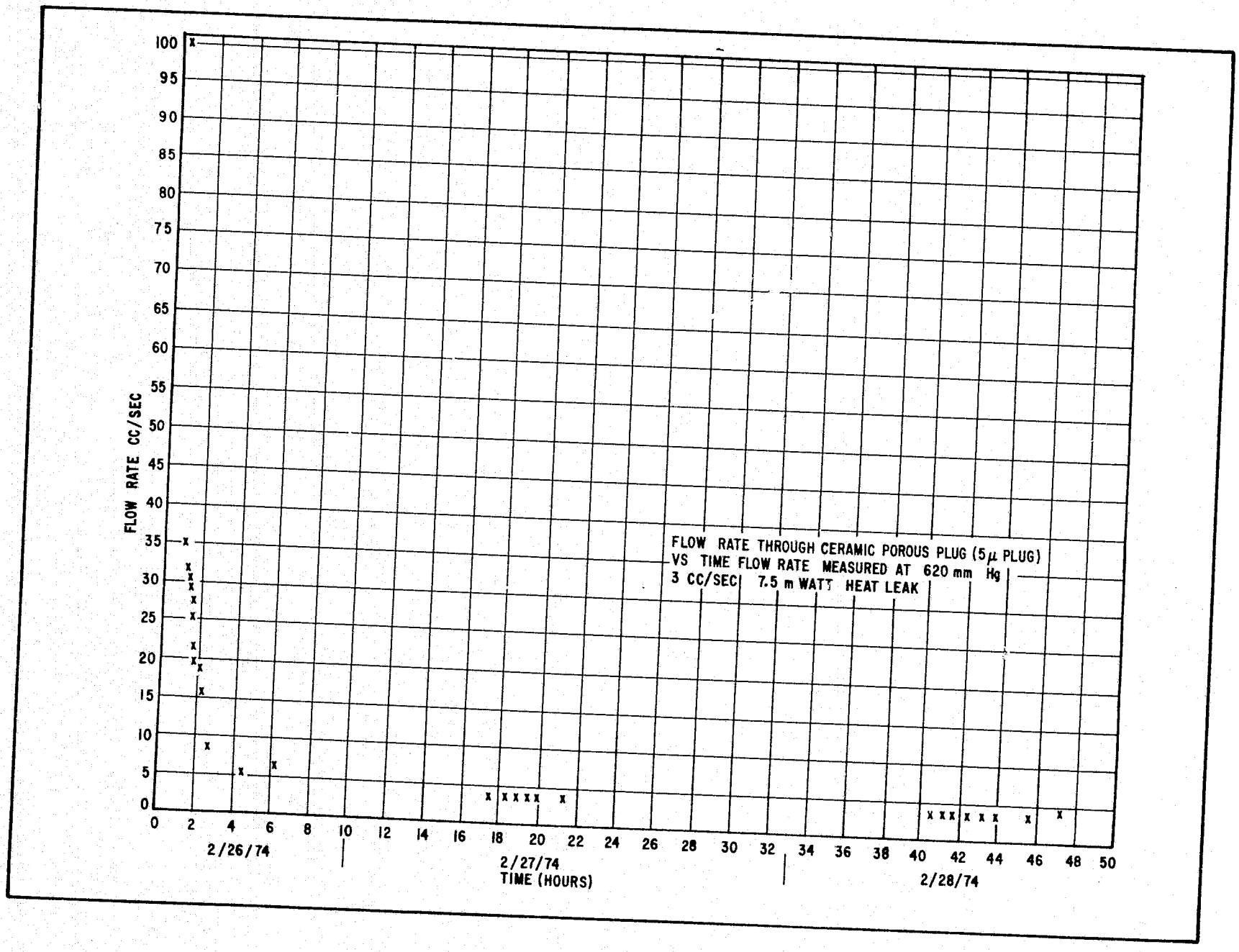

Figure 2-3 Flow Rate Versus Time

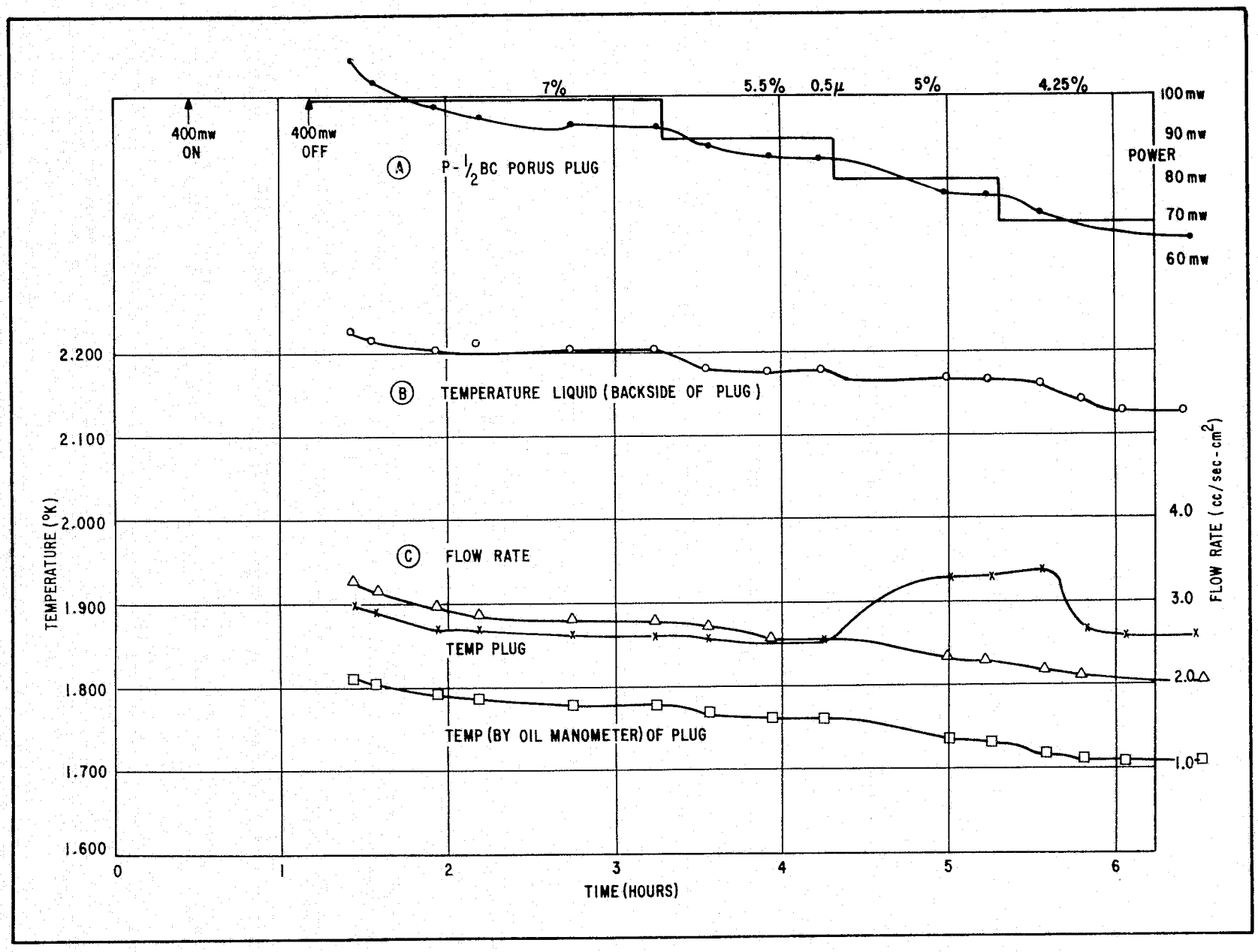

Figure 2-4 Effect of Heating Bath

In Figure 2-4(a), the top two curves compare the heat supplied to the bath through the resistor (step function) and the heat input as calculated from the helium gas flow rates. This latter quantity is calculated from the latent heat of evaporation of liquid helium. A given rate of gas flow corresponds directly to a rate of heat causing the gas to evaporate. The latent heat of evaporation varies slightly as a function of temperature. Thus, the temperature of the plug surface where the liquid is evaporated must be included in order to arrive at the heat input.

Initially, 400 mwatts of power was supplied to increase the bath temperature and gas flow rates. This power was then lowered to 100 mw at which point data was taken. The time constant for the bath to reach equilibrium conditions depends on the specific heat of the liquid. The specific heat varies with temperature. Then the time constant will be longer for a given volume of liquid at higher bath temperatures, assuming constant evaporation rates. In Figure 2-4(a) the time constants appear to be shortening as the power level is reduced from 100 to 60 mw. However, the amount of bulk liquid level is being rapidly depleted by the high heat loads; thus, no clear cut correlation was established. The time constant at a given power level depended on the initial temperature of the liquid and the rate of heat loss through evaporation at the plug surface. These parameters can be calculated if the time rate of change of the bulk liquid is known. No attempt has been made to correlate these factors as the volume of liquid present at any given time was not known.

In Figure 2-4(a) the power calculated from gas flow rates was from 7 to 4.25% lower than the calculated heater power inputs. This difference may be accountable by the resistive heat losses in the leads to the heater.

Figure 2-4(b) is the temperature of the sensor located in the bulk liquid. The temperature follows closely the change in the heater power inputs except for 70-60 mw. This power region corresponds to a phase change from He I to He II. This is accompanied by a large increase in the specific heat of the liquid as it changes phase. Thus, much more energy must be removed from the liquid for a given temperature change. This results in a much longer time constant for equilibrium to be reached.

Figure 2-4(c) gives the helium gas flow rate, the temperature of the plug and the temperature of the plug derived from oil manometer readings of the vapor pressure at the plug surface. The gas flow rate is normalized to a unit area (sq cm). The flow rate is directly proportional to the heater input at equilibrium. The curve follows the changing heat input as would be expected.

The plug temperature curve shows unexpected behavior at the 70 to 80 mw heat input. The phenomenon appears to be directly attributable to the changing temperature of the storage bath. The temperature rise occurs at the same time as the bath undergoes the phase transition to superfluid state. Why this occurs is not completely understood. In fact, it may be a completely spurious effect, since the vapor pressure at the plug shows no corresponding increase.

The temperature at the plug surface can be derived from vapor pressure thermometry. Converting vapor pressures to temperatures using standard tables gives the temperature curve shown in Figure 2-4(c). This curve does not show any increase in temperature corresponding to the anomalous temperature rise of the resistance thermometer on the plug surface. Thus the temperature rise must be questioned and subjected to further study.

The interesting feature of Figure 2-4(c) is the temperature difference as measured by resistive and vapor pressure thermometers. The difference is real and reflects the unsaturated vapor conditions in the expansion space above the plug surface. The unsaturated condition is possible since the pumping speed of the vent line is higher than the gas supply. The vapor pressure is approximately 70% of the equilibrium vapor pressure over the entire range shown.

This result is particularly interesting since it insures that superfluid film effects will not interfere with the operation of the plug in space. Unsaturated films have important characteristics. First, the thickness of the film may be much reduced. Secondly, they will still exhibit superfluidity, but the phase transition point is lowered in temperature. As a result of the above two phenomena, the film flow rates are much less than saturated film flow rates. At 1.8°K the flow rate is reduced to essentially zero by reducing the vapor pressure to 90% of the equilibrium value. Thus with a saturation percentage of 70% or less, film flow should not occur.

With the absence of film flow, the presence of unsaturated films in the vent line of the porous plug will not have any adverse effect on the operation of the plug. It has been postulated that the presence of films in the vent lines would lead to a large heat leak to the plug. This leak would occur if the films could flow to a warmer region in the vent line, evaporate and then recondense at the cold plug surface. However, this experiment has demonstrated that the films are unsaturated to such an extent that the film flow rate is essentially zero. Therefore, there should not be a heat leak due to presence of films in the vent line of the porous plug.

In Figure 2-4 the temperature differential across the plug is approximately 0.35°K. This differential is not constant over the

whole range of the experiment but depends on the bath temperature and heater input power. Measured differentials were always 0.2K or larger.

Figures 2-5 and 2-6 show the mass flow rate in grams/sec as a function of bath temperature and porous plug downstream surface temperature respectively. The flow rate is fairly linear with bath temperature over the measured range from 1.5°K to the lambda point, 2.17°K. Above the λ point the flow rate increases rapidly for small changes in bath temperature. The mass flow rate as a function of plug surface temperature does not have a simple linear dependence. In fact, the flow rate can vary considerably for a given plug temperature.

The results shown in Figure 2-5 are consistent with both Urban's and Elsner's. The ceramic porous plug operates reliably.

2.4.2 Sintered Nickel Plug

The operation of the sintered nickel plug was entirely consistent with the results of the ceramic porous plug. The only differences in the operation of the two types of plugs can be identified with the size of the pore structure. The sintered nickel plug has an average pore size of 2 microns to the less than 0.5 micron pores of the ceramic plug.

The qualitative results for the nickel plug presented here are consistent with the more detailed results achieved by Urban. The large pore size of the nickel plug reduced the operational range of the plug considerably. During filling, bulk liquid would flow through the plug very easily. It was difficult in fact to keep liquid behind the plug during filling. The filling process used in this experiment in fact is not appropriate for use with a large pore size plug.

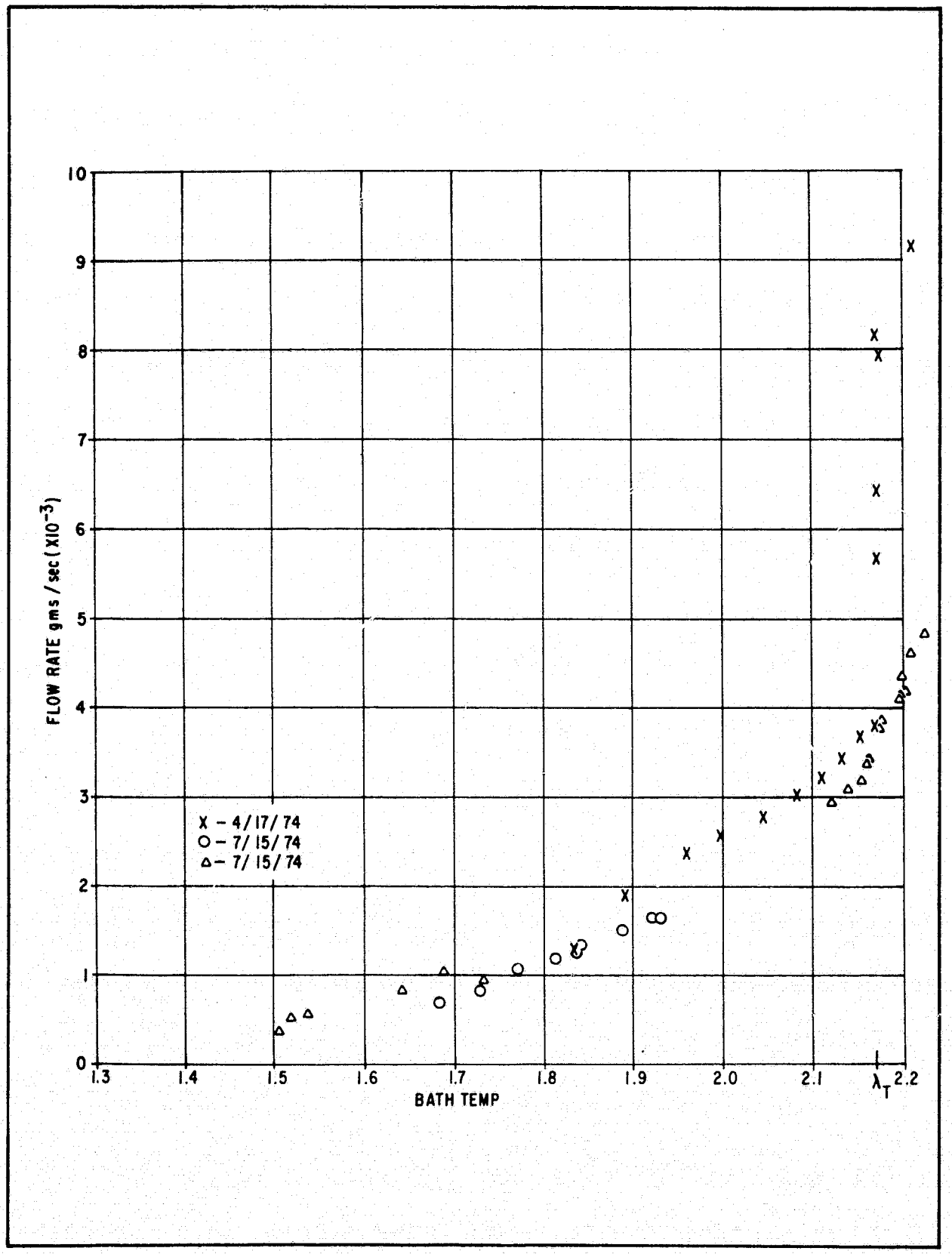

Figure 2-5 Flow Rate (Liquid) Versus Bath Temperature

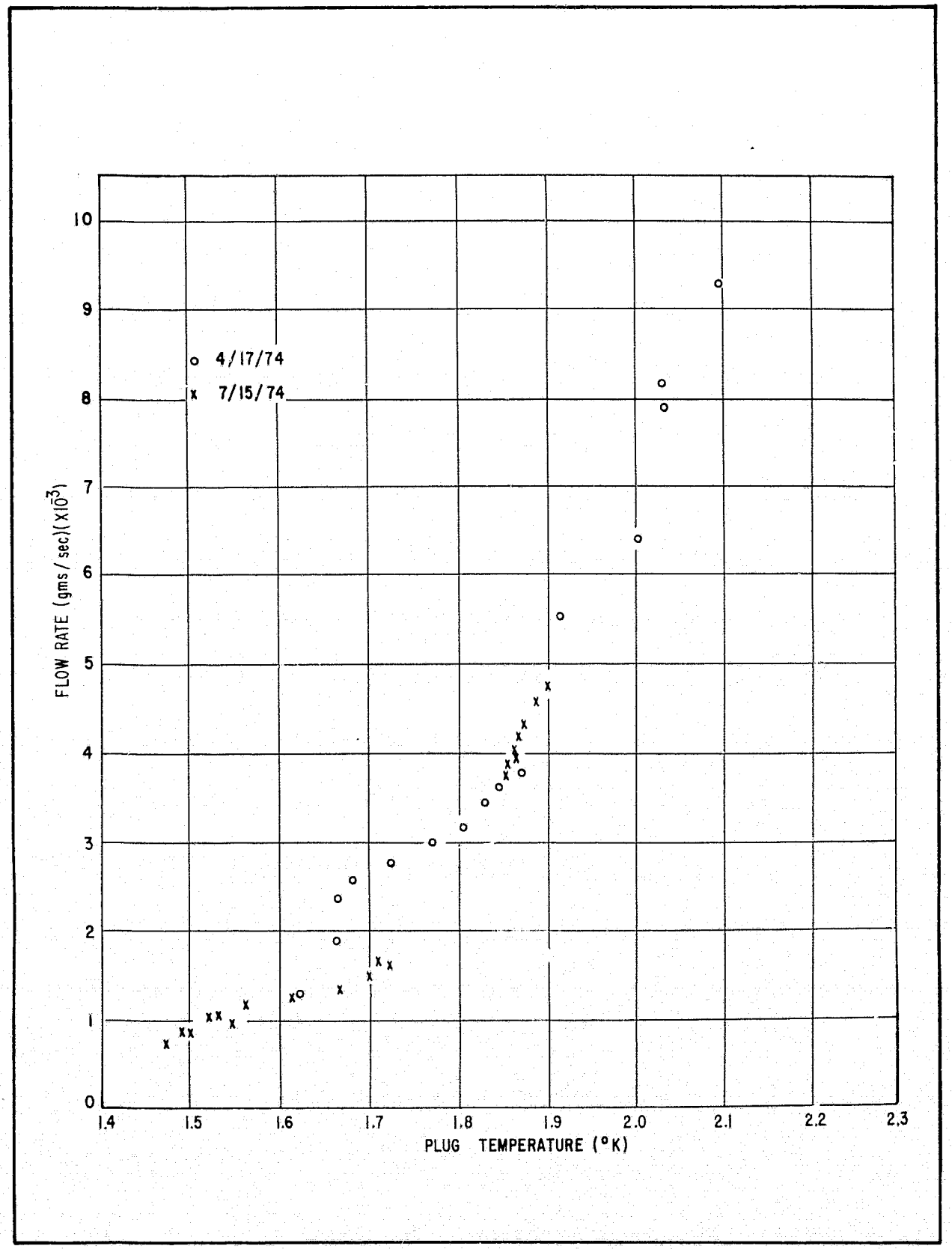

Figure 2-6 Flow Rate Versus Plug Temperature

During filling with helium at 4°K, the viscous properties of the liquid keep it from flowing freely through the plug. With a small pore plug limiting this flow, the pumps have a better opportunity to lower the temperature of the plug surface. Once the superfluid transition occurs in the plug, the fountain effect helps to contain the bulk liquid. For a large pore plug, the viscous liquid flow through the plug is much larger and leaves little operating margin in the present experiment. Use of this plug requires a smaller plug for a given size dewar.

The other operating difference between the two types of plugs also is due to the pore size. The temperature gradient across the sintered nickel plug was always less than 0.05K. It was shown above that the ceramic plug had temperature gradients larger than 0.2K. For larger pore plugs, the liquid circulation is less limited by viscous effects. Hence, the apparent thermal conductivity of the plug is increased with increasing pore size. The effect is not restricted to nickel plugs in that large pore ceramic plugs also exhibit the same temperature gradient effects.

Originally, a sintered nickel plug was chosen to insure heat exchange between the storage bath and the plug surface at which evaporation took place; however, it is now apparent that the heat transfer through the liquid is many times that through the material.

This is apparent from the dependence of thermal gradient on pore size alone. It is also apparent from Figure 2-4 in which the mass flow rates closely follow the heater input power levels. These results lead to the conclusion that the material composition of the plug has no effect on heat exchange between the bulk liquid and the plug surface.

Section 3

NECK DESIGN

3.1 INTRODUCTION

For the relativity satellite, a star tracking telescope must see out of the dewar from the cold environment since the telescope must be firmly attached to and accurately aligned with the cold gyroscopes. This makes necessary a window and neck assembly causing a structural tie (the neck tube) to exist from the outer shell of the dewar to the inner vessel cavity. This structural tie can be made very soft by using a bellows for decoupling or could be made quite stiff by using a solid fiberglass tube. One potential requirement makes the use of a stiff tube attractive. That is the potential for flying a relativity mission using external roll gyros so that relative motion between the instrument (pressure vessel) and the roll gyro (outer shell) should be minimized. The nature of a fiberglass strap support system for holding the inner dewar within the outer shell is that fairly small temperature gradients in the outer shell can cause several arc seconds of roll differential motion between the inner and outer structures. A stiff neck tube (structural member) could materially improve this situation and could, in fact, replace strap supports at one end of the dewar to reduce heat leak. This investigation looks at the structural situation using a neck tube as a structural member by comparing various geometries and stiffness combinations under vibration and static accelerations for a Scout vehicle (Appendix A shows levels used).

3.2 STRUCTURAL MODEL

The system was analyzed by using a finite element mathematical model. All parts were assumed rigid except for the following:

- Plate connecting composite cylinder to outer shell
- Composite cylinder
- Two concentric titanium cylinders
- Plate connecting two titanium cylinders
- Tension supports

Tests and analysis which have been performed by BBRC have established that suitable accuracy for this study can be achieved by treating the inner vessel and outer shell as rigid. This simplification resulted in a large reduction in the effort required for the study. Mass and stiffness properties of model elements are given in Appendix B.

The finite element model was used to determine flexibility influence coefficients for the system and to determine loads in the parts of interest. The use of these factors will be further explained in the sections that follow.

3.3 VIBRATION RESONANT FREQUENCIES

The pressure vessel, experiment and fluid were considered to be a single rigid mass. Other parts were treated as without mass. This, together with the lack of coupling with motion in the other directions, allowed the system to be treated as having two degrees

of freedom when forced in the lateral direction. Axial and torsional frequencies were calculated using single degree of freedom equations.

Flexibility influence coefficients were determined with the finite element model by applying a unit lateral force and a unit movement independently at the mass center.

A three degree of freedom model, two translations and one rotation was used for the analysis. Because of axial symmetry a third dimension was not required in the model. The available finite elements in the program were not capable of describing the torsional restraint of the tension supports. The model was therefore not used for any analysis of torsion. All analysis of torsion is included in Section 3.8.

Ten configurations were studied. These models are shown in schematic form in Figure 3-1.

The structural model was also used to determine the effect of thermal contractions.

The mass and flexibilities were used in the following equation which is developed in Appendix B.

$$\lambda^2 - (M\delta_{YY} + J\delta_{\theta\theta})\lambda + MJ(\delta_{YY}\delta_{\theta\theta} - \delta_{Y\theta}\delta_{Y\theta}) = 0$$

This equation is readily solved for the two values for λ. Frequencies are related to λ in the following equation:

$$f = \frac{1}{2\pi}\sqrt{\frac{1}{\lambda}} \quad ; \quad f_1 = \frac{1}{2\pi}\sqrt{\frac{1}{\lambda_1}} \quad ; \quad f_2 = \frac{1}{2\pi}\sqrt{\frac{1}{\lambda_2}}$$

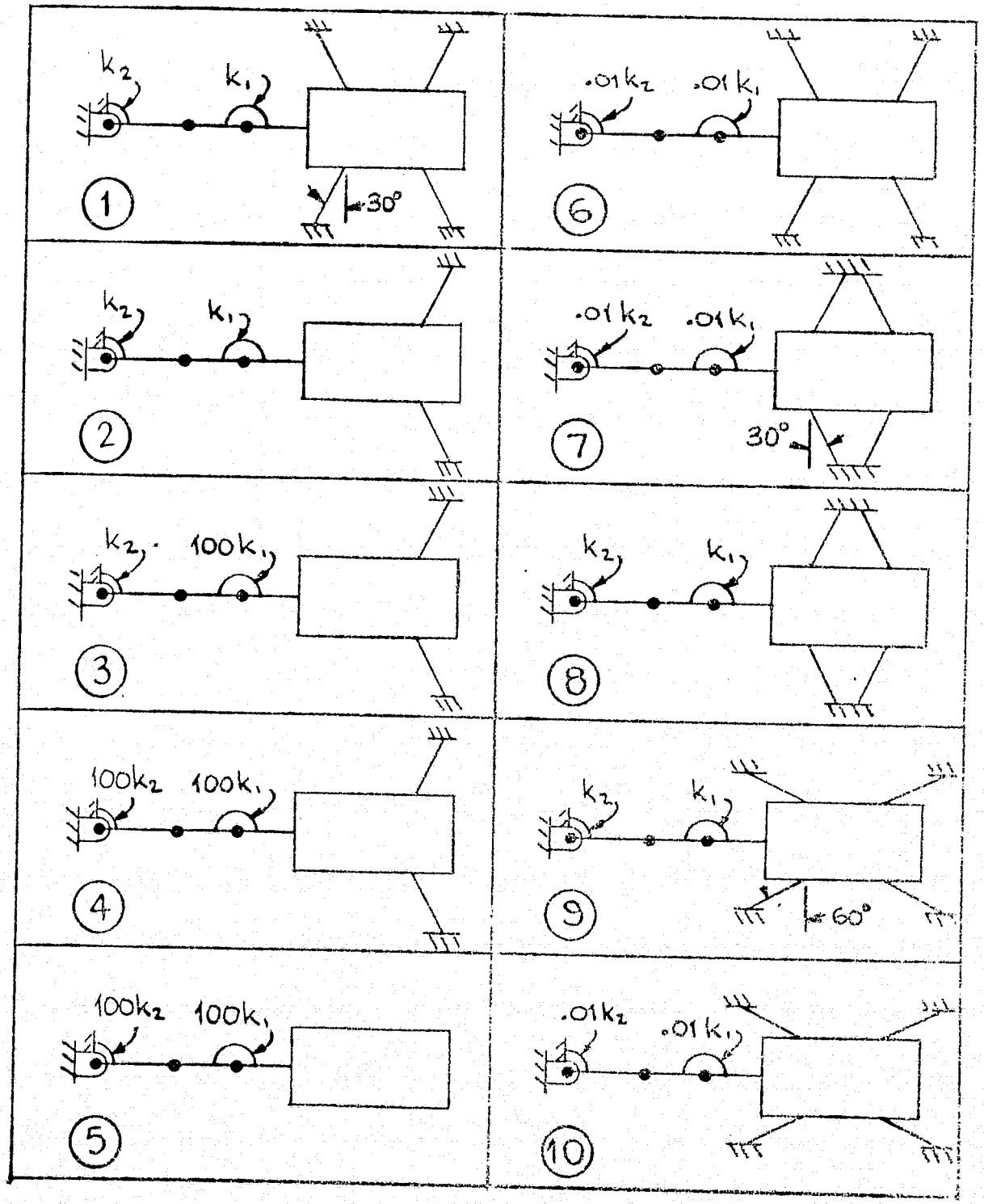

Figure 3-1 Model Configurations

The single axial influence coefficient was determined by loading the finite element model with a unit load in the axial direction. The axial frequency is determined by:

$$f = \frac{1}{2\pi}\sqrt{\frac{1}{M\delta_{XX}}}$$

Axial and lateral frequencies for the various configurations are given in Table 3-1.

Table 3-1
RESONANT FREQUENCIES

CASE	FREQUENCY (Hz)		
	AXIAL	LATERAL	
		FIRST	SECOND
1	74	46	83
2	60	45	61
3	65	51	123
4	123	53	171
5	115	20	171
6	61	17	75
7	61	74	118
8	74	76	131
9	113	45	80
10	105	43	60

3.4 LOAD FACTORS

A load factor is the vibration response of the inner vessel. It is obtained from the product of the base acceleration, as given in Section 2 and an amplification factor or transmissibility.

Transmissibility is normally obtained by test as means for its analytic determination have not been developed. The best source of test data is that of the BBRC cryopak. Though not of identical configuration, the cryopak performance should be near that of the study tank.

The measured transmissibility of the cryopak was a maximum of 22 with a base input of 0.5 g. Typically, the amplification factor is reduced as the input acceleration is increased. Also, the cryopak contained a solid instead of a liquid. For these two reasons, the transmissibility was estimated to be reduced to a value of 15 for this study. The one exception to this was the factor for case five where a value of 20 was used because of the low input acceleration.

In each case the input acceleration at the frequency of resonance was multiplied by the transmissibility to obtain a load factor. In all but one case the first mode frequency was used. The exception was the lateral factor for case six for which the second mode was used. This was done because the response of the second mode is greater than that of the first mode since the first mode involves much pitching.

The calculated load factors are included in Table 3-2.

Random vibration accelerations are much less than those for a sinusoidal input. The following calculation is an approximate response to random vibration. Use:

$D = 0.0031\ g^2/Hz$	(Section 2)
$f = 100$ Hz	(Typical value)
$Q = 20$	(For low input)

From Reference 1 for a 2.2 sigma response:

$$G = 2.2\sqrt{\frac{\pi DfQ}{2}} = 2.2\sqrt{\frac{\pi \times 0.0031 \times 100 \times 20}{2}} \quad G \simeq 79$$

This is well under the equivalent sine response factors of Table 3-2.

3.5 SUPPORT LOADING

There are three types of loads in the inner vessel supports:

- Dynamic load
- Preload
- Thermal contraction load

A discussion of each of these follows.

Dynamic Load. These loads result from an acceleration of the vessel. The acceleration may be either steady, as from thrust, or oscillatory, as from vibration. In all cases of this study, vibration loads are greater than those of a steady acceleration (compare Table 3-2 to Appendix A).

Preload. The tension supports are capable of carrying only tension loads. A support system containing these members is made most efficient when the supports are pretensioned to a value equal to their vibratory load.

Preloading serves to increase the stiffness of the system but does not cause an increase in load in the supports over that which would occur if there was no preload.

Preloading of the tension supports will not produce initial loads in the fiberglass cylinder if a symmetric system of tension supports is used. This is based on the assumption that the final cylinder attachment can be made after tension support preloading. If a non-symmetric system is employed, such as cases 2, 3 and 4, then cylinder preloading is unavoidable. This could produce undesirable effects in that a redundant system exists and uneven preloading of the tension supports would produce bending in the cylinder.

Thermal Contraction Load. Cooling of the vessel will result in shrinkage of the inner tank and the supports. The contraction will, except for certain geometries, cause the load in the tension supports to change.

Loading Data. Support loading is affected by the angle of the members. Figure 3-2 illustrates this effect when the influence of the cylinder is ignored. Complete symmetry of mass and stiffness is assumed. The figure should be self-explanatory.

Table 3-2 summarizes vibration loads in the fiberglass cylinder and the tension supports as obtained from the finite element model. The table does not include the preload though adequate preload is assumed in the calculations.

Table 3-3 adds preload to the vibration loads of Table 3-2 to show the total load in the supports. Bending is not included since it is unaffected by preload.

Support Stress. Stresses in the fiberglass cylinder are a combination of preload stress and bending stress for lateral loading. They are a combination of preload stress and dynamic load stress for axial loads.

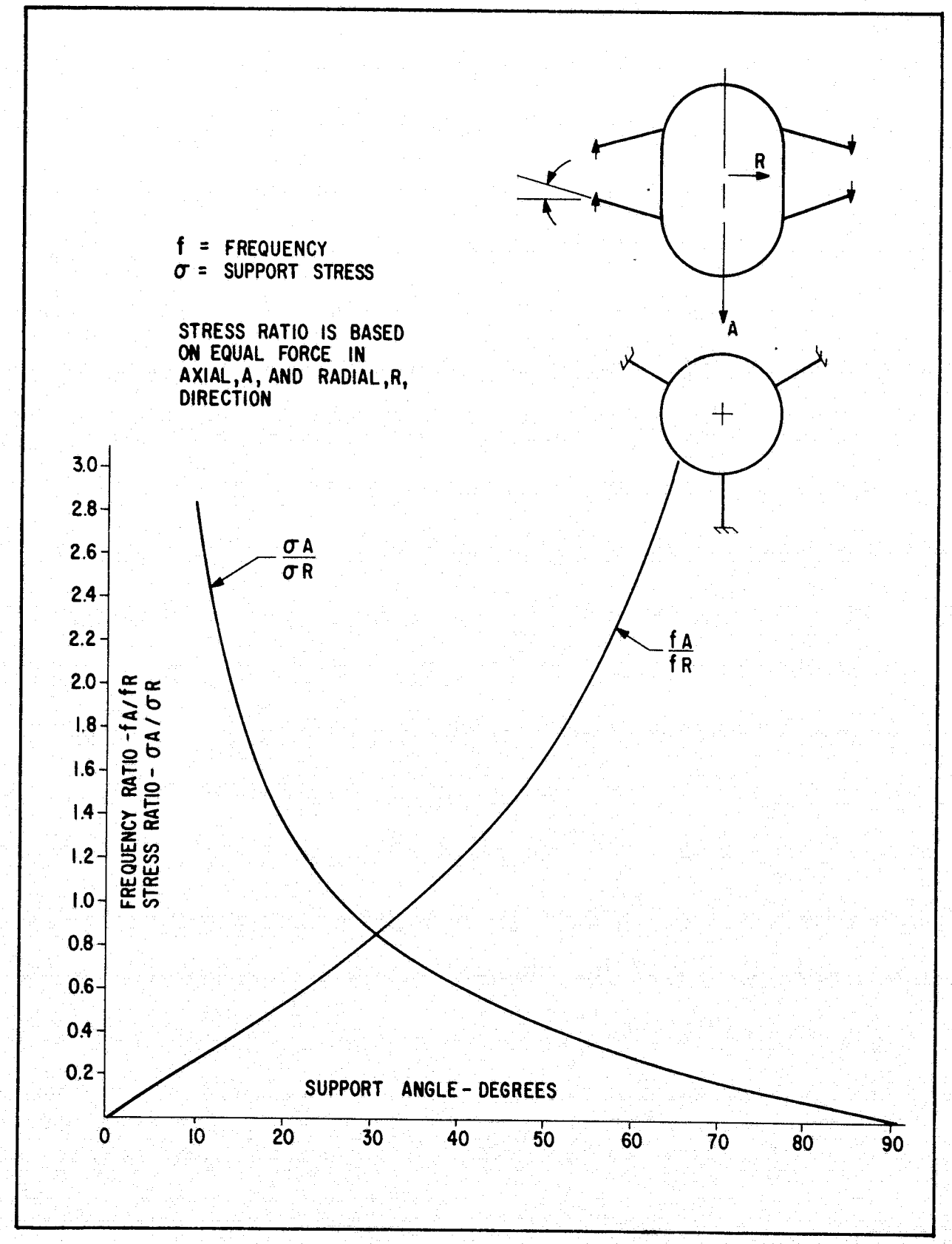

Figure 3-2 Support Loading

Table 3-2
SUPPORT VIBRATION LOADS

CASE	LOAD FACTOR (g)		MAXIMUM VIBRATION LOAD		
			FIBERGLASS CYLINDER		TENSION SUPPORT AXIAL
	AXIAL	LATERAL	AXIAL	BENDING	
1	67	22	9919	85	7046
			(2230)	(752)	(1584)
2	90	22	20185	151	14340
			(4538)	(1335)	(3224)
3	90	22	23303	133	12250
			(5239)	(1179)	(2754)
4	67	22	27195	764	6232
			(6114)	(6761)	(1401)
5	67	15	30949	3453	--
			(6958)	(30560)	--
6	90	22	222	6	13851
			(50)	(49)	(3114)
7	90	22	222	1	13851
			(50)	(11)	(3114)
8	67	22	9923	105	7046
			(2231)	(933)	(1584)
9	67	22	4181	249	7099
			(940)	(2207)	(1596)
10	67	22	58	4	7157
			(13)	(33)	(1609)

Units: Axial Load - N (lb)
Bending Load - N-M (lb-in)

Table 3-3
TOTAL AXIAL LOAD IN SUPPORTS

CASE	DYNAMIC LOAD		PRELOAD		MAXIMUM LOAD			
					POSITIVE		NEGATIVE	
	C	T	C	T	C	T	C	T
1	9919	7046	0	7046	9919	14091	-9919	0
	(2230)	(1584)	(0)	(1584)	(2230)	(3168)	(-2230)	(0)
2	20185	14340	21511	14340	41696	28681	+1326	0
	(4538)	(3224)	(4836)	(3224)	(9374)	(6448)	(+298)	(0)
3	23303	12250	18375	12250	41678	24500	-4928	0
	(5239)	(2754)	(4131)	(2754)	(9370)	(5508)	(-1108)	(0)
4	27195	6232	9350	6232	36545	12463	-17845	0
	(6114)	(1401)	(2102)	(1401)	(8216)	(2802)	(-4012)	(0)
5	30994	--	0	--	30994	--	-30994	0
	(6968)	--	(0)	--	(6968)	--	(-6968)	(0)
6	222	13851	0	13851	222	27702	-222	0
	(50)	(3114)	(0)	(3114)	(50)	(6228)	(-50)	(0)
7	222	13851	0	13851	222	27702	-222	0
	(50)	(3114)	(0)	(3114)	(50)	(6228)	(-50)	(0)
8	9923	7046	0	7046	9923	14091	-9923	0
	(2231)	(1584)	(0)	(1584)	(2231)	(3168)	(-2231)	(0)
9	4181	7099	0	7099	4181	14198	-4181	0
	(940)	(1596)	(0)	(1596)	(940)	(3192)	(-940)	(0)
10	58	7157	0	7157	58	14314	-58	0
	(13)	(1609)	(0)	(1609)	(13)	(3218)	(-13)	(0)

C = Fiberglass Cylinder
T = Tension Support
Units: N (lb)

Tension support stresses are the sum of preload stress and dynamic load stress.

Stresses are calculated assuming axial and lateral loads to be independent of each other. The stresses are given in Table 3-4.

Table 3-4
SUPPORT STRESS

CASE	CYLINDER ($N/m^2 \times 10^{-3}$); (lb/in^2)				TENSION SUPPORT ($N/m^2 \times 10^{-6}$) (ksi)
	AXIAL LOAD		LATERAL LOAD		
	TENSION	COMPRESSION	TENSION	COMPRESSION	
1	21744	-21744	3916	-3916	496
	(3154)	(-3154)	(568)	(-568)	(72)
2	91421	+2909	54104	+40206	1013
	(13261)	(+422)	(7848)	(+5832)	(147)
3	91387	-10803	46417	+34146	862
	(13256)	(-1567)	(6733)	(+4953)	(125)
4	80129	-39130	55669	-14684	441
	(11623)	(-5676)	(8075)	(-2130)	(64)
5	67968	-67968	159003	-159003	---
	(9859)	(-9859)	(23064)	(-23064)	---
6	489	-489	255	-255	979
	(71)	(-71)	(37)	(-37)	142
7	489	-481	55	-55	979
	(71)	(-71)	(8)	(-8)	142
8	21757	-21757	4853	-4853	496
	(3156)	(-3156)	(704)	(-704)	72
9	9169	-9169	11485	-11485	503
	(1330)	(-1330)	(1666)	(-1666)	73
10	124	-124	172	-172	503
	(18)	(-18)	(25)	(-25)	73

Thermal Loads. Thermal loads are considered independently of dynamic loads since support preloads can normally be set to compensate for thermal contractions. A problem can exist if the contraction load is greater than the desired preload or if a large negative contraction load exists. The former problem requires that either the final preload be greater than desired or that the supports be initially slack. The latter requires that the support load be higher than desired during a major portion of the vessel life.

Thermal loads, as calculated with the finite element model, are given in Table 3-5. These are based on a temperature change of -289°K (-520°R).

Table 3-5
THERMAL LOAD IN SUPPORTS

CASE	FORWARD SUPPORT	AFT SUPPORT	FIBERGLASS CYLINDER
1	4168	5925	2624
	(937)	(1332)	590
2	0	3781	5649
	(0)	(850)	(1270)
3	0	4368	6525
	(0)	(982)	(1467)
4	0	6859	10253
	(0)	(1542)	(2305)
5	0	0	0
	(0)	(0)	(0)
6	5031	5062	44
	(1131)	(1138)	(10)
7	1428	1401	44
	(321)	(315)	(10)
8	2291	538	2624
	(515)	(121)	(590)
9	3412	4697	3340
	(767)	(1056)	(751)
10	4043	4061	44
	(909)	(913)	(10)

Units: N (lb)

3.6 ALLOWABLE STRESSES

Tension Supports. The number of cycles between half-power points is given by:

$$\Delta f = \frac{f_n}{Q}$$

For

$f_n = 100$ and $Q = 15$:

$$\Delta f = \frac{100}{15}$$

$$\Delta f = 6.7 \text{ cycles}$$

The number of octaves is given by:

$$N = \frac{\log_{10} f_2/f_1}{\log_{10} 2}$$

With:

$$f_1 = f_n - \Delta f/2 \simeq 100 - 4 = 96$$

$$f_2 = f_n + \Delta f/2 \simeq 100 + 4 = 104$$

$$N = \frac{\log 104/96}{\log 2}$$

$$N = 0.115 \text{ octave}$$

With a sweep rate of 2 octaves per minute (see Section 2) the number of cycles of vibration is:

$$f = \frac{\text{octaves}}{\text{octaves/minute}} \times \frac{\text{seconds}}{\text{minute}} \times \frac{\text{cycles}}{\text{second}} = \frac{.115}{2} \times 60 \times 100$$

$$f = 345 \text{ cycles}$$

With a three axis test the total number of cycles is about 1000.

Data from structural Composite Industries, Azusa, California, shows the tension support material to be about 50 percent of its original strength when cycled 1000 times. Using an ultimate tensile strength of 1.4×10^9 N/m^2 (200 ksi) (obtained by BBRC) the allowable stress is:

$$F_t = 1.4 \times 10^9 \times .5$$

$$F_t = 0.7 \times 10^9 \text{ N/m}^2 \text{ (100 ksi)}$$

Fiberglass Cylinder. Additional study is required before this part can be properly analyzed. The critical loads calculated herein are based on equations for isotropic material.

It is assumed that a 0, $\pm$45, 90 layup is used for the cylinder. Using the following values for unidirectional fiberglass material:

$$E_x = 4 \times 10^{10} \text{ N/m}^2 \qquad (6 \times 10^6 \text{ psi})$$

$$E_y = 0.6 \times 10^{10} \text{ N/m}^2 \qquad (1 \times 10^6 \text{ psi})$$

$$G_{xy} = 0.4 \times 10^{10} \text{ N/m}^2 \qquad (6 \times 10^5 \text{ psi})$$

$$V_{xy} = .25$$

Along with the constitutive and transformation equations of Reference 3 the following values are calculated:

$E_1 = 2 \times 10^{10}$ N/m^2 (2.8×10^6 psi)

$E_2 = 2 \times 10^{10}$ N/m^2 (2.8×10^6 psi)

$\nu = .26$

The following critical loads are based on equations of Reference 2 for isotropic material.

The following cylinder dimensions are used:

$R = 9.5$ cm (3.75 in) (Cylinder Radius)

$L = 30.5$ cm (12.0 in) (Cylinder Length)

$t = 0.076$ cm (0.03 in) (Cylinder Thickness)

Bending

$$F_{cr} = 0.68\ E\ \frac{t}{R}$$

$$\frac{R}{t} = \frac{9.5}{.076} = 125$$

For this $\frac{R}{t}$, $\gamma = 0.62$

$$F_{cr} = 0.6 \times 0.62 \times 2 \times 10^{10} \times \frac{.076}{9.5}$$

$$F_{cr} = 6 \times 10^7 \text{ N/m}^2 \quad (8333 \text{ psi})$$

Axial compression

$$F_{cr} = 0.6\ \gamma\ E\ \frac{t}{R}$$

For

$$\frac{R}{t} = 125, \quad \gamma = 0.54$$

$$F_{cr} = 0.6 \times 0.54 \times 2 \times 10^{10} \times \frac{.076}{9.5}$$

$$F_{cr} = 5 \times 10^{7} \text{ N/m}^2 \qquad (7258 \text{ psi})$$

Allowable tensile stresses for the cylinder have not been calculated at this time. It is probable that they are much greater than the compressive allowables.

3.7 EVALUATION OF CASES

Case 1. Table 3-1 shows all frequencies to be acceptable. They are high enough to avoid large deflections. The axial frequency is well above the 6g input range from 44 to 65 Hz. Table 3-4 shows the cylinder stress to be acceptable with the critical stress being 2.6 times the maximum tabulated value. Tension support stresses are also acceptable but with a lesser safety factor than desired. The allowable stress of 7×10^8 N/m^2 (100 ksi) is 1.4 times the calculated stress. It would be desirable to have a factor of at least 1.5 but such a difference is of no concern at this stage of the study. The thermal contraction load of 5925 newtons (1332 pounds), as shown in Table 3-5, is far enough under the desired preload of 7046 newtons (1584 pounds) in Table 3-3 to be acceptable.

Case 2. The axial frequency for this case dropped to 60 Hz which is in the 6g sine input range. This caused cylinder and tension support stresses to increase to a point where they are unacceptable.

Case 3. Tension support stresses dropped from Case 2 but are still unacceptable.

Case 4. Compressive stresses in the cylinder increased to the point where the critical load is greater than the calculated stress by a factor of 1.5. Considering the possible discrepancies between calculated and actual buckling loads, the 1.5 factor is marginal. A comparison of Tables 3-3 and 3-5 shows the thermal contraction load to be greater than the minimum preload. Since the tension support stress is low it appears possible to preload to a value greater than the minimum. The increased preload would in turn reduce the cylinder compressive stress. This configuration may warrant further study.

Case 5. The removal of all tension supports results in this system being unacceptable as shown by the stresses of Table 3-4.

Case 6. Softening of the plates caused cylinder stresses to be insignificant. Tension support stresses are far too great. In addition the pitching frequency is quite low.

Case 7. This case was run to illustrate the effect of support angle reversal on frequency. The pitching frequency increased from 17 Hz of Case 6 to 118 Hz. Stresses are similar to Case 6.

Case 8. This case is essentially the same as Case 1. Lateral frequencies increased from Case 1 but support stresses are essentially unchanged.

Case 9. This case was run in an attempt to reduce both tension support and cylinder stresses. Table 3-2 shows the axial acceleration to be three times those in the lateral direction. Figure 3-2 indicates that a support angle near 60 degrees best supports this load ratio. Therefore, Case 9 was run with a 60 degree support angle. Table 3-4 shows that the cylinder stresses due to axial loading decreased while tension support stresses increased slightly. This indicates a possible reduction in cylinder thickness.

Case 10. Softening of the plates rendered the cylinder stresses insignificant with a minor increase in tension support stress. The effect on tension support stress is much less severe than the change from Case 1 to Case 6.

Torsion. With a Scout Launch it is necessary that the experiment be spun to a high angular velocity over a short period of time. For this study an angular velocity of 180 rpm achieved in 0.5 seconds was selected. This results in an angular acceleration of:

$$\ddot{\omega} = \frac{\dot{\omega}}{t} = 2\pi \times \frac{180}{60} \times \frac{1}{0.5}$$

$$\ddot{\omega} = 37.7 \ \frac{\text{rad}}{\text{sec}^2}$$

It is probable that the fluid will offer no resistance to the acceleration. The mass moment of inertia is taken as that of the dry tank:

$$J = 1.04 \text{ kg-m}^2 \qquad (9.2 \text{ lb-in}^2)$$

The resulting torque is:

$$T = J\ddot{\omega} = 1.04 \times 37.7$$

$$T = 39.2 \text{ N-m} \qquad (347 \text{ lb-in})$$

The torsional stress in the cylinder is:

$$\tau = \frac{T}{2\pi R^2 t} = \frac{39.2}{2\pi \times 9.5^2 \times .076 \times .01^3}$$

$$\tau = 9.1 \times 10^5 \text{ N/m}^2 \qquad (131 \text{ psi})$$

If the fluid is treated as a solid:

$J = 1.684$ kg-m^2 (1.684 lb-in^2)

$T = 63.5$ N-m (562 lb-in)

$\tau = 14.7 \times 10^5$ N/m^2 (212 psi)

The critical stress as determined from Reference 3 is:

$$\tau_{cr} = \frac{.747 \times .67\ E}{\left(\frac{R}{t}\right)^{5/4}\left(\frac{L}{R}\right)^{1/2}} = \frac{.747 \times .67 \times 2 \times 10^{10}}{\left(\frac{9.5}{.076}\right)^{5/4}\left(\frac{30.5}{9.5}\right)^{1/2}}$$

$\tau_{cr} = 13.4 \times 10^6$ N/m^2 (1880 psi)

The torsional stiffness of the system is due primarily to the cylinder. The torsional frequency, using the dry tank inertia and ignoring tension support stiffness, is 61 Hz.

3.9 RECOMMENDATIONS FOR FUTURE STUDY

Based on this brief study, it appears that the most critical component in the system is the fiberglass cylinder. This conclusion is based partially on the fact that the cylinder is the most difficult part to analyze. Many investigators have attempted to predict the critical load of a thin-walled cylinder. Test reports indicate that no analysis is yet capable of predicting an accurate collapse load.

It is recommended that the following effort be expended on future studies:

A. Cylinder Analysis

1. Search recent literature for information on cylinder buckling analysis. This must involve correlations between test and analysis.

2. Obtain or prepare the computer program that appears to be the most promising.

B. Dewar Analysis - Continue along the lines of the present study with a more exact analysis directed toward minimizing cylinder loads.

C. Cylinder Design - Combine the results of "A" and "B" above to design a cylinder which appears to satisfy the requirements.

D. Cylinder Test - Fabricate and test a cylinder under the conditions that analysis predicts it will experience.

If the torsion requirement diminishes it is probable that the fiberglass cylinder will become less critical. This study indicates that cylinder stresses can be held well under the critical load in bending and compression by softening the two annular plates.

Section 4

INSTRUMENTATION

Instrumentation of the liquid helium dewar is necessary for any space mission. The instrumentation includes temperature, pressure and gas mass flow sensors. The instrumentation must be compatible with both the satellite launch environment and the satellite power and telemetry subsystems. As part of the dewar technology studies, existing commercially available sensors were surveyed and evaluated for suitability and feasibility for space flight. In addition, certain critical electronic components for temperature sensor amplifiers were breadboarded and evaluated. Laboratory testing of other sensors was done to investigate stability and repeatability.

4.1 TEMPERATURE SENSORS

Standard commercial germanium thermometers were chosen for temperature sensors. These sensors have been used as secondary temperature standards by the National Bureau of Standards. Their reproducibility and stability are excellent. They can be obtained from several vendors and can be calibrated to approximately $\pm$ 1m° K. Their very small size and negligible weight are important benefits.

While the sensors themselves are commercially available, suitable flight amplifier electronics do not exist. These amplifiers were designed, breadboarded and tested as part of the study.

Two different amplifiers were designed and breadboarded; one for an absolute monitor and one for a differential monitor. The absolute temperature monitor is used to make temperature measurements in the range 1.5° to 4.2°K with an accuracy of $\pm$ 0.1°K. This type of amplifier will be used with all the germanium sensors except for monitoring the porous plug differential temperature. Each porous

plug will have two temperature sensors, one on each side. A differential temperature measurement between the two sensors is the only method that will achieve a ±1m°K accuracy, the accuracy desired when the study was initiated. Subsequent testing of the porous plug revealed differential temperatures in the 100m°K region instead. Thus, two different types of differential temperature amplifiers were designed. Only the narrow range differential amplifier was breadboarded, since the wide range amplifier was well within the state-of-the-art for space systems.

4.1.1 Absolute Temperature Monitor

The absolute temperature monitor is implemented with the bridge-type circuit shown in Figure 4-1. This configuration differs from conventional bridge-type networks in that resistor R2 is connected in series with the amplifiers inverting node. This resistor has the unique property of producing a linear output transfer function even though the germanium probe is non-linear. Selection of R2 is made such that optimum linearity is achieved in the output transfer function. There is no straight-forward analytical expression that will guide in the selection. Thus, a computer program was written which varies R2 and selects the optimum value. The resulting output is linear to about ± 0.3 m°K. (See appendix A).

The computer program also calculates the necessary values of R3, R4 and Rc for a 0 to 5 volt output over the desired temperature range. A listing of the program and a typical printout is shown in appendix A. In the printout, "DELTA VO" represents the change in output voltage from the previous temperature, "R_T" is the sensor resistance, and "amplifier gain" is the closed loop amplifier gain referenced to the voltage of the unloaded bridge. Each time a new amplifier is used, the circuit has to be re-balanced for amplifier offset voltage. Each time a different sensor is used, the optimization program must be run again with the appropriate sensor resistance-temperature data cards to determine new circuit values.

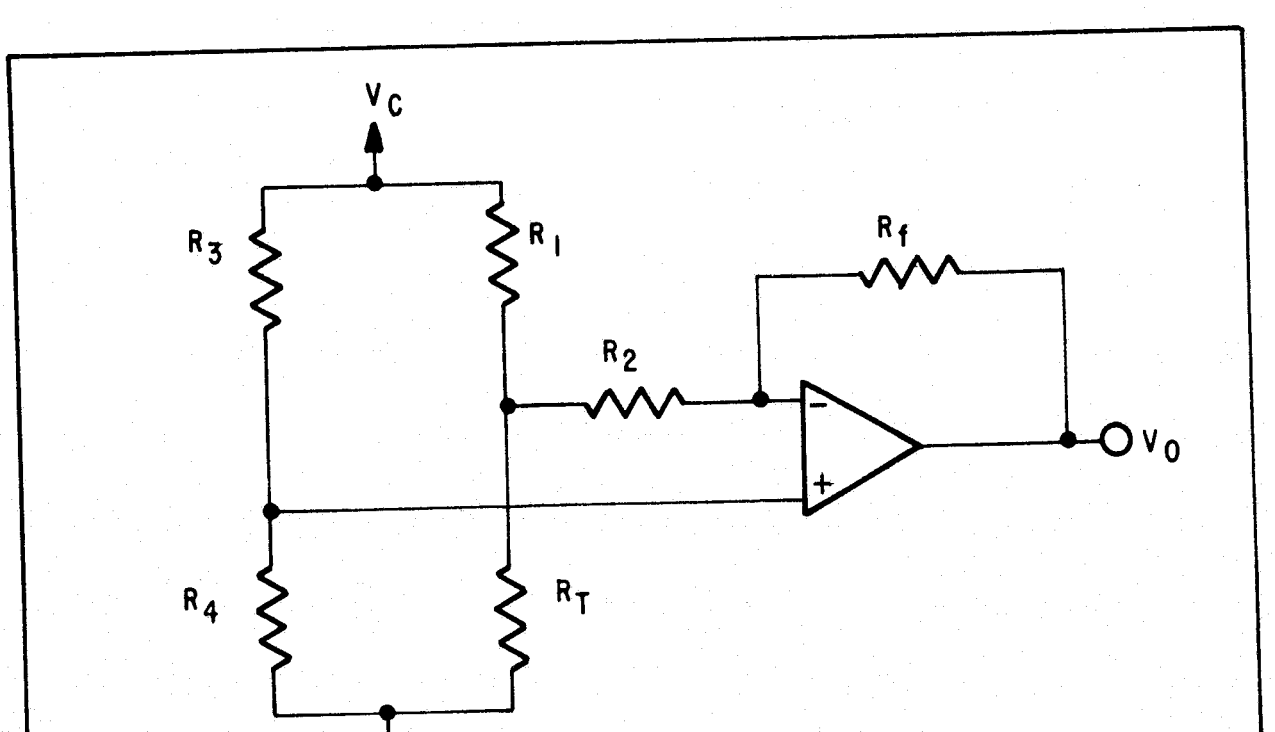

Figure 4-1 Absolute Temperature Monitor Functional Schematic

The performance requirements for the absolute monitor are stated as follows:

Range:	1.5 - 4.2°K
Accuracy:	0.1°K
Maximum Current through sensor:	10μA
Compatible with:	8 bit AD converter with 0 to 5 V input range

The error sources are discussed in the following paragraphs.

Starting with the operational amplifier, let us assume the use of a LM 725A which has a maximum input drift of 1μV/C. If an open loop gain of 100 is used (highest temperatures), then a 60°C amplifier temperature range will contribute an output error of 1.8 m°K.

Errors due to bridge power supply variations will be most significant at the highest temperatures and can be computed from the following expression:

$$\frac{dV_o}{dV_c} \approx \frac{R_f \frac{(R_1 + R_T)R_4}{R_3 + R_4} - R_T}{R_1R_T + R_1R_2 + R_2R_T}$$

Substituting the typical values for the highest temperature (maximum bridge unbalance) one obtains a sensitivity of:

$$\frac{dV_o}{dV_c} = 0.489$$

which means that a 1% change in V_c will produce a 0.489% change in V_o. A 1% power line regulation will produce no more than a 3.7 m°K error at the output (V_o).

A temperature coefficient for the 5 resistors of better than 50 ppm °K over a 50°K range will produce a worst-case error of 5 m°K.

Table 4-1 summarizes the various error sources and their effect on output accuracy. The total root sum square error of 12.7 m°K is pessimistic since nearly all inputs were taken at the worst case sensor temperature.

Table 4-1

ERROR BUDGET FOR ABSOLUTE MONITOR
(LM725A Op Ampl)

Source	Component Tolerance	Max Output Error (m°K)
Op amp input voltage drift	1μV/°K	1.8
Resistors (5 ea.)	50 ppm/°K	5.0
Bridge power supply	1%	3.7
Telemetry Resolution	8 bit	10.9
RSS Error		12.7 m°K

The absolute temperature monitor was breadboarded and temperature cycled to demonstrate that the amplifier as designed meets the requirements. Table 4-2a gives the values of the various components of Figure 4-1 that were used in the breadboard circuit. A LM212, which has characteristics similar to the 725, was used for the breadboard. The circuit was temperature cycled between -27°C and +82°C, while the sensor temperature was in the range 1.5°K to 2.17°K. The results are given in Table 4-2b and show a maximum change in output voltage of 14 mV. This voltage change corresponds to a 1.9 m°K shift over the temperature range tested. This test demonstrates that the output accuracy of the absolute monitor is well within the requirements.

Table 4-2(a)
BREADBOARD ABSOLUTE MONITOR

Circuit Element	Selected Value
Operation Amp	LM212 (similar to LM725)
R_1	1 M
R_2	1.200 K
R_3	765 K
R_4	6.424 K
R_f	477 K

Table 4-2(b)
TEMPERATURE CYCLING TESTS

R_T	Temp(K)	V_o (-27C)	V_o (21C)	V_o (82C)	ΔV_o
8488Ω	1.50	4.968	4.963	4.954	0.014
5064Ω	1.84	2.520	2.516	2.511	0.009
3464Ω	2.17	0.000	-0.003	-0.005	0.005

4.1.2 Differential Temperature Monitor

To monitor porous plug operation, the temperature difference across the plug is needed. This monitor must resolve better than 50 m°k. There is some question at this time whether a single differential monitor or 2 absolute monitors are best. If a resolution better than about 10 m°k is needed, the differential monitor must be used because of the telemetry channel resolution.

Figure 4-2 shows temperature resistance curves for two typical detectors. Data from these are tabulated in Table 4-3. The absolute temperature monitor provides a linear output to better than 1 m°k. If the gains of two detectors are matched by amplifying them at slightly different gains, a differential monitor can be made. The schematic is shown in Figure 4-3.

A1 and A2 are designed as described for the absolute monitor. The gains of A1 and A2 differ by about 1% to obtain an overall gain match. The resistors R_1, R_2, R_f, R_1', R_2', and R_f' are adjusted for a linear output. The outputs of A_1 and A_2 are differenced by A_3. Resistors R_g and R_s provide additional differential gain. R_r and R_t compensate for any offset bias remaining after the gains are matched.

In this arrangement the bridge is always near balance. Therefore, the error due to changing bridge power supply, V_c, will be much smaller. The unbalance for the absolute monitor is $\frac{3000\Omega}{5000\Omega}$ and $\frac{130\Omega}{5000\Omega}$ for the differential monitor. If an accurate differential monitor becomes useful, resistors with temperature coefficients matched to 4 ppm/°C are available from Vishay Resistor Products at very little more than the cost of normal metal film resistors. For a full scale of 200 m°k, the telemetry resolution becomes 0.78 m°k. The errors for the differential monitor are summarized in Table 4-4. The errors are evaluated for a $\pm$15°c temperature range since this is more typical of a spacecraft environment.

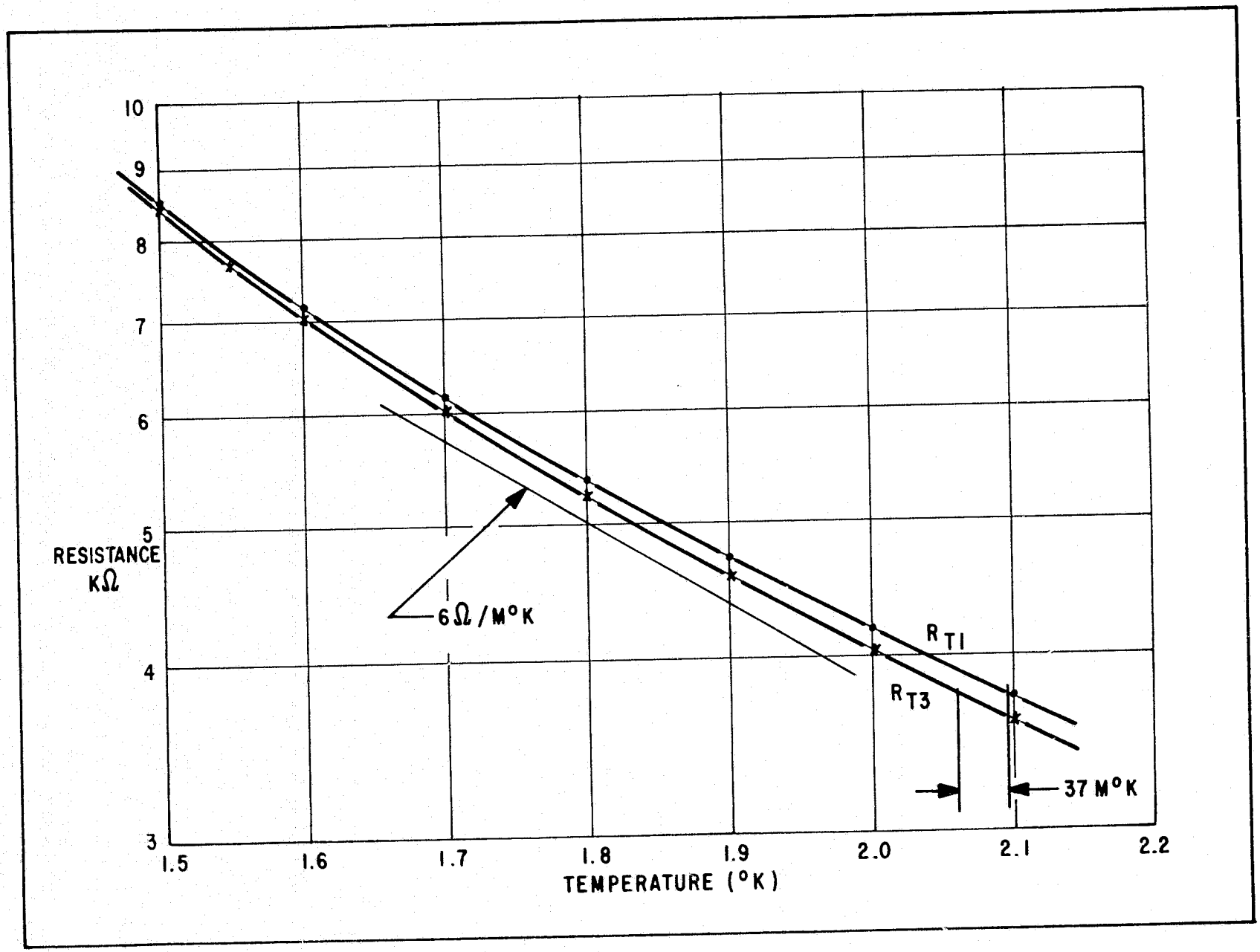

Figure 4-2 Typical Difference Between Two Detectors

Table 4-3

DETECTOR RESISTANCE DIFFERENCES

Temp. °K	R_{T1} Ω	R_{T2} Ω	R_{T1}x1.01 Ω	ΔR Ω	ΔR' Ω	ΔR'-$\overline{R}$ Ω	Gain Ω/m°k	Error m°k
1.50	8487.6	8422.9	8572.5	65.7	149.6	-20	15.6	-1.3
1.55	7770.8	7692.9	7848.5	77.9	155.6	-14	13.4	-1.0
1.60	7151.8	7060.5	7223.3	91.3	162.8	- 7	11.6	-0.6
1.65	6611.6	6508.2	6677.7	103.4	169.5	- 1	10.2	-0.1
1.70	6136.0	6022.4	6197.4	113.6	175.0	5	9.0	+0.6
1.75	5714.1	5592.4	5771.2	121.7	178.8	9	8.0	+1.1
1.80	5337.4	5209.7	5390.7	127.7	181.1	11	7.1	+1.5
1.85	4999.3	4867.3	5049.3	132.0	182.0	12	6.4	+1.9
1.90	4694.3	4559.5	4741.2	134.8	181.7	12	5.8	+2.1
1.95	4418.1	4281.8	4462.3	136.3	180.5	11	5.3	+2.1
2.00	4167.1	4030.3	4208.8	136.8	178.5	9	4.8	+1.9
2.05	3938.1	3801.7	3977.5	136.5	175.8	6	4.4	+1.4
2.10	3728.7	3593.2	3766.0	135.5	172.8	3	4.0	+ .8
2.15	3536.7	3402.6	3572.1	134.1	169.5	- 1	3.7	- .3
2.20	3360.2	3230.0	3393.8	130.2	163.8	- 6	3.4	-1.8

$\overline{R}$ = 170Ω

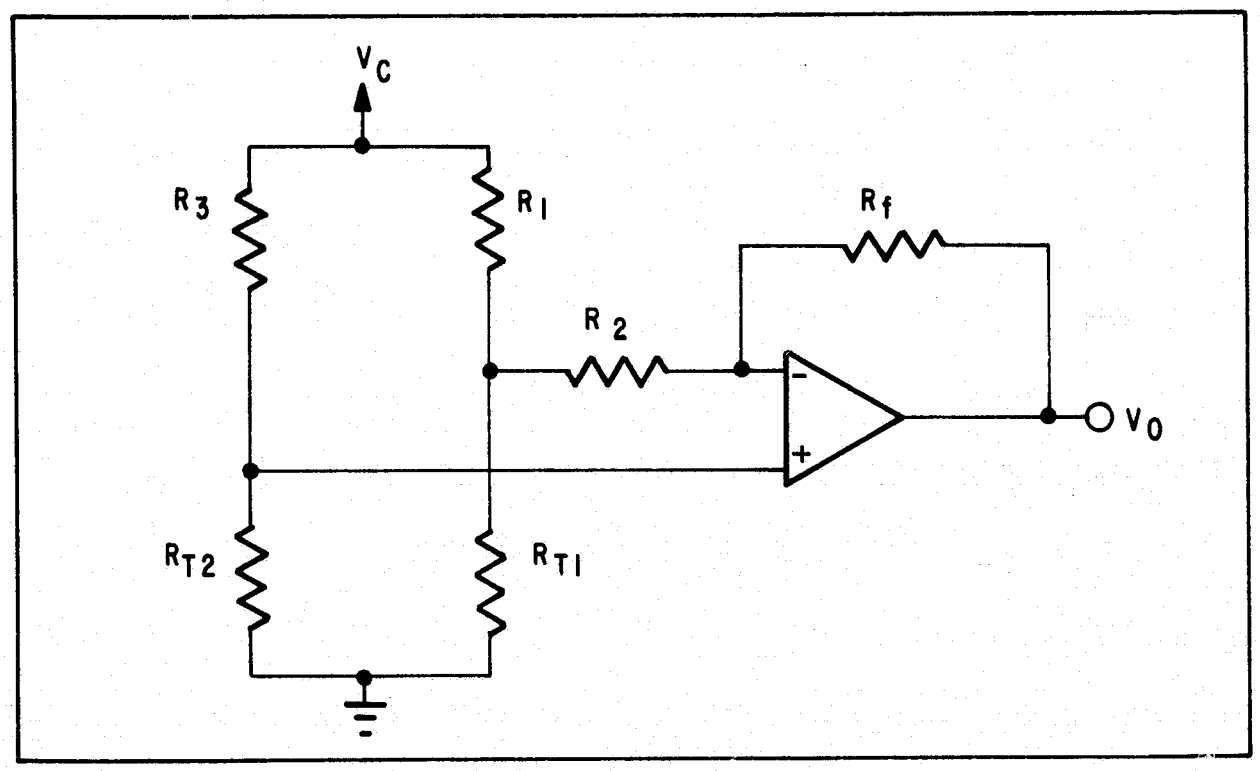

Figure 4-3 Differential Temperature Monitor Functional Schematic

Table 4-4
ERROR BUDGET FOR DIFFERENTIAL MONITOR

Source	Component Tolerance	Error (m°k)
Operational amplifier input Voltage Drift	1μV/°C	0.54
Resistors (10)	4 ppm/°C	0.76
Bridge Power Supply	1%	0.16
Telemetry Resolution	8 Bit	0.78
RSS ERROR		1.23

This monitor nearly achieves the 1 m°k goal needed if a high conductance metal plug were used. All parts are consistent with aerospace standards and are nominal in cost.

4.2.1 Thrustor Design

The Stanford thrustor is designed to achieve linear differential thrust. Differential thrust is obtained by directing continuous helium flow differentially through two opposing nozzles. The thrustor uses a moving plunger which differentially restricts the helium flow through the two opposing nozzles at each end (Figure 4-4). Flat rather than hemispherical or conical ends are used on the plunger which reduces requirements on machining and assembly accuracy.

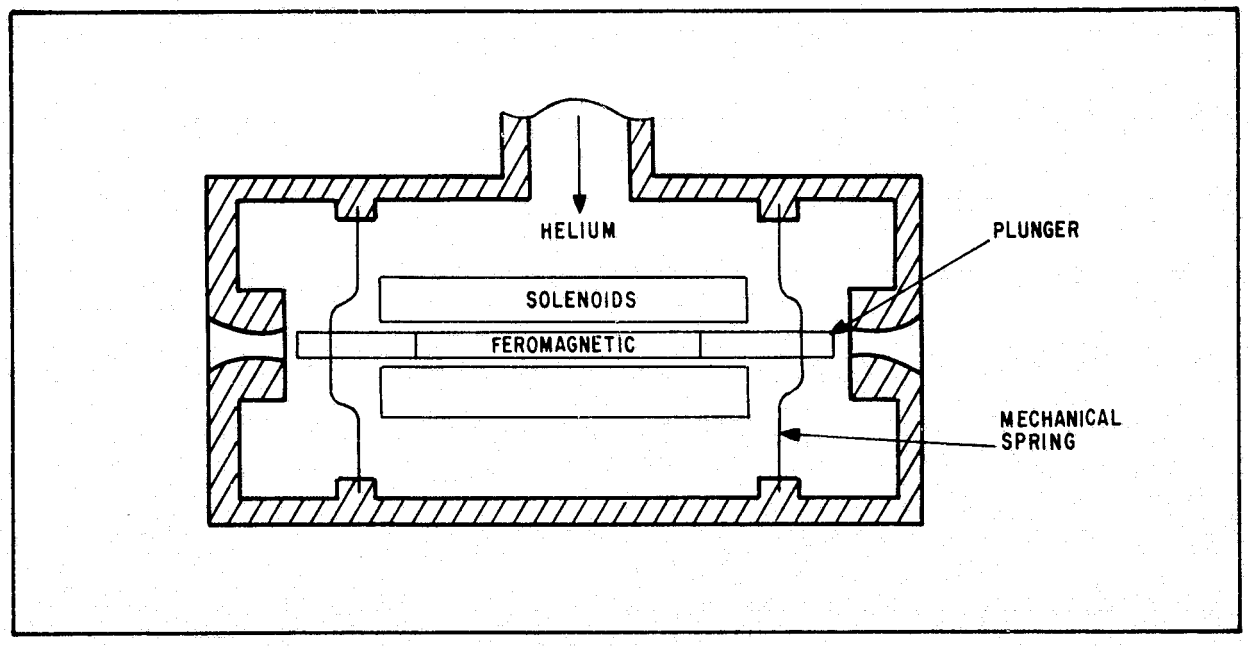

Table 4-4 Thrustor Design Concept

The plunger is fabricated from ferromagnetic material. Motion is obtained by adjusting currents in three solenoids concentric to the plunger axis. Mechanical leaf springs are used to provide the plunger centering force which balances the force produced by the magnetic fields of the solenoids. Provision has also been made for direct position readout by use of a capacitive mechanism. One plate of a capacitor is mounted on the plunger arm, the other being in a fixed position. The position of the plunger is directly proportional to the capacitance measured across the plates.

The plunger full open position can be estimated as follows. As the plunger moves toward the nozzle, the flow passage between the plunger face and nozzle entrance begins to restrict the flow of gas through the nozzle (Figure 4-5). The effective cross sectional area of the "restrictor" is

$$A_R = d\ell$$

where d is the diameter of the plunger face and ℓ is the distance between the plunger face and the nozzle. For full flow through one nozzle, the distance of the plunger from the nozzle should provide a restriction area at least as large as the real nozzle throat area. For the nozzle:

$$A_N = \frac{\pi D^2}{4}$$

where D is the smallest diameter of throat of nozzle. Then for equivalent areas:

$$A_R = A_N$$

or

$$\ell = \frac{\pi D^2}{4d} = .059 \text{ cm}$$

for the Stanford designed thrustor. Thus for the differential thrustor, the plunger motion should be at least $\pm$ 0.06 cm for full flow through either nozzle.

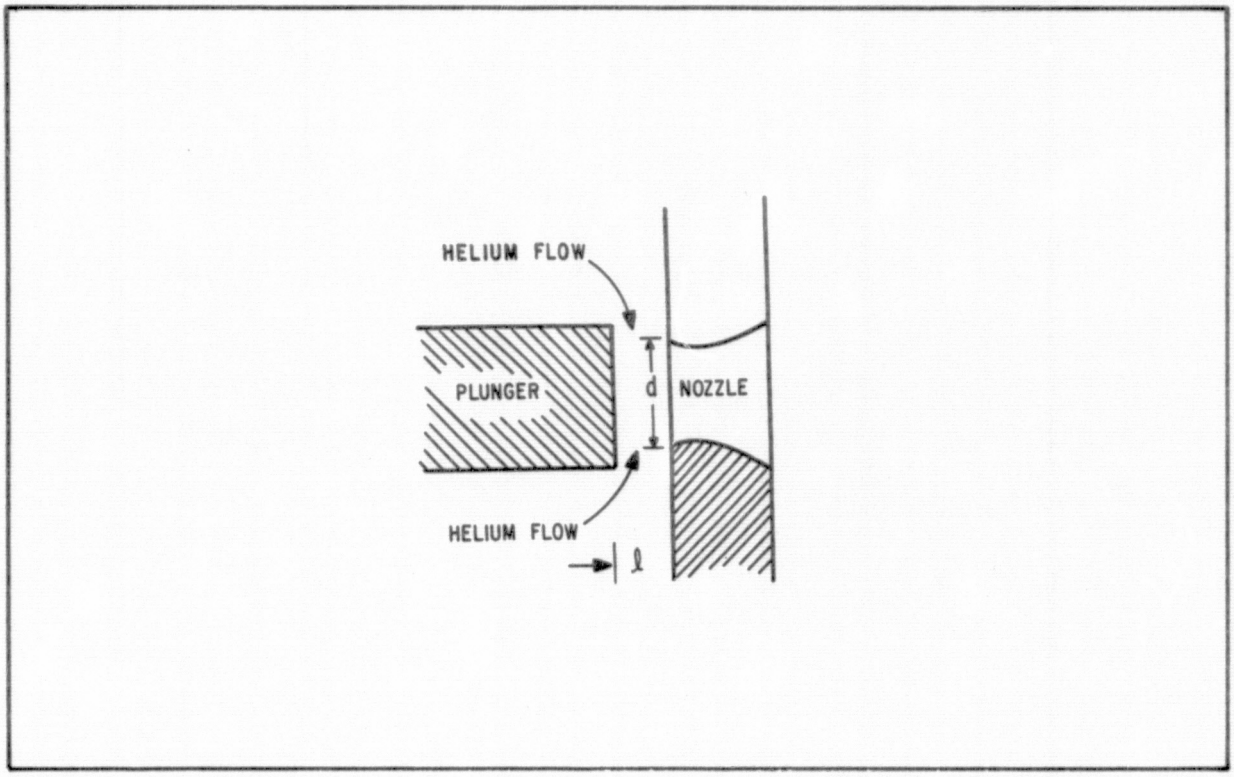

Figure 4-5 Effective Restrictor Area

4.2.2 Nozzle Design

The nozzle design of the Stanford thrustor is based on the usual equations for one dimensional isentropic nozzle flow as shown in Table 4-5. The throat must be sized to pass the expected helium boiloff gas flow at an appropriate flow rate.

For the GP-B flight, the heat to the helium is expected to be on the order of 75 mwatts which would generate approximately 3.4×10^{-3} grams/sec of boiloff gas. With two thrustors per axis, each thrustor must then pass 5.6×10^{-4} gms/sec at nominal plenum pressures of 1 to 5 torr. The plenum pressure must be kept low to ensure proper performance of the porous plug which will operate at pressures around 20 torr.

Table 4-5

ONE DIMENSIONAL ISENTROPIC NOZZLE FLOW EQUATIONS

Conservation of Energy

$$h_o = h_+ V^2/2$$

h_o = stagnation enthalpy
h = local enthalpy

Conservation of Mass

$$\dot{M} = \rho v A$$

$\dot{M}$ = mass flow rate
ρ = flow density
v = flow velocity
A = cross sectional nozzle area

Temperature, Pressure and Density at any point in nozzle can be related to entrance parameters as follows

$$T_o/T = 1 + [(k-1/2)]\ M^2$$

$$P_o/P = (To/T)^{\frac{k}{k-1}}$$

$$P_o/P = (To/T)^{\frac{1}{k-1}}$$

where k = ratio of specific heats = Cp/C_o
Cp = specific heat at constant pressure
C_V = specific heat at constant volume
M = local mach number
(at throat M=1, choked conditions)

For one dimensional isentropic nozzle flow, the diameter of the throat of the nozzle can be found from the following derivation. The theoretical mass flow in the throat is given by $\dot{M} = \rho_* u_* A_*$

where ρ_* gas density in throat,
u_* gas velocity in throat,
and A_* cross section area of throat.

The gas velocity in the throat u_* is the critical or sonic velocity for the chocked flow conditions created with the nozzle and is given by $u_* = [\gamma RT_*/M]^{1/2}$ where R is the gas constant, R_* is the temperature in the throat, M is the molecular weight and $\gamma = C_p/C_o$ is the ratio of the specific heats at constant pressure and volume. The gas density ρ_* in the throat is related to the pressure in the throat as $\rho_* = \frac{P_* M}{RT_*}$. Using $A_* = \frac{\pi}{4} D_*$, substituting and solving for D_* gives

$$D_* = \left[\frac{4}{\pi} \frac{\dot{M}}{P_*} \left(\frac{RT_*}{M}\right)^{1/2}\right]^{1/2}$$

From Table 4-5, the temperature and pressure in the throat (P_*, T_*) can be found from the plenum pressure and temperature $P_o T_o$. With a gas temperature of 300°K, with M = 1.667 for helium, it is found that

$$T_* = 225K$$
$$\text{and} \quad P_* = \frac{P_o}{2.053} \text{ dyne/cm}^2$$

Converting P_o from dyne/cm^2 to torr and substituting T_*,P_* the diameter of the nozzle throat is given by

$$D_* = 10.9 \left(\frac{\dot{M}}{P_o}\right)^{1/2} \text{cm} \qquad P_o = \text{plenum pressure in torr}$$

Most nozzles will not pass the ideal mass flow

$$\dot{M} = p_* u_* A_*$$

but some fraction of this flow. This is due to surface irregularities in the nozzle, viscous boundary layer formulation and other interesting phenomena. This is accounted for by assigning a coefficient of discharge C_D to the nozzle. The actual mass flow $\dot{M}_a$ is then found from

$$\dot{M}_a = C_D \dot{M}$$

Thus, the nozzle throat diameter is then

$$D_* = 10.9 \left(\frac{\dot{M}_a}{C_D P_o}\right)^{1/2} \text{cm}$$

By plotting families of curves for nozzle throat diameters against thrustor plenum pressures and helium mass flow rates, a throat diameter can be chosen that would produce plenum pressures in the nominal range of 1 to 5 torr for nominal gas flow. The Stanford thrustor uses a D_* = .137 cm. Additional care usually must be taken in choosing the throat radius of curvature, nozzle half angle and expansion ratio but these are not as important in small nozzles.

4.2.3 Helium Gas Flow Calibration Instrumentation

The objective of the calibration of the Stanford thrustor was to measure gas flow rates as a function of plenum pressure, plunger-nozzle distance and gas temperature. Figure 4-6 depicts the test arrangement of the thrustor used for helium gas flow calibration.

The plunger in the thrustor is spring loaded with mechanical leaf springs which provide the centering force for the plunger in the thrustor assembly. A micrometer head was installed on one end of the thrustor. The tongue of the micrometer was free to move through the o-ring seal and push the plunger towards the nozzle.

The mechanical springs provided the restoring force when the micrometer tongue motion was reversed. There appeared to be no play in the plunger-micrometer system; the plunger always resting snugly against the flat end of the micrometer tongue and the plunger and micrometer tongue moving together, both toward and away from the nozzle face. The nozzle-plunger distance with the plunger in the centered position could be adjusted by adjusting the threaded nozzle mount in its hole so as to give maximum throw to the plunger. The throw was limited only by the leaf spring on the plunger which would deform if stretched too far. The travel was adjusted to give over 1.50 mm of throw in this calibration procedure.

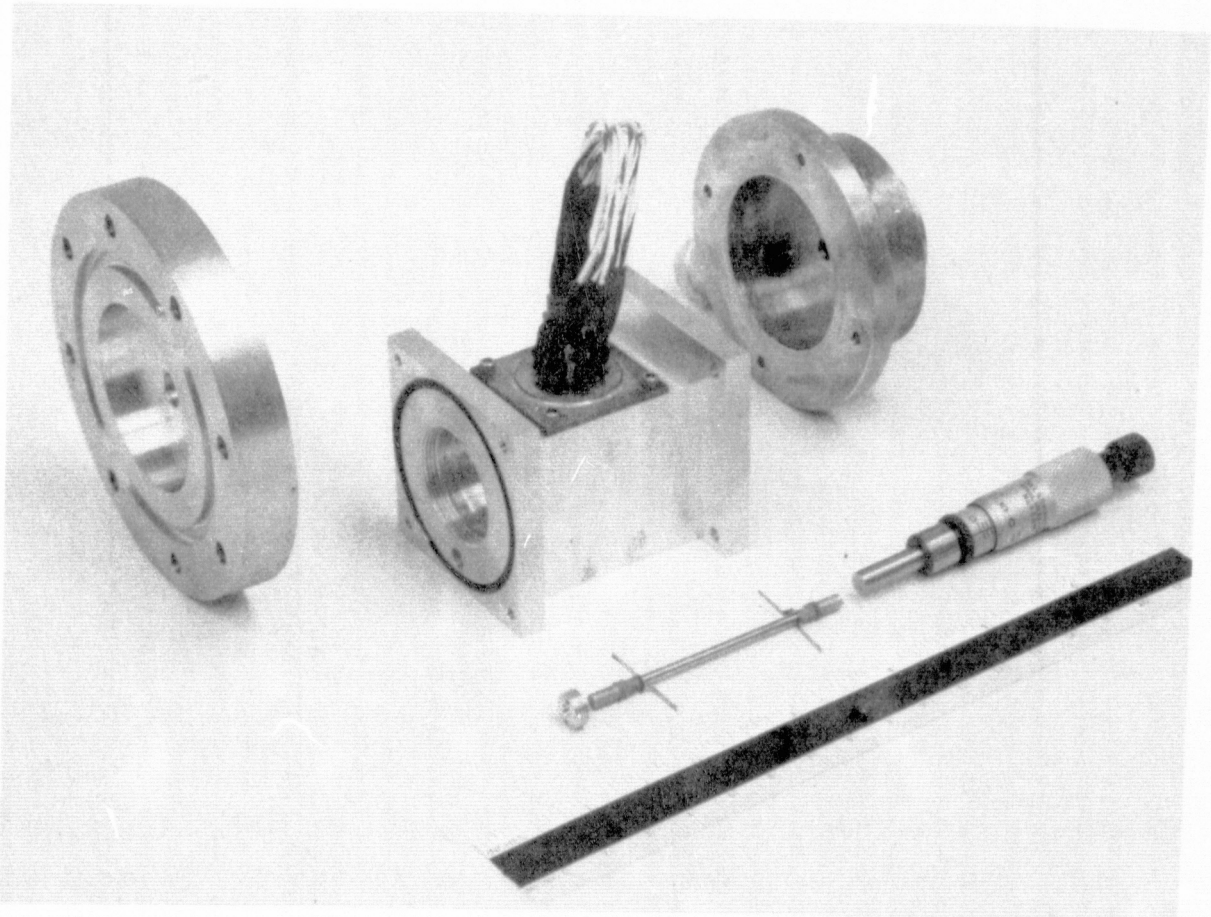

Figure 4-6 Stanford Thrustor Test Arrangement Disassembled

The plenum pressure was measured with a SenTran pressure transducer PN10050, SN101, calibrated from 0.1-100 torr in air. The sensor was calibrated at BBRC for helium gas usage over the range 0.1-17 torr at which point the thermocouple's amplifier circuit saturated. Additional data on this pressure transducer is contained in Section 4.3. The sensor was mounted on the opposite end of the thrustor near the micrometer head (Figure 4-7). Gas was admitted to the thrustor through a fitting in the center of the thrustor. It was then directed to each end by two .46 cm dia, 2.6 cm long channels. Using ordinary viscous flow equations for tubes of this size, the pressure drop between the entrances of the gas and the nozzle, at the maximum flow rates (6.48×10^{-4} gms/sec) is less than 1% of the inlet pressure.

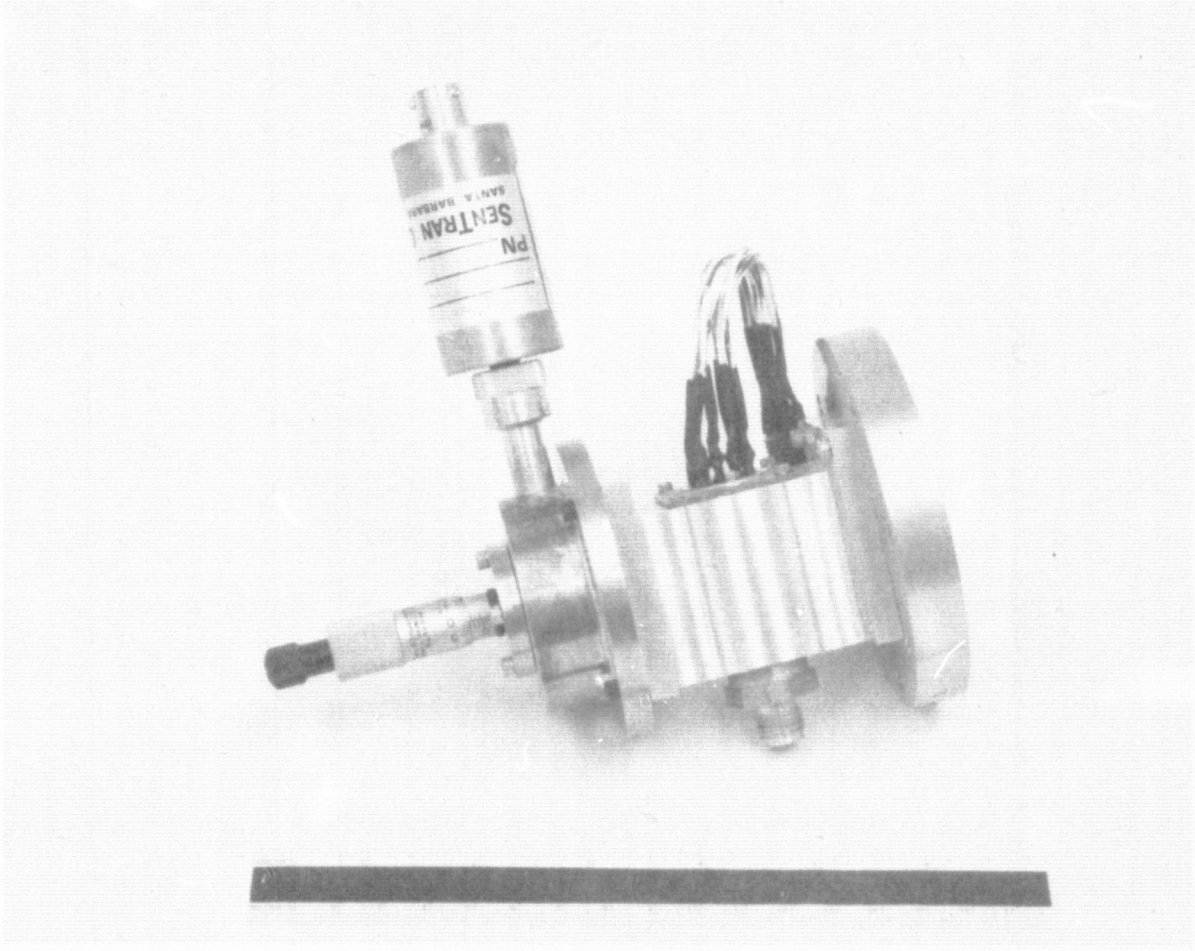

Figure 4-7 Assembled Stanford Thruster Test Arrangement

Two transition pieces were used during the calibration procedure. The transition piece connected the thrustor to the side port of the high vacuum chamber. Initially, the transition piece was a tube 4.45 cm dia x 6.05 cm long flanged at each end (not shown in the figure). The nozzle was screwed into the flange mating to the thrustor. A fitting was brazed into the side of the tube which would accept a SenTran P/N10150 pressure transducer. This transducer is a temperature compensated thermocouple pressure gage sensitive over a pressure range 10^{-5} to 0.1 torr with a 0-5 DC log output. The sensor was calibrated with helium gas down to 1.0^{-5} torr. This sensor was used to measure the downstream expansion pressure of the nozzle.

A second transition piece was used to study the effect of the limited pumping capacity of the tube of the first transition piece. This tube would cause higher pressures at the nozzle which might inhibit gas flow through the nozzle. The second transition piece was a simple flange which attached to both the vacuum port and the thrustor. Again the nozzle screwed into the flange. In this configuration the SenTran P/N10150 pressure transducer was mounted inside the vacuum chamber approximately 5 cm away from the nozzle and slightly to one side. Results from tests using both transition pieces are presented below.

The thrustor assembly was attached to a side port of the NASA 10' x 15' high vac chamber at BBRC. This chamber was two NRC-HS, 32 inch diameter, liquid nitrogen trapped, water baffled, oil diffusion pumps. These pumps have a combined nominal pumping speed of 60,000 liters/sec of air at 1×10^{-5} torr. Measured throughput of the entire vacuum system with helium gas was 13,200 liters/sec at 1×10^{-5} torr.

For tests of flow rate as a function of gas temperature, a liquid nitrogen chiller was used. Cooling coils were wrapped around the

thrustor unit. Nitrogen gas flowed through a heat exchanger immersed in a LN_2 bath and then through the cooling coils. A heat exchanger was also used to precool the flowing helium gas. A temperature sensor monitored the thrustor wall temperature, while another thermocouple provided a feedback to control the cooling gas flow. The temperature could be controlled to $\pm$2K over the range of the gaseous helium flow rates used.

The helium flow rates were measured with a Hastings Mass Flowmeter Model #ALL-500-PGX using the Hastings Flow Transducer Type H-500M, which had been factory calibrated for methane. This flow meter is both temperature and pressure insensitive over ranges much wider than used in the calibration. For this type of flow meter, any gas could be used; the correction factor was given by Hastings. The Hastings flow meter was also calibrated at the end of the thrustor tests against a Precision Scientific Test wet flow meter. The two flow meters agreed over the full scale range of the Hastings to within 3%.

The helium gas used was research grade quality. The gas circuit was composed of the compressed gas bottle, helium regulator, gas flow meter, Granville Phillips variable leak valve, thrustor and vacuum chamber. Gas was allowed to flush the system for thirty minutes before any data were taken. The entire system was checked for gas leaks by advancing the plunger up tight against the nozzle. No measurable flow was detected by the flow meter, even at pressures up to 300 torr in the thrustor body. Thus, all measured gas flow rates were due to flow only through the nozzle itself. Leaks into the gas lines from the surrounding environment were also found to be negligible by pumping out the gas fill line back to the variable leak valve. After locking the plunger up tight against the nozzle face, there was no noticeable increase in the equilibrium pressure of less than .05 torr.

4.2.4 Helium Gas Mass Flow Calibration Data

Helium gas flow calibration data were taken to determine the mass flow through the nozzle as a function of plenum pressure, plunger-nozzle distance, and temperature variation. Total flow rates for a two nozzle thrustor were plotted to determine total flow variation under plenum pressure and temperature changes.

4.2.4.1 Variation With Pressure

In his thesis, Bull presents mass flow versus plenum pressure for helium pressures up to 3.2 torr. One of the prime objectives of this study was to extend the helium pressure range covered. Unfortunately, due to limitations in the range of the flow meter available, the measurements could only be extended to 5.6 torr, the plenum pressure corresponding to the highest measurable flow rate 6.48×10^{-4} gms/sec. Figure 4-8 presents data from three different sets of data and also for comparison, Bull's data. For pressures above 1.5 torr, the flow rate increases linearly with plenum pressure. Bull's data also shows a linear increase with pressure above 1 torr, but his slope is slightly steeper than that measured in this experiment. These differences may be attributed to the different plunger-nozzle orientations as well as pressure measuring techniques used in the two experiments.

The data were taken with the plunger in the full open position. This position corresponded to a plunger nozzle distance of approximately 1 mm. For distances greater than 1 mm, movement of the plunger had no discernible effect on the flow rate or pressure. In Bull's experiment, however, the mass flow data were not taken using the thrustor. The nozzle was inserted into one end of a specially constructed thrust balance arm used for thrust measurements. A special tap and tubing for pressure measurements was installed in the thrust balance arm containing the nozzle in

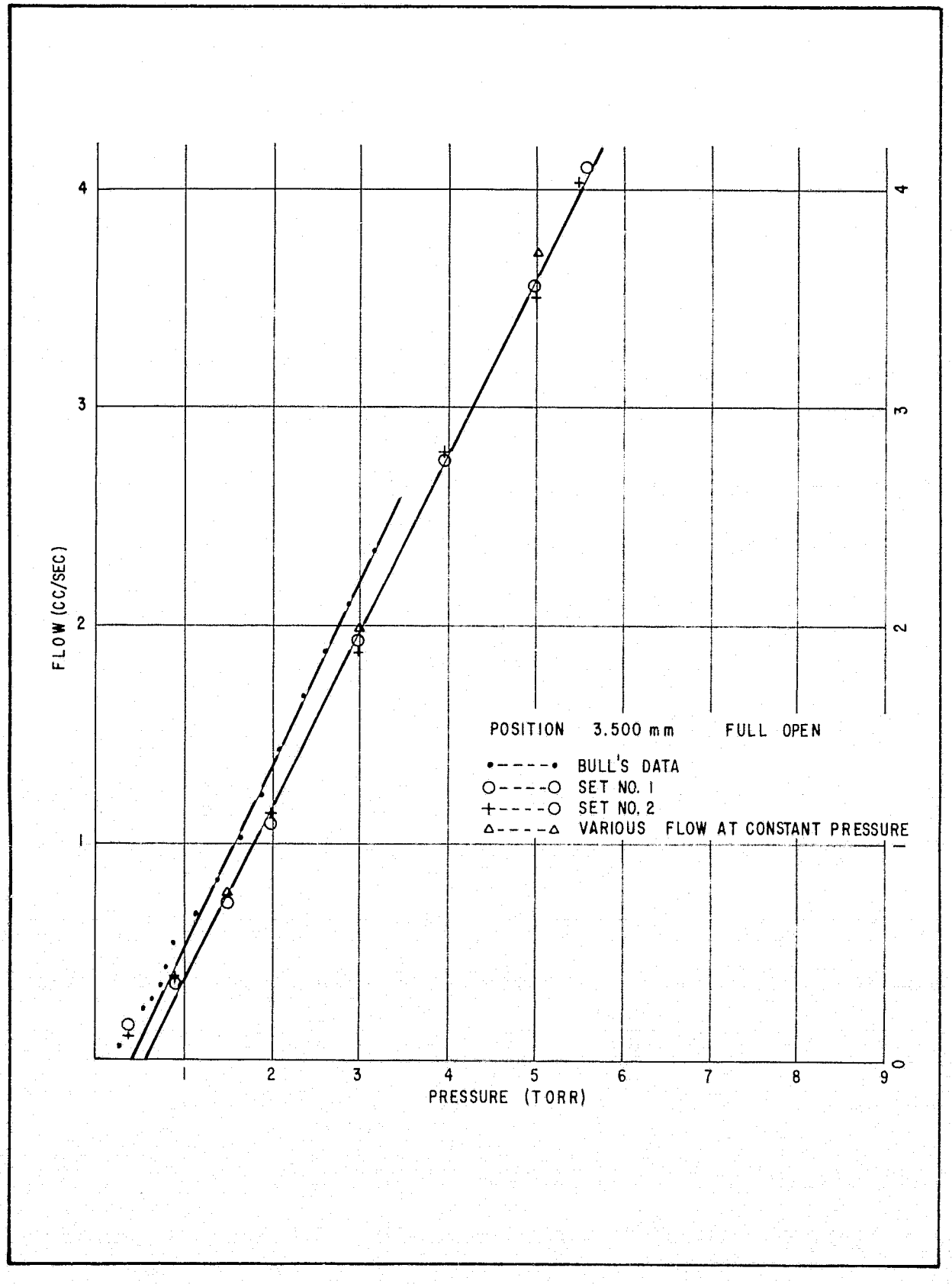

Figure 4-8 Mass Flow Versus Plenum Pressure

order to measure plenum pressures using an oil manometer. Whether corrections were made to the pressure measurements for the long tube length used is not discussed in the thesis. Thus, the discrepancies in both the absolute measurements and the slope of the linear segment could be due to non-corrected pressure measurements. It is also possible that the flow meters used in the two experiments read differently, even though both were calibrated by the manufacturers.

4.2.4.2 Variation with Plunger Nozzle Distance

In space, the thrustors will operate at a constant pressure, which will depend on the temperature of the dewar, heat leak, vent tube size and length, etc. It can be anticipated that the valves will operate around 5 torr in order to provide a sufficient pressure drop along the vent lines for the gas flow expected. The plug is expected to have an unsaturated pressure in the range 20-30 torr. Thus, data were taken on the variation of mass flow rate with plunger position for a few fixed plenum pressures.

From the data plots, three regions of operation were apparent. For small plunger-nozzle distances less than approximately 0.1 mm, the slope of the line decreases with decreasing distance. As the plunger-nozzle distance is increased, the mass flow rate grows linearly with the plunger position up to a falloff point. For distances longer than falloff point, the mass flow increases more slowly, gradually becoming constant for plunger-nozzle distances longer than 1 mm.

The shape of the curve appears to have the following explanation. At small plunger-nozzle distances, choked flow is not fully developed in the nozzle, but may be developed at the plunger face

edge. The rate of increase of flow is proportional only to the increased plunger-nozzle spacing. The linear portion of the curve probably represents fully developed choked flow in the nozzle. The plunger face acts as a restricter, causing a pressure drop from normal plenum pressure. The effective pressure seen by the nozzle is less than plenum pressure and increases linearly with increasing plunger-nozzle distance up to the falloff point. At distances larger than the falloff position, the effective nozzle plenum pressure becomes less sensitive to position of the plunger and eventually the plunger distance has no effect on the nozzle operation.

4.2.4.3 Temperature Variation

Temperature has little effect on the absolute value of mass flow as function of plunger position for a given plenum pressure. The curves for both T = +20C and T = -20C coincide over the entire position range to within ± 5%. It is apparent from the plots, however, that the T = -20C data has an apparent change in the slope of the curves occurring at about 0.175 mm relative position. This change occurs at the same position irrespective of plenum pressure. The cause of the slope change cannot be explained at this time. Further study is recommended to determine first whether this anomaly is real. If it is a real phenomenon, what are its causes and how might it effect the thrust of the thrustor. The effect on mass flow measurements is small. The difference between total flow rates for T = +20C and T = -20C is smaller than 5% as is discussed below.

4.2.4.4 Total Flow

The total flow per thrustor is the desired flow rate to be measured. The total flow rate is the sum of the flow rates

through both nozzles in the thrustor. As one nozzle is being restricted by the plunger, the other nozzle is being opened up to larger flow rates. By choosing the initial plunger-nozzle distance with the plunger centered, a flow rate independent of plunger position can be achieved.

Inspection of the various plots of flow versus plunger-nozzle relative position shows that most curves are linear in the region of 0.05 to 0.35 mm relative position. The total flow rate of a thrustor is the sum of the flow from the two nozzles. The largest change in total flow rates with plunger position was 15.4% for a 5 torr plenum pressure vibration. This could be reduced considerably by going to a plenum pressure of 7.0 torr and reducing the plunger-nozzle range by 0.05 mm. This correction would give a variation of 2.5% in flow rate over the plunger-nozzle position range used. In this case, the total flow would be approximately 3.6 cc/sec which corresponds to 5.83×10^{-4} gms/sec of helium gas per thrustor. Thus, a six thrustor array would give 3.50×10^{-3} gms/sec flow rates, which would be the boiloff rate for a helium dewar with approximately 77 mwatts heat leak. Larger flow rates could be obtained if necessary by enlarging the thrustor nozzle. For now, it is important to realize that over a limited range of nozzle-plunger positions, the flow rate is independent of position to within 5%.

4.2.5 Summary

Tests at BBRC have confirmed the data gathered by John Bull at Stanford on the mass flow rates of the thrustor as a function of plenum pressure. The data has been extended to include flow

rate as a function of plunger-nozzle distance for given plenum pressure and gas temperature. Temperature effects were small, less than 5% variation in flow rate on decreasing the temperature from 293°K to 253°K. The total flow rate for a two nozzle distance is chosen to take advantage of the linear portion of the flow rate versus position curve. This parameter must be considered when designing the nozzle for thrust so as to achieve desirable thrust levels and flow rates within a given set of helium dewar operating conditions. The maximum flow rates of the nozzle must accommodate the normal boiloff helium gas flow rates.

4.3 PRESSURE SENSOR

A pressure sensor is needed on a flight liquid helium dewar to help monitor the performance of the porous plug. For the GP-B mission, the pressure sensor would also be used in conjunction with the directional thrustors to determine helium gas mass flow rates as described in Section 4.4 below. A survey of commercially available pressure sensors has led to the selection of a fully qualified sensor that could be used on the GP-B mission. This pressure sensor was obtained and tested at BBRC in conjunction with the Stanford thrustor tests.

4.3.1 Pressure Sensor Description

The pressure sensor was obtained from the SenTran Company, Santa Barbara, California. The transducer P/N10050 was designed for applications where minimum weight and size are desirable. The sensing element of the transducer is a constant temperature bead thermistor. The power necessary to keep the thermistor at a particular temperature depends on the pressure and thermal conductivity of the gas used. A solid state thermostat regulates the internal sensor housing temperature and makes the calibration of the transducer independent of outside temperature changes.

The overall pressure range of the sensor is 10^{-4} to 10^{-2} torr in air. The sensor provides a 0-5 volt readout and can be adjusted during fabrication for a minimum range of one decade of pressure above 10^{-2} torr. Table 4-6 shows the specifications as provided by the manufacturer. Figure 4-9 shows the size of the transducer.

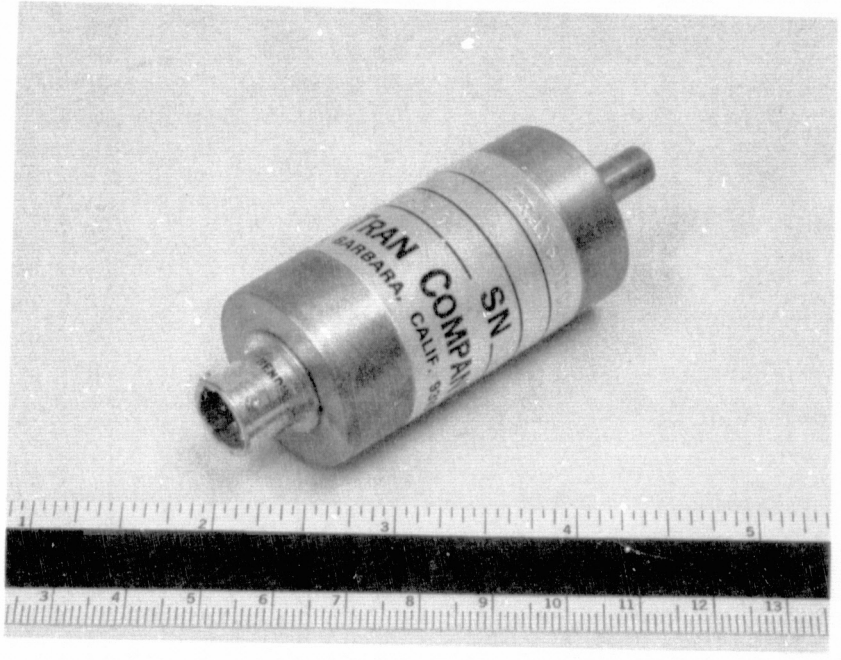

Figure 4-9 SenTran Pressure Transducer P/N10050

Table 4-6

SPECIFICATIONS

SENTRAN VACUUM TRANSDUCER P/N10050

Maximum measurement range	10^{-4} to 10^{2} torr
Minimum measurement range	any pressure decade in the range 10^{-1} to 10^{2} torr
Most sensitive measurement range	10^{-4} to 10^{-2} torr
Output voltage	0 to 5 volt DC
Output impedence	100 ohm $\pm$ 10%, short proof
Accuracy	depends on pressure and range (typically $\pm$ 2% to 5% of reading)
Response time	.1 second at 10^{-3} torr .02 seconds at 10^{2} torr
Supply voltage	+12 v+30% -10% (other supply -12 v $\pm$30% voltages on request)
Supply current	+30 mA at upper, +80 mA at lower limit of temperature range -5 mA (1.0 w max)
Temperature range	
Operating	-55C to +75C
Compensated	any 100°C span in operating range
Vibration	20 g's, 20 to 2000 Hz per Mil-E-5272C
Shock	50 g's, 11 ms per Mil-E-5272C
Weight	65 grams

4.3.2 Pressure Sensor Calibration

The pressure sensor as ordered called for a 0.1-100 torr pressure range with a 0-5 volt output over this range. The sensor was calibrated in air by the manufacturer. The pressure calibration was repeated at BBRC using helium gas. Figure 4-10 shows the transducer output as a function of pressure. The sensor output saturates at approximately 18 torr in helium. This calibration was repeatable and stable over a period of weeks. For flight, the sensor will be set for 0.5 to 50 torr. This will provide a resolution of about 0.2 torr in the normal operating range.

4.4 GAS MASS FLOW METERS

A survey of currently available mass flow meters was made. Most of the current laboratory gas flow meters systems available take advantage of the thermal conductivity of the flowing gas. These meters commonly have a heater element and temperature sensing devices which measure the rate at which heat is lost from the hot element. The heat loss is directly proportional to the mass flow rate and is independent of the gas pressure.

Other systems use ultrasonic waves. The change in the frequency of a sonic wave propagated in a direction nearly perpendicular to the gas flow is a function of the gas density and the flow rate. This method has the disadvantage that the readings are proportional to the volume flow rate and are very sensitive to the gas pressure at the measuring element.

Neither of these systems could be considered for GP-B because they have a pressure drop of 50 torr. The total pressure drop in the GP-B mission is about 20 torr and most of this must be reserved for the dewar piping and the proportional valve. The thermal conductivity units consume up to 15 watts which could be a problem.

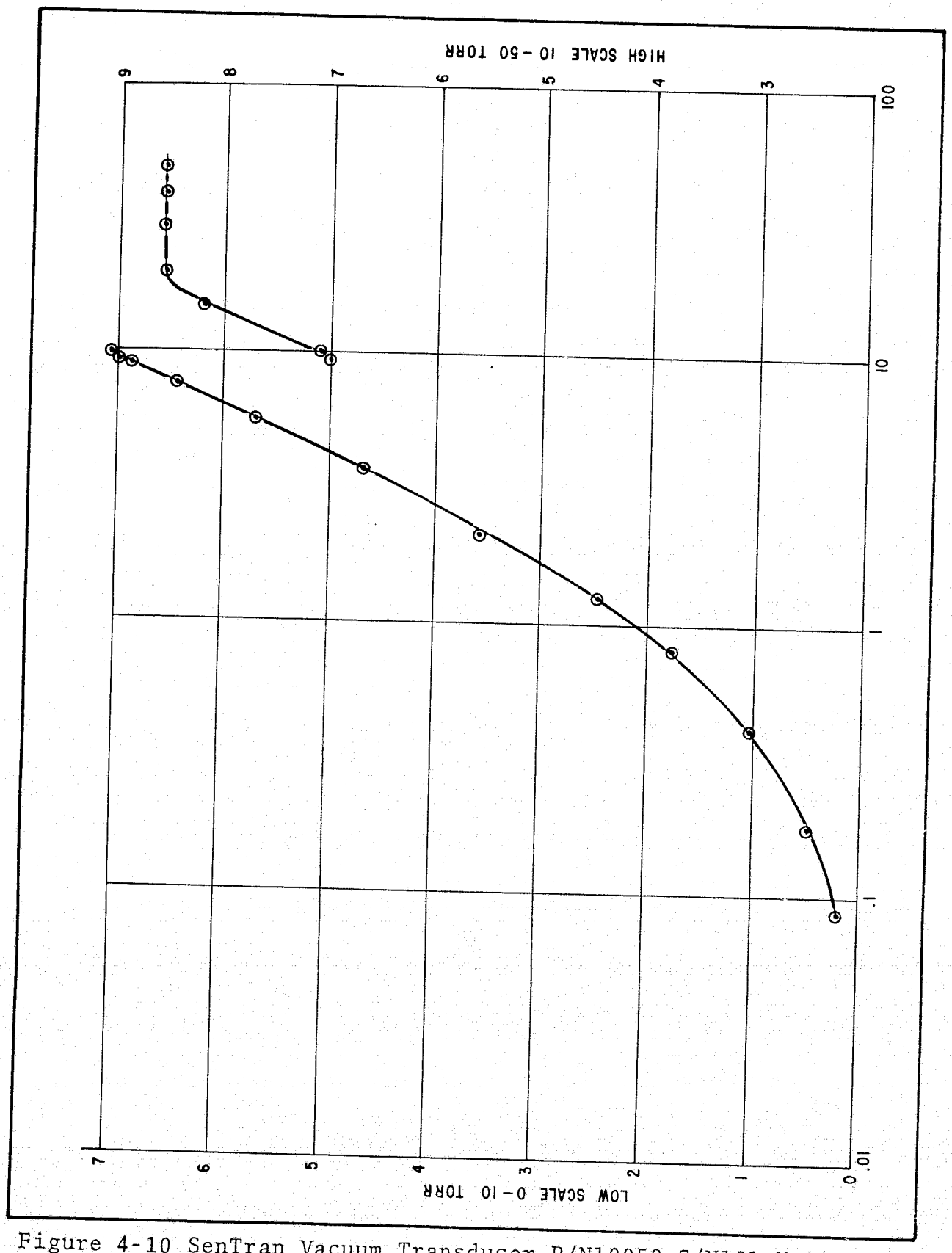

Figure 4-10 SenTran Vacuum Transducer P/N10050 S/N101 Helium Calibration

Sonic systems are better suited for space use. However, no device was found in the survey that was spaceflight designed or was usable at the low flow pressure and rates of the long life dewar. Sonic systems are disadvantaged further in that the readout is not directly in mass flow rates. Since no off-the-shelf design was suitable, undeveloped techniques were considered. It was discovered on a reading of John Bull's thesis "Precise Attitude Control of the Stanford Relativity Satellite," Stanford University 1973, that the thrustor developed at Stanford had an approximately linear mass flow rate versus pressure upstream of the nozzle. Further study of the results presented in this thesis led to the conclusion that the Stanford thrustor could be used as a mass flow meter. The mass flow rate is determined by measuring the upstream (plenum) pressure with the transducer discussed above.

Section 5

HELIUM DEWAR INSULATION TASK

This section describes the multilayer insulation system which was installed on the Ball Brothers Research Corporation's liquid helium dewar.

5.1 DESCRIPTION OF LHe DEWAR

The dewar which was insulated under this phase of the contract has a forty inch diameter by forty inch long pressure vessel (PV) with an eighteen inch cavity in the center of the PV. The PV is supported by six fiberglass supports and six retractable titanium supports which are attached to the fifty-four inch diameter by fifty-six inch long outer shell. The dewar is of all aluminum construction except for the plumbing which is stainless steel. The dewar contains six hundred and fifty liters of liquid helium in either the normal or superfluid helium states. The insulation system consists of four multilayer insulation blankets of mylar aluminized on both sides and spaced by dacron net. The insulation blankets are spaced by three vapor cooled shields which are supported by the fiberglass supports and in turn cool the supports. Figure 5-1 is a photograph of the assembled dewar. Table 5-1 summarizes the dewar thermal characteristics, and Figure 5-2 shows the dewar schematically.

The primary purpose of the liquid helium dewar is to demonstrate that a one year life-time dewar which can withstand launch environment is not only feasible but is available.

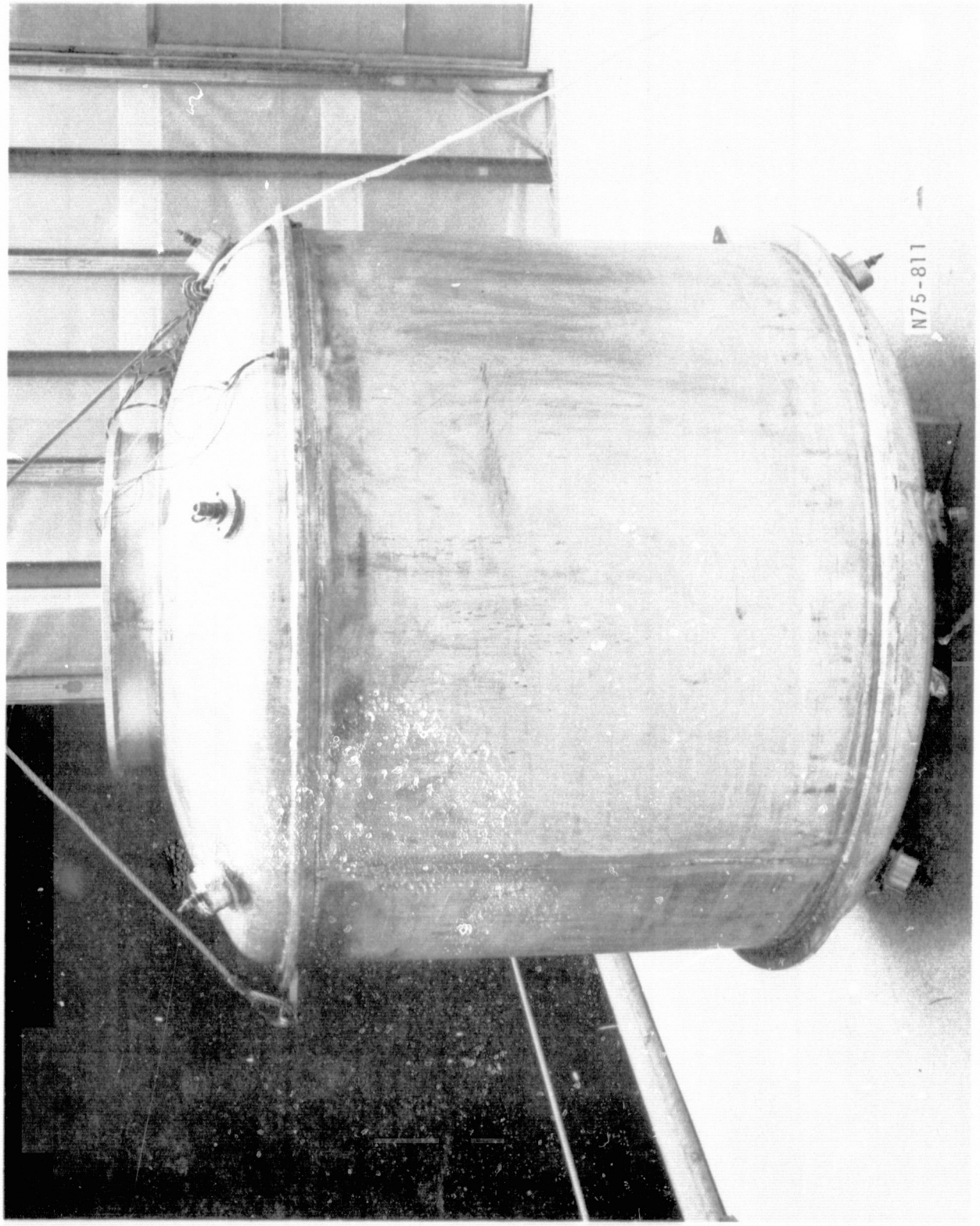

Figure 5-1 Liquid Helium Dewar

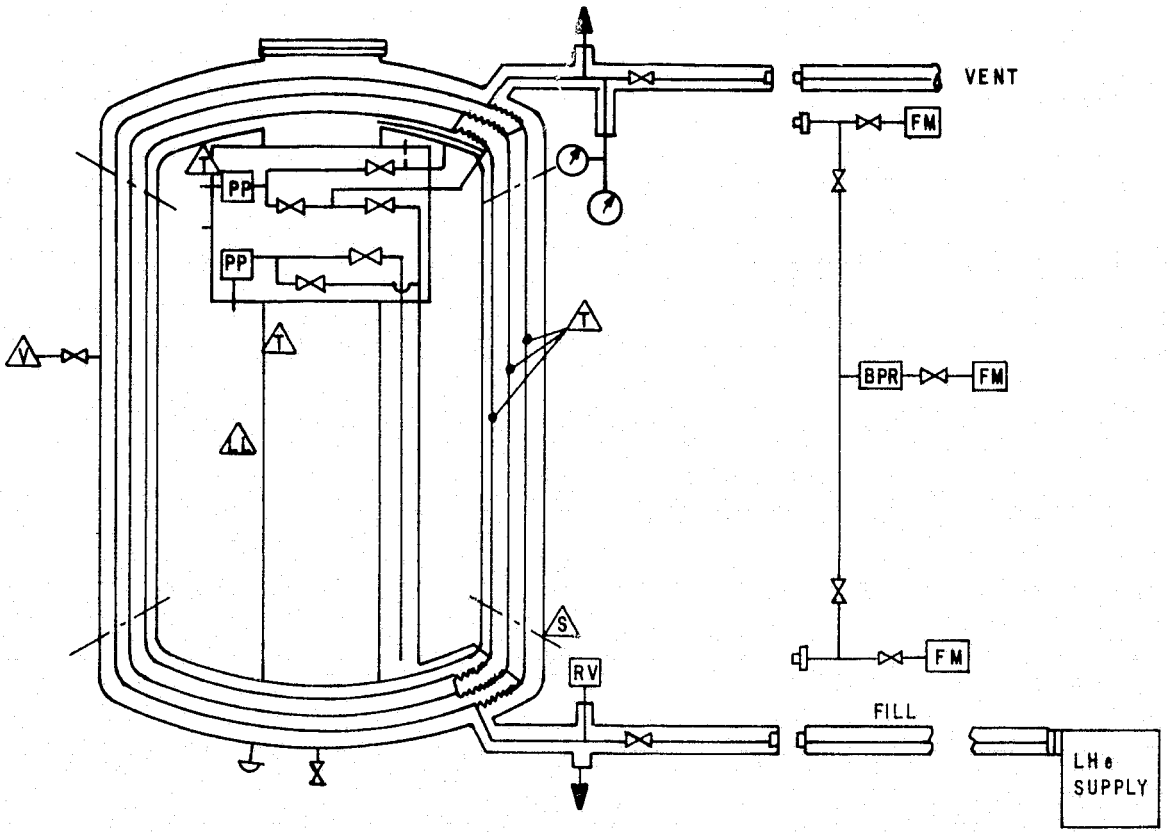

PP – POROUS PLUG
BPR – BACK PRESSURE REGULATOR
RV – RELIEF VALVE
FM – FLOW METER
V – VACUUM SENSOR
LL – LIQUID LEVEL SENSOR
T – TEMPERATURE

Figure 5-2 Liquid Helium Dewar Schematic

Table 5-1
Helium Dewar Physical Characteristics

Parameter	Value
Size	54 in. (137 cm) dia x 55 in. (140 cm) lg.
Weight (wet)	1020# (464 kg)
LHe Capacity (Superfluid)	650 Liters - 190# (86 kg)
Launch Environment	Thor/Delta
Instrument Cavity	18 in. (46 cm) dia x 40 in. (102 cm) lg.
Supports	6 fixed fiberglass, 6 retractable
Insulation	MLI
Fluid Containment	Porous Plug

An additional purpose of the dewar is to determine fluid management problems which may be encountered on the Stanford Relativity Experiment and find solutions for them.

5.2 INSULATION CONCEPT

In the last ten years a significant amount of investigation has been conducted to determine the most efficient method for insulating cryogenic dewars. Present day concepts vary from layups of one hundred and twenty layers of aluminized mylar per inch to ten layers per inch. The BBRC concept leans toward the latter layer density. The inner blanket is laid up at approximately ten layers per inch. The second blanket is approximately twenty layers per inch as is the third blanket. The fourth (outer) blanket is laid up at approximately thirty layers per inch.

The philosophy for going to the lower layer densities is based on in-house testing and on performance trends which have

been documented by other investigators. At BBRC a quarter-scale model of the pressure vessel was made and insulated utilizing the same basic concept employed in the full size dewar. The layer density was checked at twenty layers per inch and thirty-five layers per inch. The inner boundary of the test specimen was maintained at 77K and the outer boundary varied from 77 to 300K. The lower layer density was more efficient at all outer shell temperatures. The advantage toward the lower layer density was diminishing as the outer shell temperature increased.

The aluminized mylar that was used for this project was purchased from National Metallizing Division of Standard Packaging Corporation. The mylar was of quarter mil thickness and was sixty-two inches wide. The dacron net was type B2A purchased from Apex Mills.

The mylar appeared to have an emissivity of 0.035 - .040. No problems were encountered with the mylar as far as excessive wrinkles or holes. The net on the other hand did have blemishes in the form of wads of net at localized places and the width varied by up to five inches. Because of these blemishes these sections were removed and not used. Consequently additional net had to be purchased. The second batch was of a significantly better quality.

As the insulation is applied there are various items such as supports and plumbing which penetrate the insulation blanket. The generalized treatment of these penetrations is called buffering. As a tube, rod, or support penetrates a blanket, a certain amount of gap or clearance is left around the outside of the tube. This gap allows radiant energy to penetrate the blanket and reduces its thermal efficiency. An optimum design would be a blanket that perfectly fits the outside of

the item being insulated with holes located exactly on the center line of the penetration. Mylar layers which are very lightly loaded do not lay up this way. Therefore oversize clearance holes are used around penetrations, mylar and donut washers are then used to close the holes. The joints between the heads and cylinders are closed by flaps which are a part of the cylinder layers. Figure 5-3 and 5-4 illustrate the buffering concept.

Other means of reducing heat leak to the pressure vessel are to match temperatures of all insulation members where they contact each other or to minimize the energy exchange at those contact points. In some cases of support or plumbing penetrations, it is not possible to match temperatures. In these cases, the plumbing or support is wrapped with one or two layers of aluminized mylar to reduce the emissivity of the hotter element to reduce the energy exchange to the colder element. The fixed supports and plumbing penetrations were wrapped in this manner.

Completely surrounding the first three insulation blankets are three vapor cooled shields. These shields are aluminum and have three functions. The first is to utilize the refrigeration available in the effluent GHe to intercept part of the incoming heat. The second is to cool the fiber-glass supports. The third is to provide a rigid support for the multilayer insulation to reduce the conduction through the MLI.

5.3 TOOLING

Tooling is required for cutting the insulation to the proper sizes and maintaining control and continuity between layers.

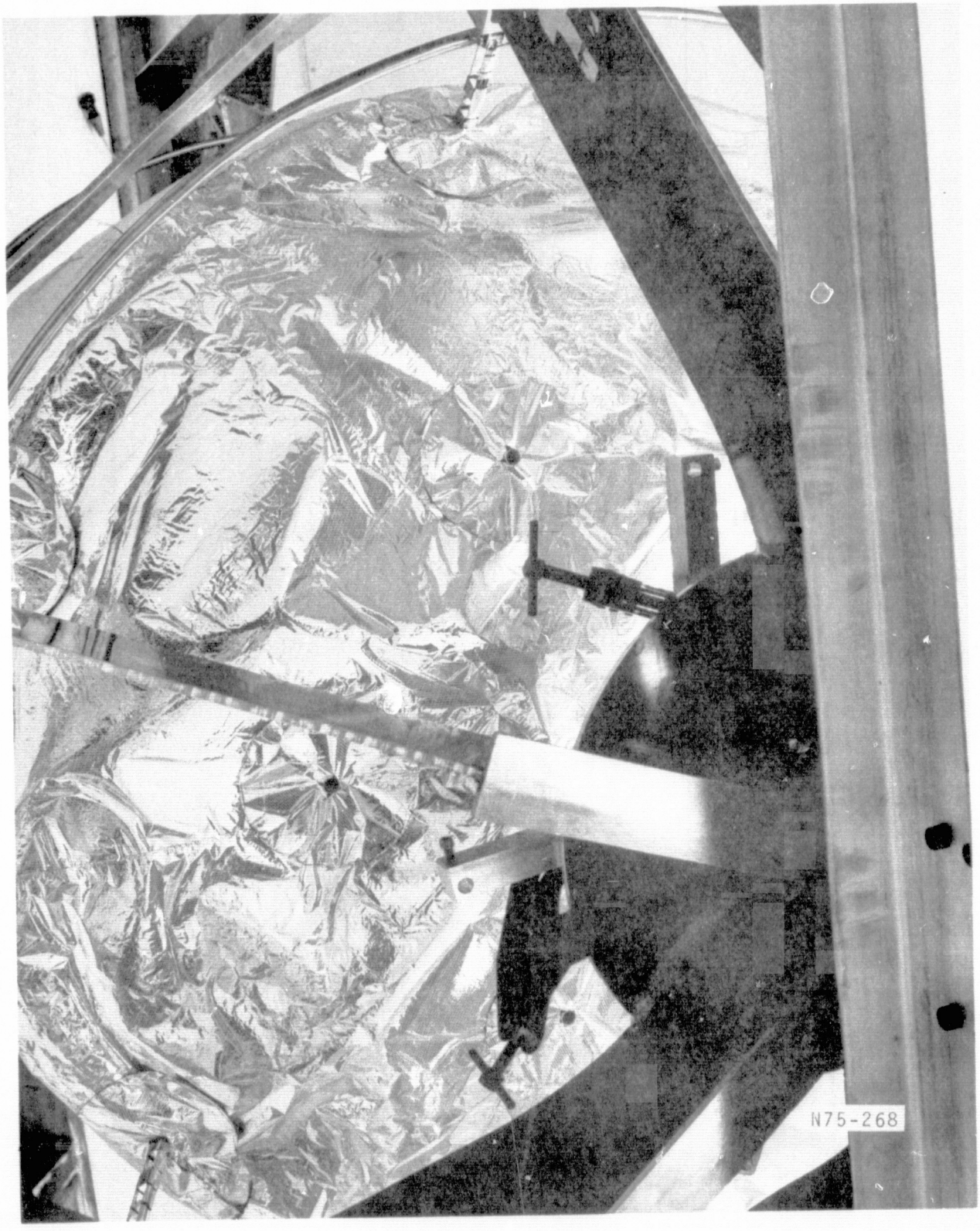

Figure 5-3 Dewar Buffering Concept

Figure 5-4 Dewar Buffering Concept

The tooling used in the layup of this insulation is described in the following paragraphs.

A fourteen foot by five foot cutting table was constructed to handle the long cylinder lengths (see Figure 5-5). The table has sixteenth inch graduations on each side and a clamping/cutting bar at one end. The net and mylar located on rollers at one end of the table was pulled out to the proper length and then cut off. The width was then trimmed to size by using a slide cutting bar along the one edge. The slide cutting bar fits on the edge of the table and has a variable extension bar which hangs over the table to the proper length.

The tooling for the insulation heads (see Figure 5-6) consists of a flat circular disk which has slits located every 60° and slide bars for locating the support penetrations. One of the heads has five holes in it in addition to the support clearance holes. These holes are for access to the control valves located in the pressure vessel. The insulation head was formed to a torispherical configuration by laying the flat pattern disks on a curved head, overlapping the slit seams, and then welding the seams. (See Figure 5-7).

An additional fixture is an installation fixture (shown in Figure 5-8) designed to position all supports for proper location in the outer shell. The fixture permits 360 degree rotation of the pressure vessel in two axes. The procedure used in applying the insulation was to install the total number of head layers required per blanket at one time, slide all except the layer being used up the support, install the cylindrical section of the layer and sew it to each head.

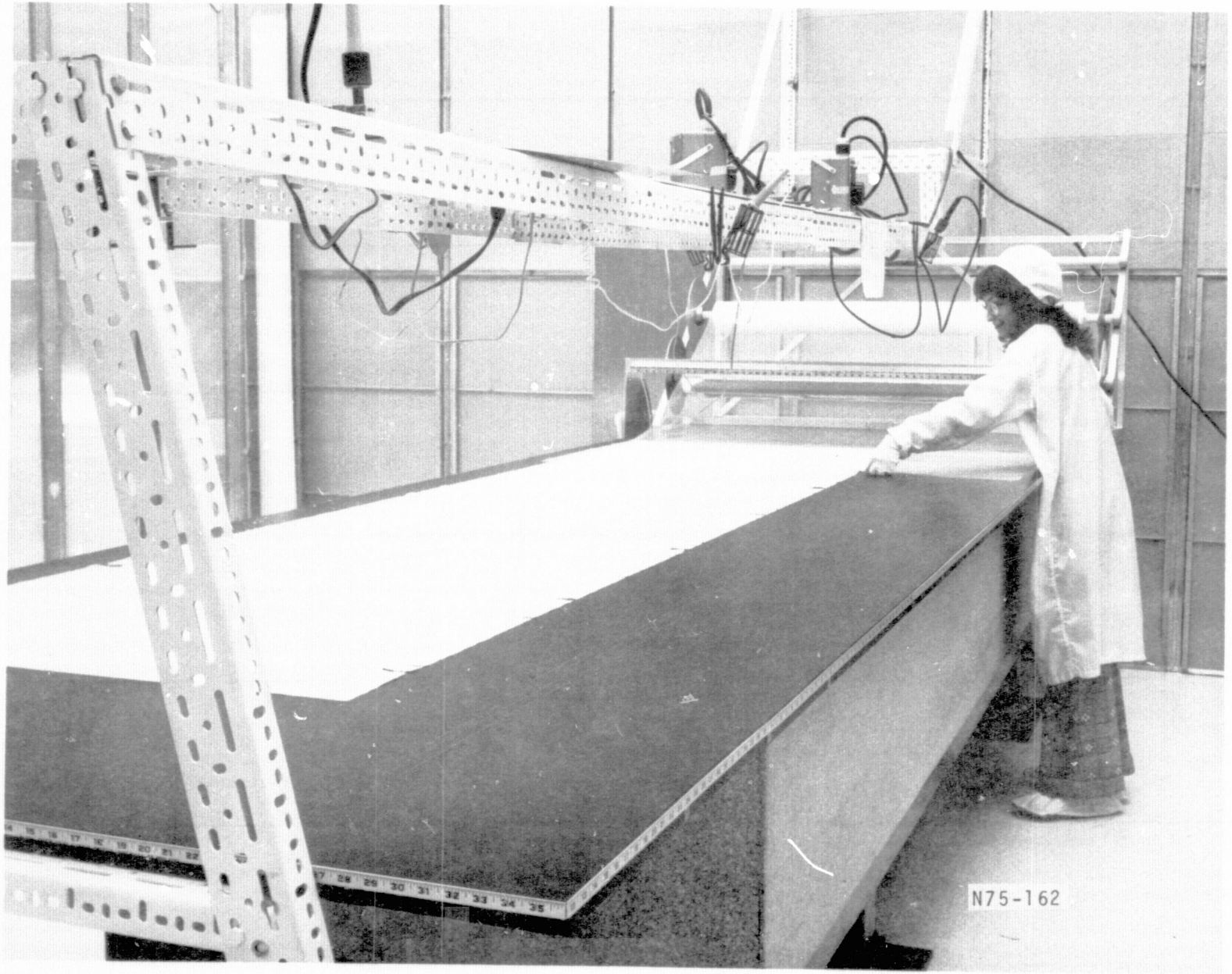

Figure 5-5 Cutting Table

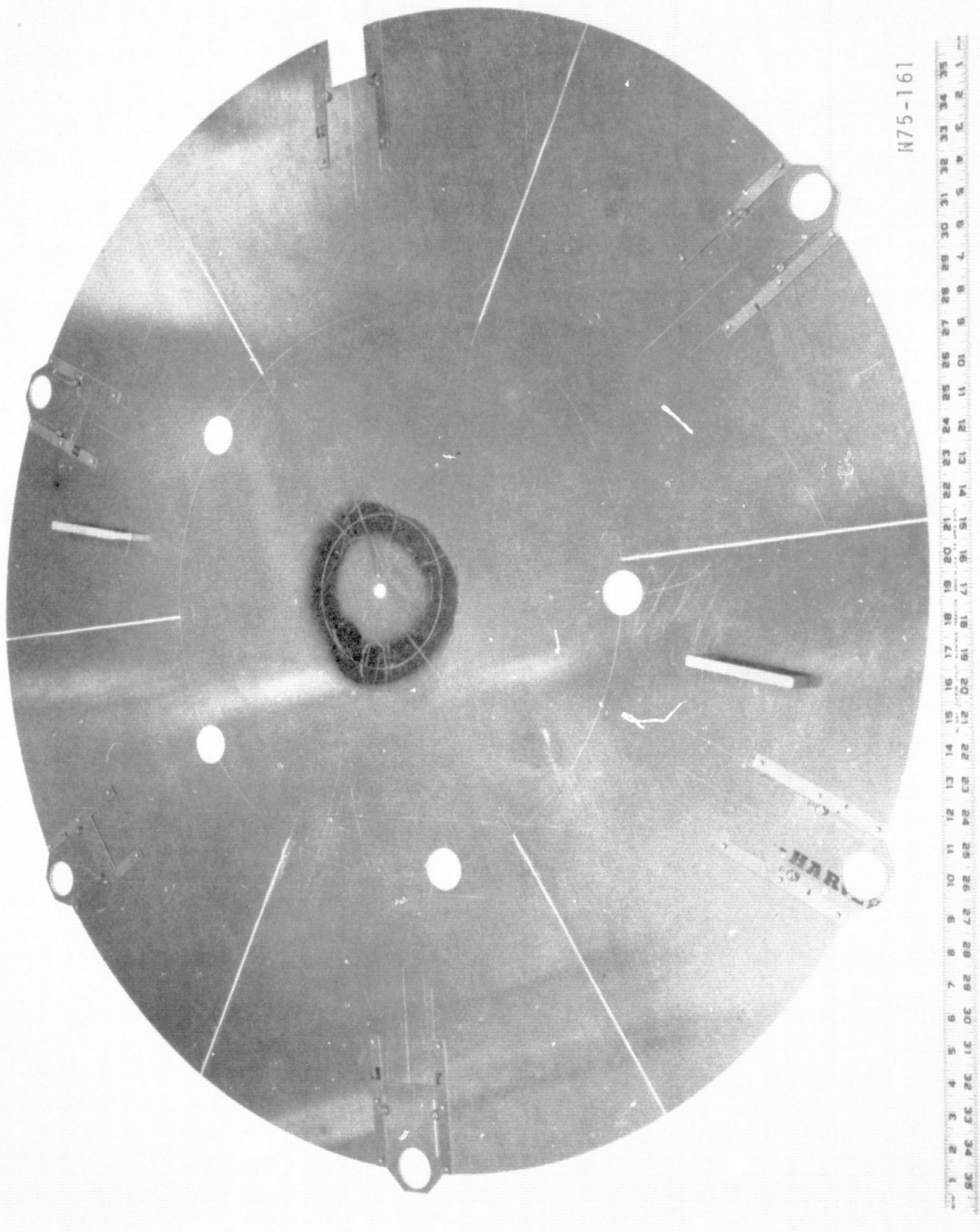

N75-161

Figure 5-6 Tooling for Insulation Heads

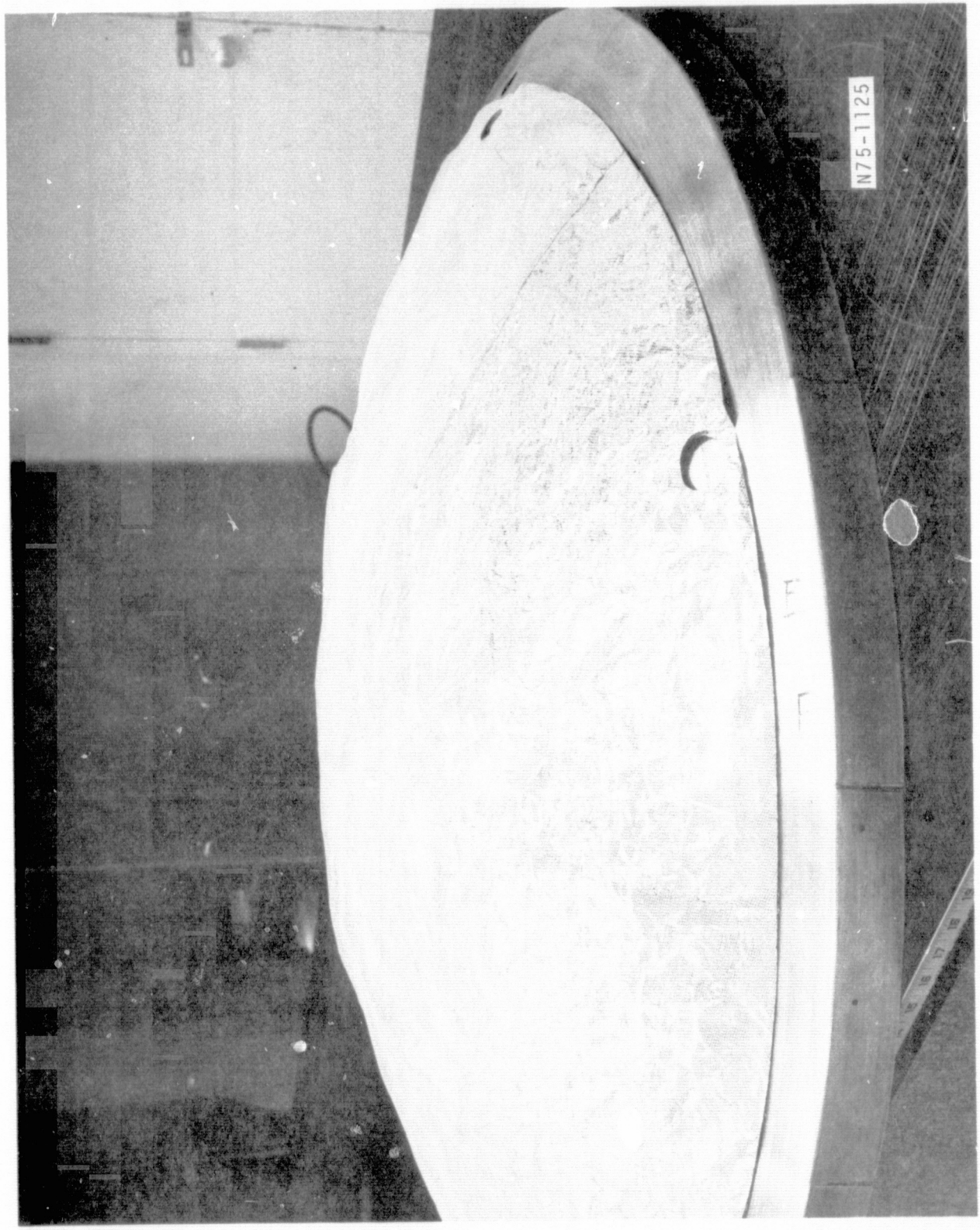

Figure 5-7 Insulation Head on Tool

Figure 5-8 Installation Fixture

5.4 INSULATION LAYUP DESCRIPTION

The following paragraphs describe the detail procedure used in insulating the pressure vessel.

5.4.1 Pressure Vessel Insulation Radiation

As the insulation cools, the long wavelength interception by the insulation is important. At 4°K there is a possibility that mylar may not be thick enough to reflect the long wavelength energy. Therefore, one layer of one and one-half mil thick aluminum foil was wrapped around the PV. The foil was encased in dacron net. Surrounding the layer of foil are five layers of mylar, aluminized on each side and spaced from each other by dacron net. All layers are sewn to each other at the heads and lateral seam on the cylinder. The cylinder joint is overlapped by three inches to minimize radiation from tunneling through the joint. The cylinder joints are staggered from layer to layer by approximately one foot. This is to minimize layer buildup and loading in that area. The stitching is approximately one stitch each half-inch, using polyester thread. The mylar insulation was oversized by 0.3 inch on the diameter to allow for the difference in thermal contraction between aluminum and mylar.

Buffering of the penetrations was provided on the second and fifth layers on all penetrations. Figure 5-9 shows disks used for buffering the supports. The cylinder widths were increased by two inches to provide a flap over the heads to completely interrupt any paths for radiation through the head to the cylinder joints. The flaps are cut to be one-inch-by-one-inch flaps.

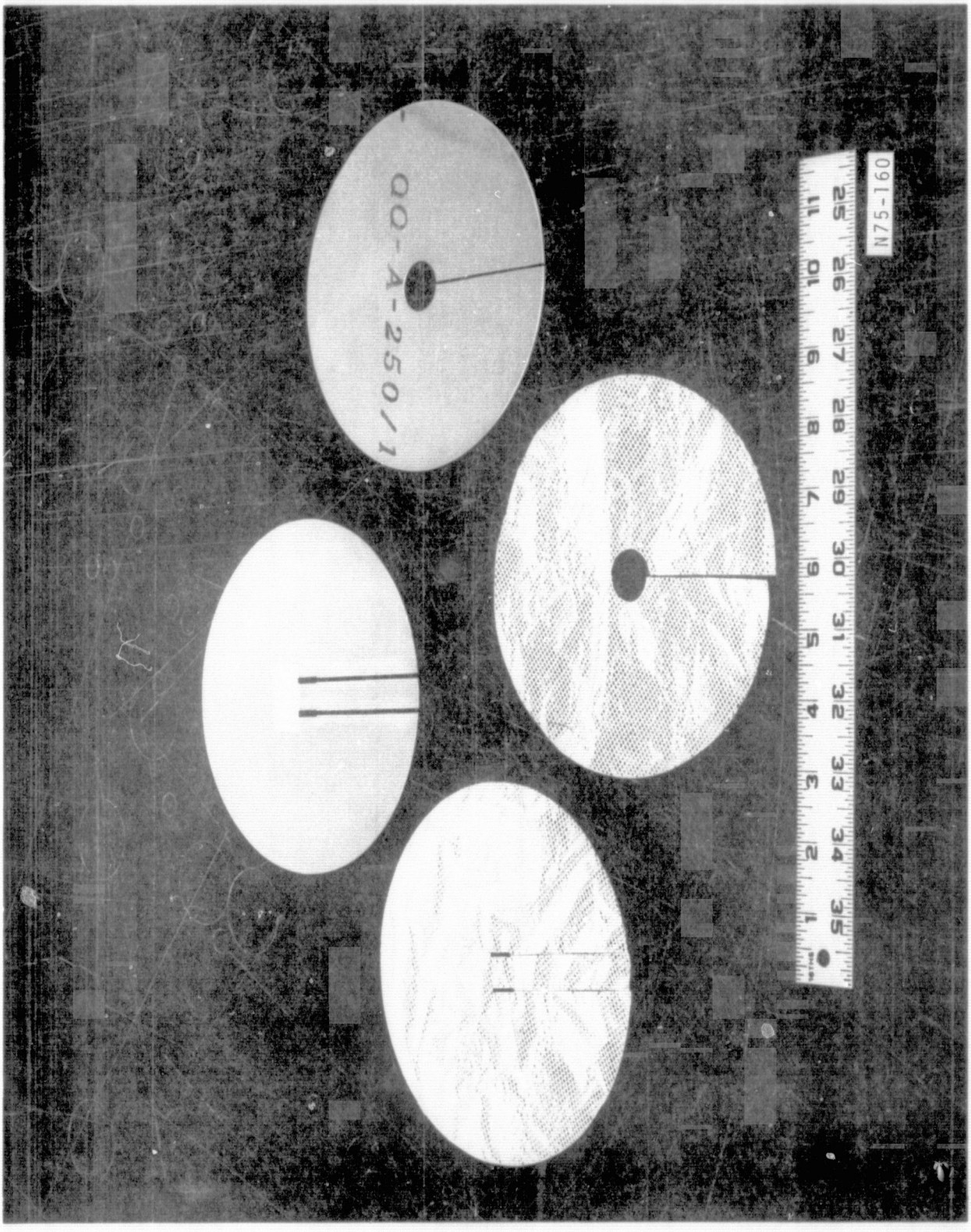

Figure 5-9 Support Buffering Disks

All plumbing extending from the PV to the vapor-cooled shield (VCS) was wrapped with aluminized mylar tape (3M type 855) to minimize energy exchange between the tube and the insulation.

The 0.500 inch by .0.016 thick 304 stainless steel tubing which forms the fill lines and vent lines is attached to the inner vapor cooled shield (IVCS) by metal clips which are riveted to the shield every eight inches. The tube is also bonded to the shield using PRD 1564 urethane which has been filled with aluminum powder (see Figure 5-10). The urethane increases the terminal contact area between the tube and the shield, thereby enhancing the heat transfer between the GHe effluent gas and the VCS.

The IVCS is supported from the fiberglass straps by tabs which are riveted to the shield and then bolted to aluminum blocks (see Figure 5-11). These blocks are bonded between the support straps. This provides support for the shields and in turn permits the support to be cooled. All vapor cooled shield heads are 1100 aluminum and span formed to form a "torispherical" head of 0.050-0.060 thickness. The IVCS heads are 44.00 inches in diameter. The cylinder is 1100 aluminum, 0.016 inches thick.

5.4.2 Inner Vapor Cooled Shield Blanket

The IVCS insulation blanket consists of sixteen layers of aluminized mylar spaced by dacron net. The blanket installation is the same as that used in the first blanket, i.e., the same method of buffering is used every three layers, the inner layer is spaced 0.3 inch larger than the IVCS and installation of the layers was the same.

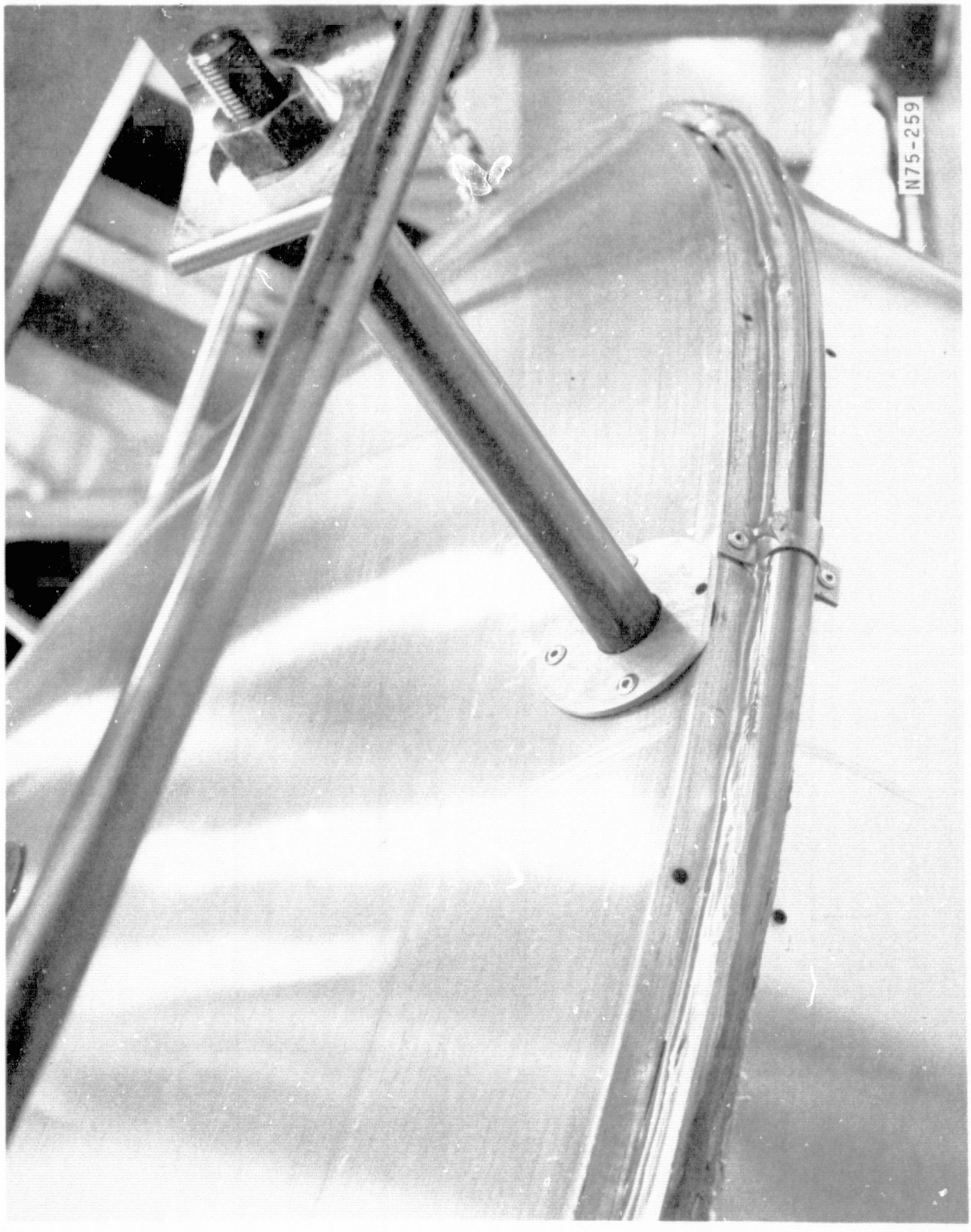

Figure 5-10 Tubing Attached to Shield by Riveted Clips and Aluminum Filled PRD 1564 Urethane

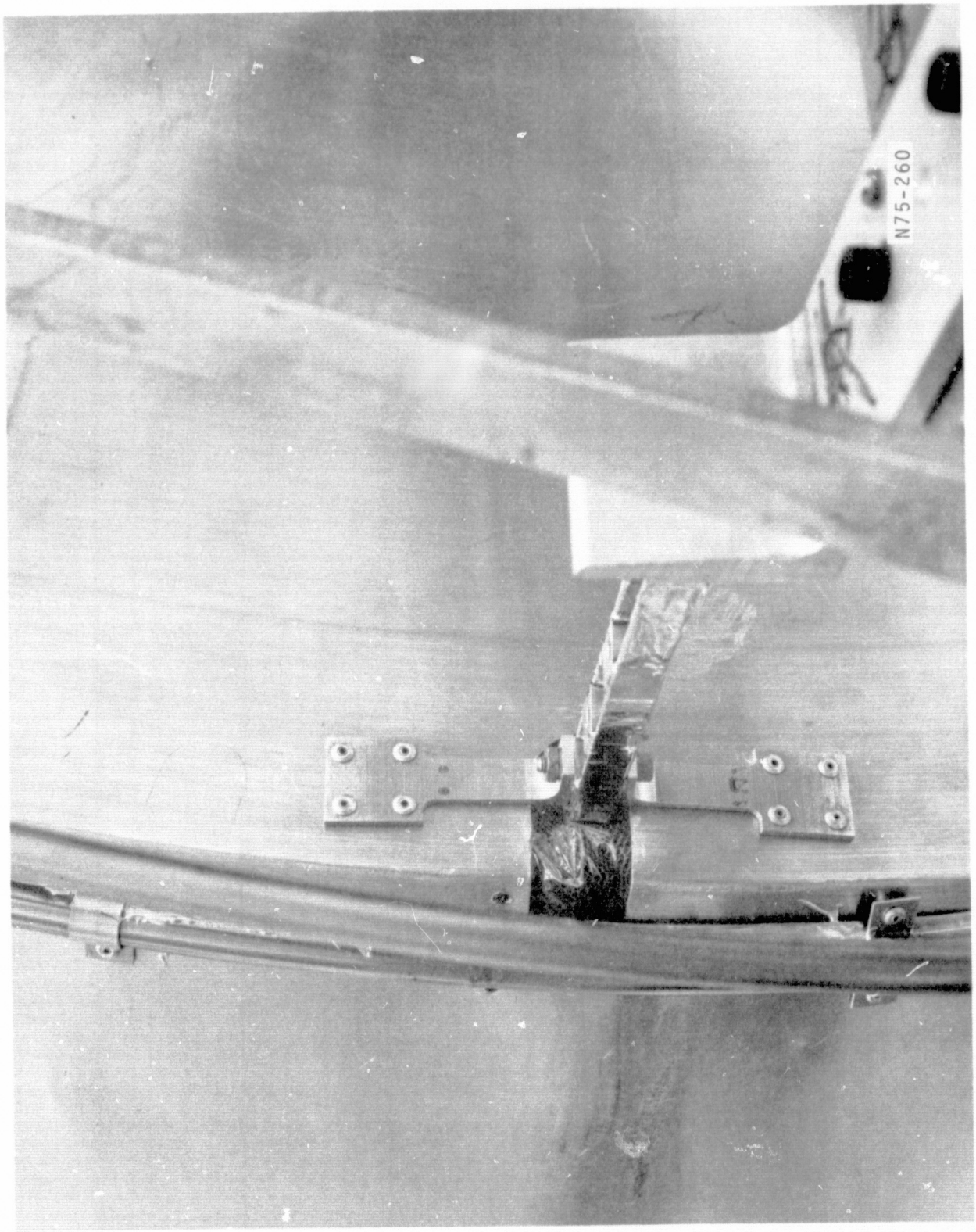

Figure 5-11 Fiberglass Support Straps.

To provide clearances for the valve driver extension rods, to connect to the valves in the PV, thin walled fiberglass tubes were bonded to the top head of IVCS. (See Figure 5-12). The insulation is buffered to these tubes to minimize radiation on the outside of the tube. The outside of the tube was wrapped with aluminized mylar tape. The tubes were sized such that there is no direct conduction between each vapor cooled shield.

During the cutting of the insulation for the IVCS a large amount of static electricity was generated on the mylar and made the cutting difficult. A ground wire was routed along the top of the cutting table and christmas tree garland was attached to it. By brushing the mylar and net with the garland the static charge could be drained off. When work was not in progress the garland was left draped across the rolls of net and mylar to drain the static charge.

Figure 5-13 shows the 16th layer of the IVCS insulation blanket.

The middle vapor cooled shield (MVCS) which encloses the IVCS blanket is pictured in Figure 5-14. It is of the same construction as the IVCS except the diameter of the shield is 46.94 inches.

5.4.3 Middle Vapor Cooled Shield Insulation Blanket

The middle vapor cooled shield insulation blanket consists of 20 layers of aluminized mylar spaced by dacron net. Buffering is every third layer and treatment of seams, and layer attachment is as previously described. Fiberglass tubes are again used to act as guide for the valve extensions.

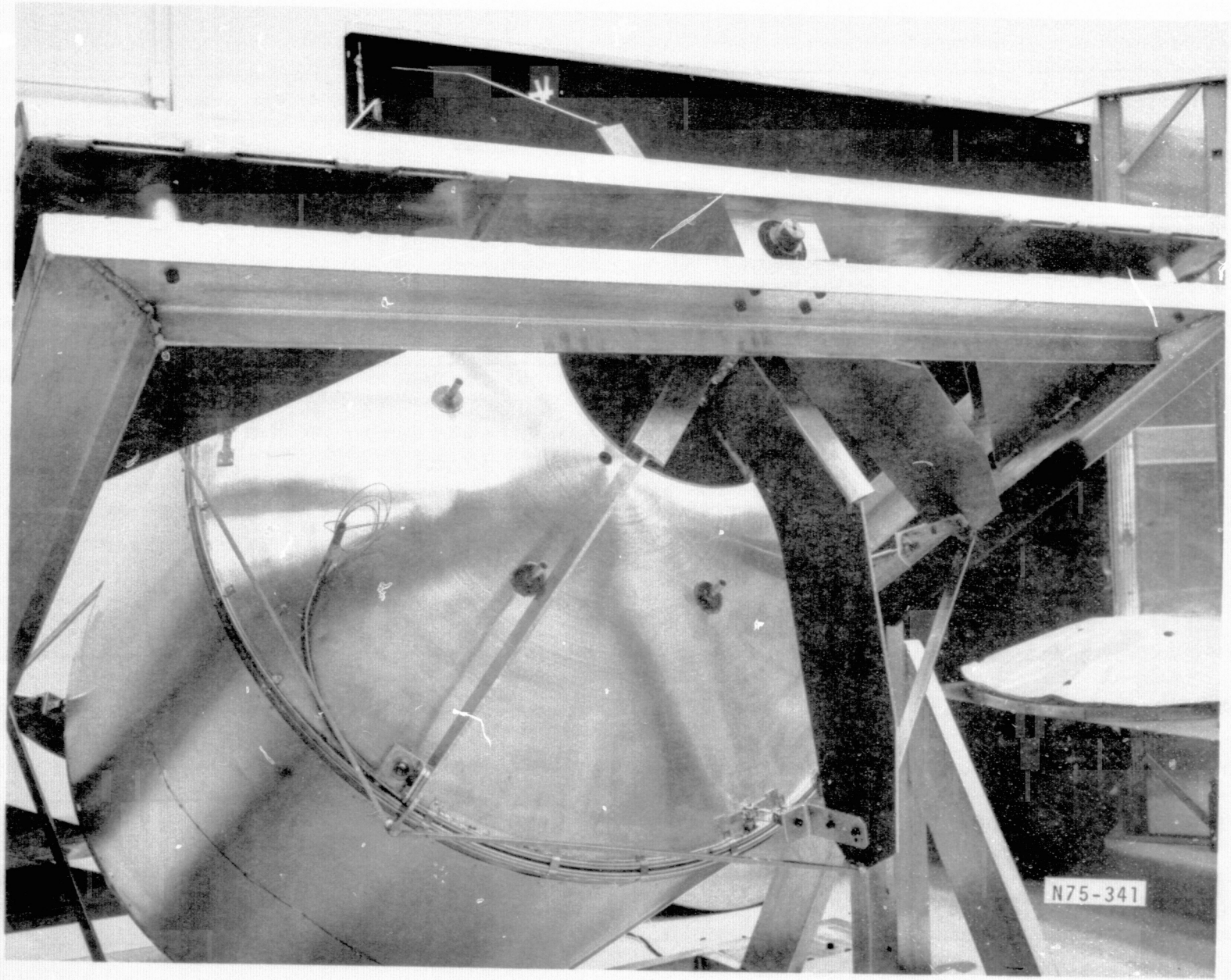

Figure 5-12 Thin-Walled Fiberglass Tubes Bonded to Top Head of IVCS to Provide Clearance

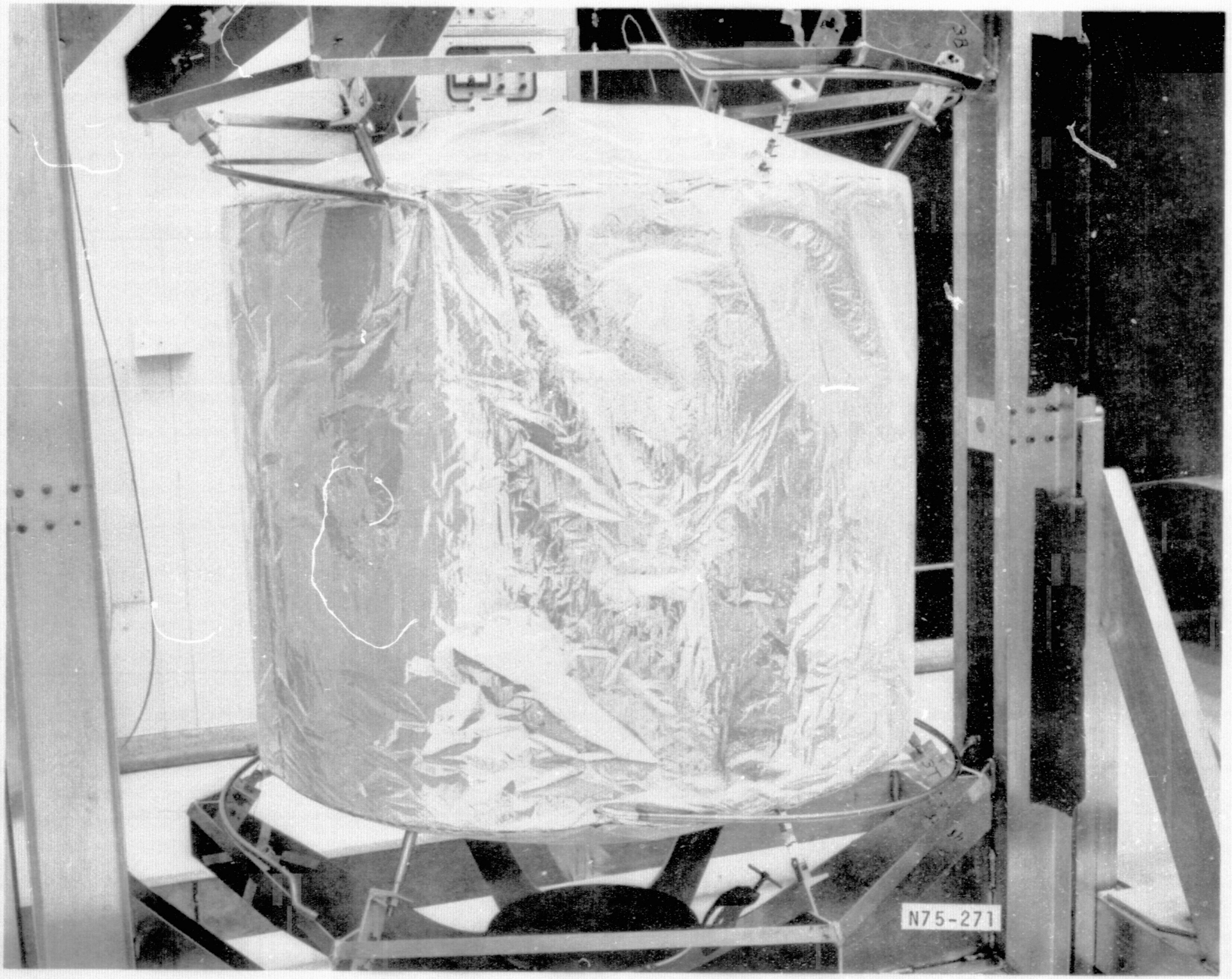

Figure 5-13 16th Layer of IVCS Insulation Blanket

Figure 5-14 Middle Vapor Cooled Shield

The treatment of the 20th layer of the upper head is shown in Figure 5-15. Surrounding the blanket is the outer vapor cooled shield (OVCS) as pictured in Figure 5-16. The OVCS is constructed and supported as the two previous shields and is 49.38 inches in diameter.

5.4.4 Outer Vapor-Cooled Shield Insulation Blanket

The outer insulation blanket consists of 34 layers of aluminized mylar spaced by dacron net. It is buffered every third layer and the layup procedure is as stated previously. The 34th layer is pictured in Figure 5-17.

After completion of the insulation layup the pressure vessel and insulation was installed in the outer shell and prepared for vacuum acquisition.

5.5 INSTRUMENTATION

The following instrumentation was installed for evaluation of the dewar thermal performance and specifically the contribution of the insulation to the dewar heat leak:

- Four chromel/constantan thermocouples (T/C) located on the IVCS. One located one inch from the first contact of the vent line to the shield and one, one inch from the fill line first contact. Another T/C was located 180° from the first two in the center of the shield cylinder. The fourth T/C was located on the shield support block which was bonded to the fiberglass support. Two germanium temperature sensors were located next to the fill and vent line attachment also. Four thermocouples were

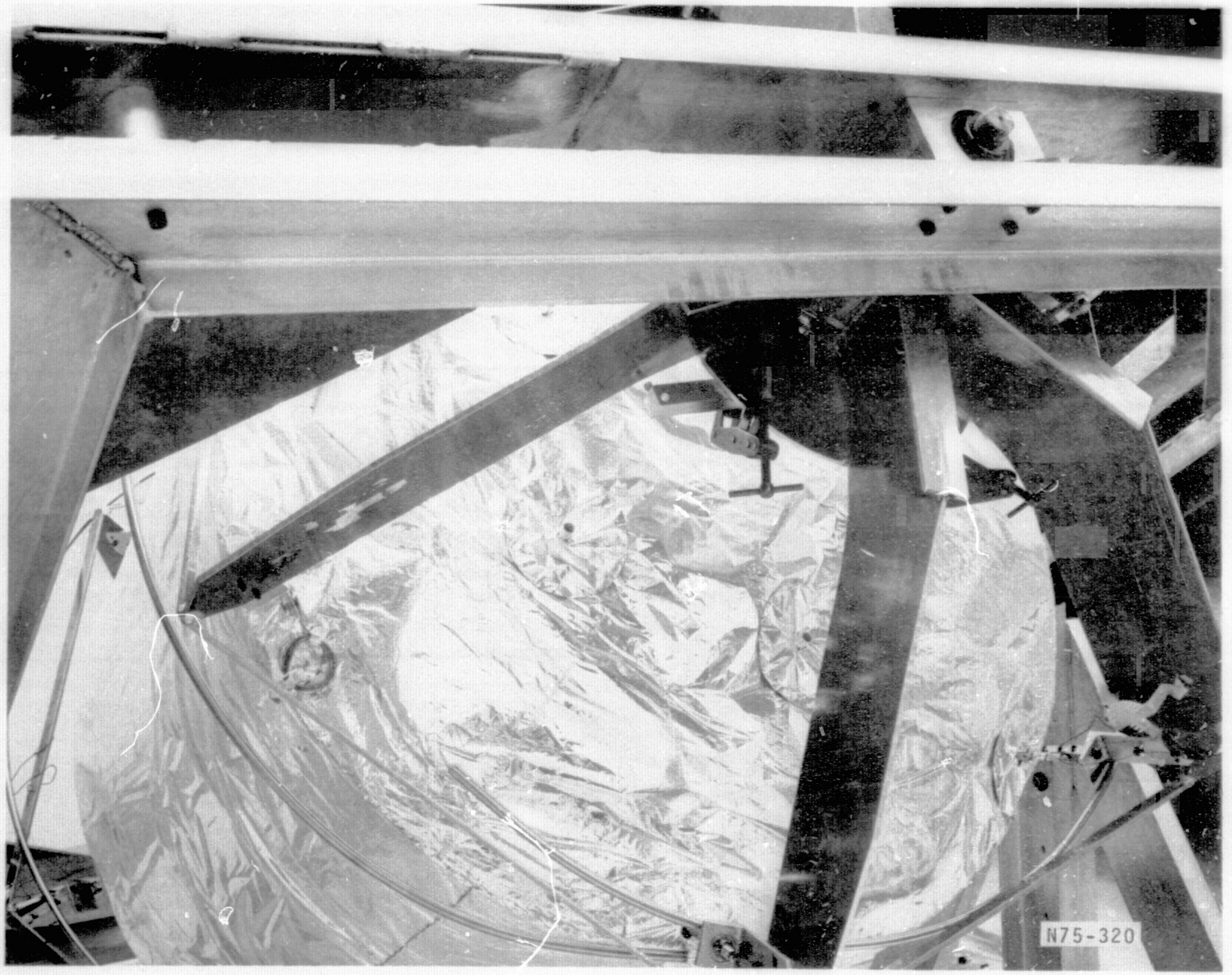

Figure 5-15 20th Layer of Upper Head

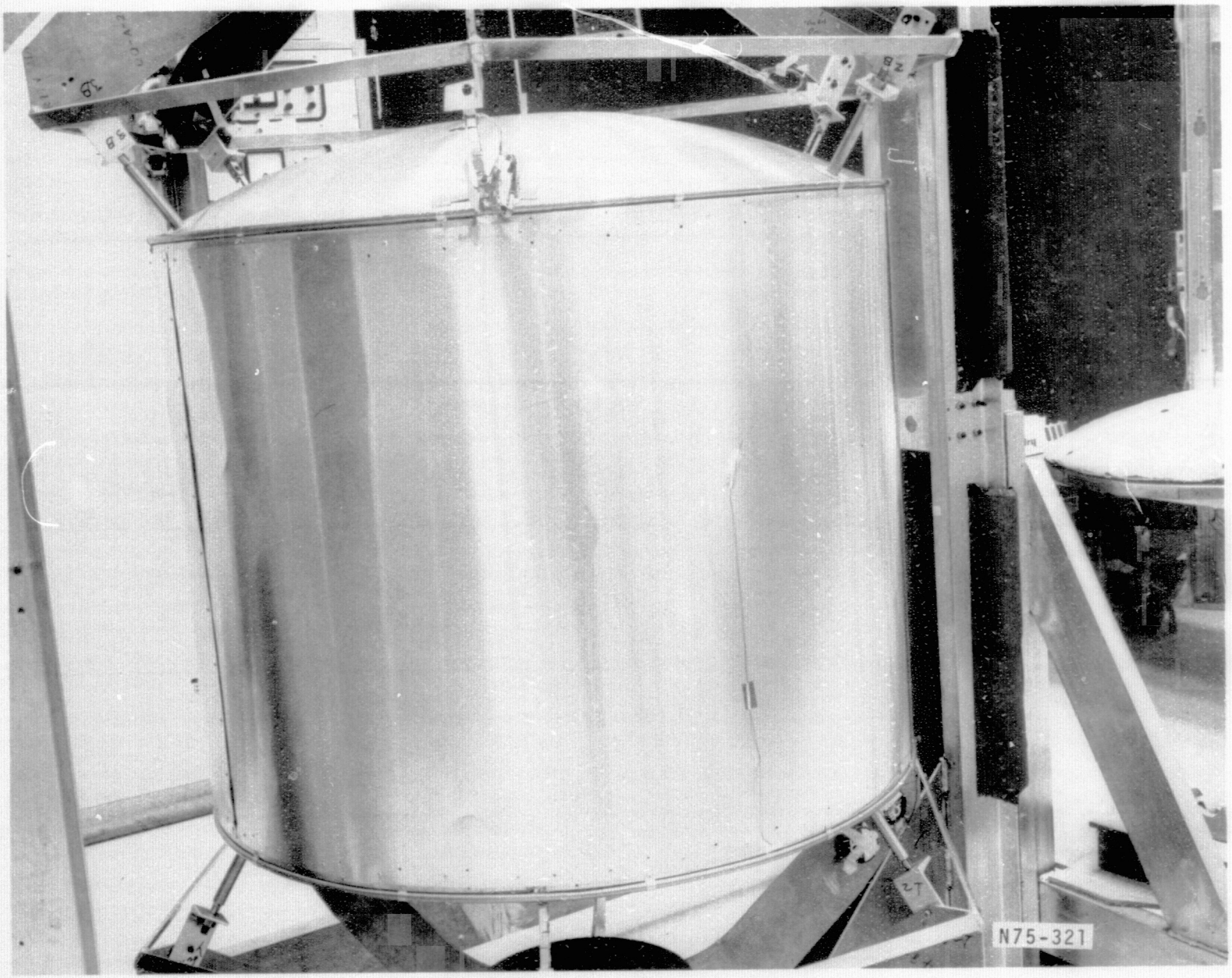

Figure 5-16 Outer Vapor Cooled Shield

Figure 5-17 34th Layer of Outer Insulation Blanket

located in the MVCS and OVCS in the same relative locations as the IVCS. The purpose of these sensors is to determine the thermal conductivity of each blanket as well as determining the efficiency of cooling the support straps. Samples of the installation of the sensors are as shown in Figure 5-18.

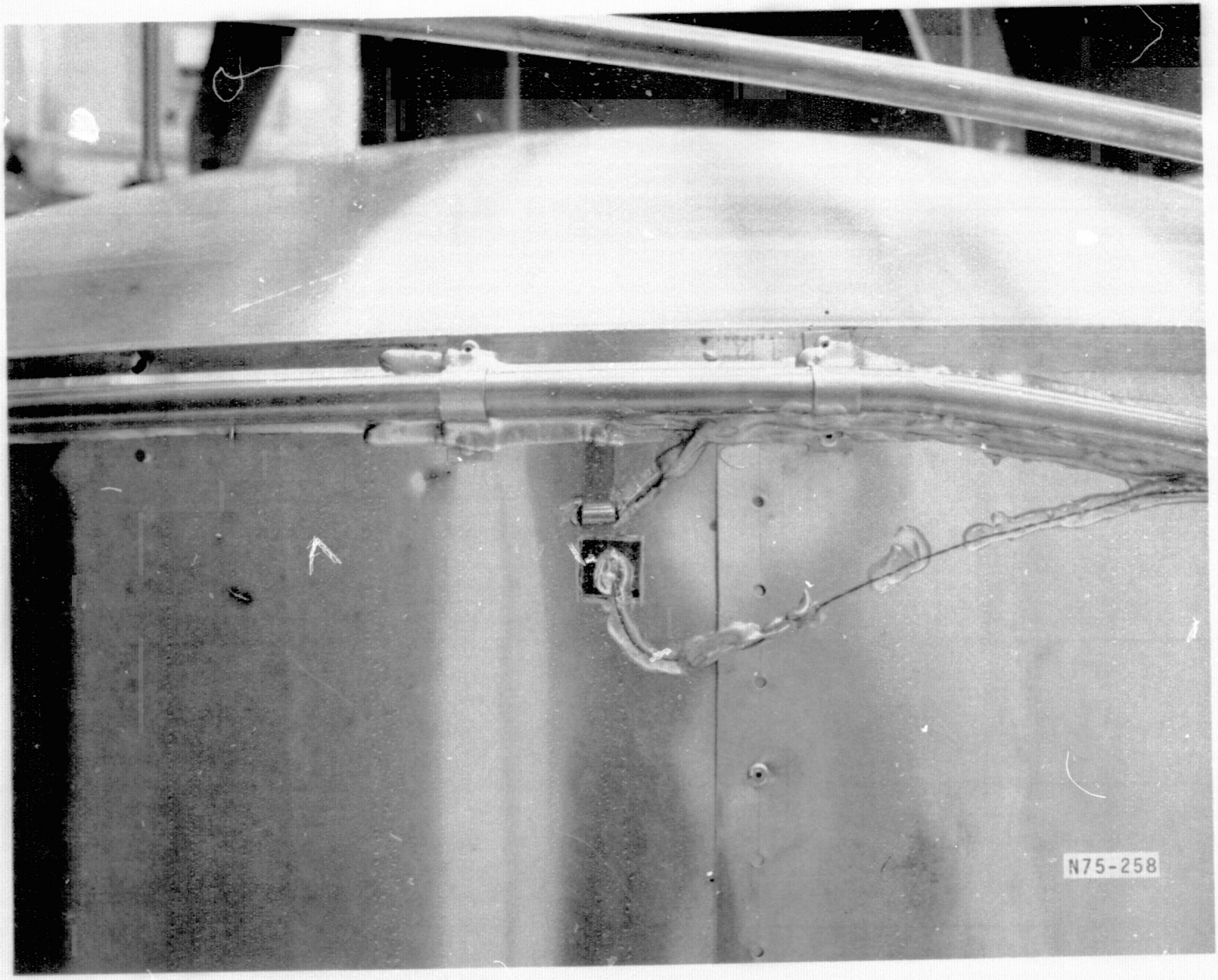

Figure 5-18 Sensor Insulation

APPENDIX A

STRUCTURAL ENVIRONMENT

(From Scout Users Manual, September 1972)

Thrust axis sine (2 oct/min sweep)

10-18 Hz	1.0 g peak
18-44 Hz	0.06 in. D.A.
44-65 Hz	6.0 g peak
65-2000 Hz	4.5 g peak

Lateral axis sine (2 oct/min sweep)

10-20 Hz	0.75 g peak
20-28 Hz	0.038 in. D.A.
28-2000 Hz	1.5 g peak

All axes random

20-325 Hz	0.0031 g^2/Hz
325-1300 Hz	+6 db/oct
1300-2000 Hz	0.0495 g^2/Hz

Axial acceleration

9 g

Lateral acceleration

3 g

APPENDIX B

RESONANT FREQUENCIES OF A TWO DEGREE OF FREEDOM SYSTEM

Resonant frequencies of a two degree of freedom system.

$$M\ddot{x} + Kx = 0$$

$$\ddot{x} = -w^2 x$$

$$[-w^2 M + K]\, x = 0$$

$$G = K^{-1}$$

$$\lambda = \frac{1}{w^2}$$

$$[GM - \lambda I] = 0$$

Expanding the matrix equation:

$$\begin{bmatrix} \delta_{yy} & \delta_{y\theta} \\ \delta_{\theta y} & \delta_{\theta\theta} \end{bmatrix} \begin{bmatrix} M & O \\ O & J \end{bmatrix} - \lambda \begin{bmatrix} 1 & 0 \\ 0 & 1 \end{bmatrix} = 0$$

$$\begin{bmatrix} M\delta_{yy} - \lambda & J\delta_{y\theta} \\ M\delta_{\theta y} & J\delta_{\theta\theta} - \lambda \end{bmatrix} = 0$$

$$\lambda^2 - (M\delta_{xx} + J\delta_{\theta\theta})\lambda + MJ(\delta_{xx}\delta_{\theta\theta} \quad \delta_{y\theta}\delta_{\theta y}) = 0$$

APPENDIX C

MASS AND STIFFNESS PROPERTIES

Mass and Stiffness Properties - Weight and Weight Moment of Inertia

ITEM	WEIGHT	MASS MOMENT OF INERTIA	
		PITCH	ROLL
Pressure Vessel	15.4 (34)	1.115 (9.86)	.996 (8.81)
Telescope	3.5 (7.6)	.133 (1.18)	.005 (.046)
Gyros	11.4 (25)	.045 (0.40)	.039 (.34)
Total Dry Vessel	30.3 (66.6)	1.293 (11.4)	1.040 (9.2)
Fluid	16.8 (37)	.576 (5.1)	.644 (5.7)
Total Wet Vessel	47.1 (104)	1.869 (16.5)	1.684 (14.9)

Units: Weight - kg (lb); Inertia - kg - m^2 (lb-in^2)

Stiffness Properties

Outer Annular Plate

Outer Radius =	15.2 cm	(6.0 in)
Inner Radius =	9.5 cm	(3.75 in)
Thickness =	.25 cm	(0.10 in)
Modulus (E) =	7×10^{10} N/m^2	(10×10^6 psi)

Fiberglass Cylinder

Radius =	9.5 cm	(3.75 in)
Thickness =	0.076 cm	(0.03 in)
Length =	30.5 cm	(12.0 in)
Modulus (E) =	2×10^{10} N/m^2	(2.8×10^6 psi)

Inner Annular Plate

Outer Radius =	11.9 cm	(4.7 in)
Inner Radius =	9.5 cm	(3.75 in)
Thickness =	0.127 cm	(0.05 in)
Modulus (E) =	11×10^{10} N/m^2	(16×10^6 psi)

Titanium Cylinder

Radius =	11.4 cm	(4.5 in)
Thickness =	0.076 cm	(0.03 in)
Length =	10.2 cm	(4.0 in)
Modulus (E) =	11×10^{10} N/m^2	(16×10^6 psi)

Tension Supports (Per Support)

Area =	0.284 cm^2	(0.044 in^2)
Length =	25.4 cm	(10.0 in)
Modulus (E) =	4×10^{10} N/m^2	(6×10^6 psi)

APPENDIX D

ABSOLUTE TEMPERATURE MONITOR ANALYSIS

Figure 1 shows the listing of the program used to determine the values of R_1, R_2, R_3 and R_f for the proper gain and linearity. The program also calculates the output versus temperature. Figure 2 gives this for the amplifier sized to go from 1.5 to 2.17°K. Performance over the range of 1.5 to 4.2°K will give nearly as good linearity. The gain shown is that measured with respect to the voltage that would appear across R(t) if the amplifier were not connected.

The linearity is seen by the consistency of "DELTA VO" through the temperature range.

```
PAGE    1     BBRC

// JOB    1000 1001 1002 1004       1000 1004       BBRC
  0000        1000          1000        0000
  0001        1001          1001        0001
  0002        1002          1002        0002
  0003        1004          1004        0003

V2 M11   ACTUAL 16K  CONFIG 16K

// FOR

C-ERRS...STNO.C.....  F O R T R A N   S O U R C E   S T A T E M E N T S  ........  IDENTFCN    **COMPILER MESSAGES**

                INTEGER L,H,AA
                DIMENSION RTH(68), U(350), G(350), X(350), A(350), EO(350),
               * C(350), G(350)
                READ(2,2) RTH
          2     FORMAT( 8F10.2)
                L = 1
                H = 68
                DO 9 I = L,H
                X(I) = 1.500 + FLOAT(I - 1) / 100.
          9     CONTINUE
                R1 = 1.0 E6
                VOFF = -.00071
                AA = (H - L)/2
                V = 5.
                VCC  = 10.
                BMIN = 10.
                DO 79 K = 1,4000,20
                EO(L-1) = 0.
                S = 0.
                R2 = FLOAT (K - 1)* 10
                VBL = VCC*RTH(L)/(R1 + RTH(L))
                VBH = VCC*RTH(H)/(R1 + RTH(H) )
                RIL = R2 + R1*RTH(L)/(R1 + RTH(L) )
                RIH = R2 + R1*RTH(H)/( R1 + RTH(H) )
                A1 = (VBL - VBH)/(RIL*RIH)
                B = (VBL - V)/RIL - VBH/RIH
                C1 = -V
                RF = (-B + SQRT(B**2 - 4.0*A1*C1) )/ (2.0 * A1)
                DO 69 I = L,H
                VB1 = VCC*RTH(I)/(R1 + RTH(I) )
                A(I)  = RF*(R1 + RTH(I)) / (R2*(R1 + RTH(I)) + R1*RTH(I))
                VB3 = VBL * RF/(RF + RIL)
                EO(I) = VB3*( A(I) + 1.0) - VB1 * A(I)
                G(I) = EO(I) - EO(I-1)
                P =  (G(I) + V/(FLOAT (H-L)))**2
         69     S = S + P
                B =  S ** .5
                IF (B- BMIN) 20,68,68
         20     BMIN = B
                DO 25  J = L,H
                U(J) = A(J)
                G(J) = EO(J)
                C(J) = G(J)
                D = P
                Y =  R2
         25     Z =  RF
         68     CONTINUE
```

```
C-ERRS...STNO.C..... F O R T R A N  S O U R C E  S T A T E M E N T S ........ IDENTFCN    **COMPILER MESSAGES**

          79    CONTINUE
                WRITE (5,59) Y,7
          59    FORMAT( 1H1,  15X,4HR2 =,1F10.0,2X,3HOHM, 5X,4HRF =,1F10.0,2X,
               1 3HOHM)
                R9 = R1*RTH(AA) / (R1 + RTH(AA)) + Y
                R15 = RTH(L) * (R2 + RF) / ( RTH(L) + R2 + RF )
                VP = VCC * R15 / ( R15 + R1 )
                V6 = VP * RF / ( RF + R2 )
                R3 = R9 * VCC / V6
                R4 = R9 * VCC / (VCC - V6 )
                WRITE(5,47) R3,R4
          47    FORMAT (//15X,4HR3 =,1F10.0,2X,3HOHM,5X,4HR4 =,1F10.0,2X,3HOHM)
                WRITE (5,29)
          29    FORMAT (///'           VOLTAGE OUT          DELTA VO
               *R(T)          AMPLIFIER GAIN   TEMPERATURE'/)
                WRITE (5,65)(Q(J),C(J),RTH(J), U(J), X(J), J = L,H )
          65    FORMAT( 5F20.3 )
                CALL EXIT
                END
VARIABLE ALLOCATIONS
   RTH(R )=0986-0200     U(R )=0542-0288     Q(R )=07FE-0544     X(R )=0ABA-0800     A(R )=0076-0ABC     EO(R )=1032-0D78
     C(R )=12EE-1034     G(R )=15AA-12F0    R1(R )=15AC        VOFF(R )=15AE         V(R )=15B0         VCC(R )=15B2
  AMIN(R )=15B4          S(R )=15B6         R2(R )=15B8         VAL(R )=15BA        VBH(R )=15BC        RIL(R )=15BE
   RIH(R )=15C0         A1(R )=15C2          B(R )=15C4          C1(R )=15C6         RF(R )=15C8        VB1(R )=15CA
   VR3(R )=15CC          P(R )=15CE          D(R )=15D0          Y(R )=15D2          Z(R )=15D4         R9(R )=15D6
   R15(R )=15D8         V8(R )=15DA         V6(R )=15DC         R3(R )=15DE         R4(R )=15E0          L(I )=15EC
     H(I )=15ED        AA(I )=15EE          I(I )=15EF          K(I )=15F0          J(I )=15F1

STATEMENT ALLOCATIONS
     2=1613     59=1616     47=1628     29=1640     65=1677      9=1689     69=180B     20=1828     25=1840     68=185A
    79=185A

FEATURES SUPPORTED
 ONE WORD INTEGERS
 STANDARD PRECISION
 ORIGIN
 IOCS-
   1403 PRINTER
   CARD

CALLED SUBPROGRAMS
 FSQRT   FAXB    FADD    FADDX   FSUB    FSUBX   FMPY    FMPYX   FDIV    FLD     FLDX    FSTO    FSTOX   FSBR    FDVR
 FAXI    FLOAT   CARD7   SRED    SWRT    SCOMP   SFIO    SIOAF   SIOFX   SIOF    SUBSC   PRNZ    SNR

REAL CONSTANTS
  .150000E 01=15F6    .100000E 03=15F8    .100000E 07=15FA    .710000E-03=15FC    .500000E 01=15FE    .100000E 02=1600
  .000000E 00=1602    .400000E 01=1604    .200000E 01=1606    .100000E 01=1608    .500000E 00=160A

INTEGER CONSTANTS
     2=160C      1=160D     68=160E   4000=160F     20=1610     10=1611      5=1612

CORE REQUIREMENTS FOR -
 COMMON-     0,   VARIABLES AND TEMPORARIES-  5110,   CONSTANTS AND PROGRAM-   768

END OF SUCCESSFUL COMPILATION
```

R2 = 1200. OHM RF = 476876. OHM

R3 = 765355. OHM R4 = 6424. OHM

VOLTAGE OUT	DELTA VO	R(T)	AMPLIFIER GAIN	TEMPERATURE
-0.000	-0.000	8487.611	49.591	1.500
0.074	0.074	8335.281	50.375	1.510
0.148	0.074	8187.640	51.160	1.520
0.222	0.074	8044.470	51.945	1.530
0.296	0.074	7905.570	52.731	1.540
0.370	0.074	7770.750	53.516	1.550
0.445	0.074	7639.820	54.302	1.560
0.519	0.074	7512.610	55.088	1.570
0.593	0.074	7388.960	55.874	1.580
0.668	0.074	7268.730	56.661	1.590
0.742	0.074	7151.770	57.448	1.600
0.816	0.074	7037.950	58.235	1.610
0.891	0.074	6927.140	59.023	1.620
0.965	0.074	6819.220	59.811	1.630
1.040	0.074	6714.080	60.599	1.640
1.114	0.074	6611.610	61.388	1.650
1.189	0.074	6511.720	62.177	1.660
1.264	0.074	6414.300	62.967	1.670
1.338	0.074	6319.260	63.757	1.680
1.413	0.074	6226.530	64.547	1.690
1.488	0.074	6136.010	65.338	1.700
1.562	0.074	6047.630	66.129	1.710
1.637	0.074	5961.320	66.920	1.720
1.712	0.074	5877.010	67.712	1.730
1.787	0.074	5794.620	68.504	1.740
1.862	0.074	5714.100	69.297	1.750
1.937	0.074	5635.380	70.089	1.760
2.012	0.074	5558.410	70.882	1.770
2.086	0.074	5483.130	71.676	1.780
2.161	0.074	5409.480	72.469	1.790
2.236	0.075	5337.420	73.263	1.800
2.311	0.075	5266.900	74.057	1.810
2.387	0.075	5197.870	74.851	1.820
2.462	0.075	5130.290	75.645	1.830
2.537	0.075	5064.110	76.439	1.840
2.612	0.075	4999.290	77.234	1.850
2.687	0.075	4935.800	78.028	1.860
2.762	0.075	4873.590	78.823	1.870
2.837	0.075	4812.630	79.617	1.880
2.912	0.075	4752.880	80.412	1.890
2.987	0.075	4694.320	81.206	1.900
3.062	0.075	4636.900	82.001	1.910
3.137	0.075	4580.610	82.795	1.920
3.212	0.075	4525.400	83.589	1.930
3.287	0.075	4471.240	84.383	1.940
3.362	0.074	4418.120	85.176	1.950
3.437	0.074	4366.000	85.969	1.960
3.512	0.074	4314.860	86.762	1.970
3.587	0.074	4264.680	87.555	1.980
3.662	0.074	4215.420	88.347	1.990
3.737	0.074	4167.070	89.139	2.000
3.812	0.074	4119.600	89.931	2.010
3.886	0.074	4072.990	90.721	2.020
3.961	0.074	4027.220	91.512	2.030
4.036	0.074	3982.270	92.302	2.040
4.110	0.074	3938.120	93.091	2.050
4.185	0.074	3894.760	93.879	2.060
4.259	0.074	3852.150	94.667	2.070
4.334	0.074	3810.290	95.455	2.080
4.408	0.074	3769.150	96.241	2.090
4.482	0.074	3728.730	97.027	2.100
4.556	0.074	3689.000	97.812	2.110
4.630	0.074	3649.950	98.595	2.120
4.704	0.074	3611.550	99.379	2.130
4.778	0.073	3573.810	100.161	2.140
4.852	0.073	3536.700	100.942	2.150
4.926	0.073	3500.210	101.722	2.160
4.999	0.073	3464.320	102.502	2.170

REFERENCES

1. Thomson, W. T.: "Vibration Theory and Applications", Prentice-Hall, Inc., Englewood Cliffs, New Jersey, 1965.

2. Anon.: "Buckling of Thin-Walled Circular Cylinders", NASA SP-8007, 1968.

3. Ashton, J. E., Halpin, J. C., Petit, P. H.: "Primer on Composite Materials", Technomic Publishing Co., Stamford, Connecticut, 1969.

SYMBOLS AND ABBREVIATIONS

D	Acceleration Density (g^2/Hz)
D.A.	Double Amplitude
E	Modulus of Elasticity
F_{cr}	Critical Stress
F_t	Maximum Tensile Stress
G	Shear Modulus
Hz	Hertz (Cycles/Second)
J	Moment of Inertia
M	Mass
N	Newton
Q	Vibration Transmissibility
$^\circ R$	Degree Rankine
RPM	Revolutions per Minute
T	Torque
cm	Centimeter
db	Decibel
f	Frequency (Hz)
g	Acceleration of Gravity
in.	Inch
k	Spring Constant
kg	Kilogram
lb	Pound
m	Meter
min.	Minute
oct	Octave
psi	lb/in^2
rad	Radian
sec	Second
δ_{xx}	Axial Flexibility Influence Coefficient
δ_{yy}	Lateral Flexibility Influence Coefficient

SYMBOLS AND ABBREVIATIONS (Continued)

$\delta_{\theta\theta}$	Rotational Flexibility Influence Coefficient
$\delta_{y\theta}=\delta_{\theta y}$	Coupling Flexibility Influence Coefficient
ν	Poissons' Ratio
τ	Shear Stress
τ_{cr}	Critical Shear Stress
ω	Angular Frequency
$\dot{\omega}$	Angular Velocity
$\ddot{\omega}$	Angular Acceleration